High-spin impurities and surface acoustic waves in piezoelectric crystals for spin-lattice coupling

Einar B. Magnusson

Jesus College

University of Oxford

A Thesis submitted for the Degree of

Doctor of Philosophy

Trinity Term, 2016

Acknowledgements

I have many people to thank for their contribution to this thesis: my supervisors, Peter Leek and Arzhang Ardavan, for this opportunity to work on an exciting and relevant topic in the field of quantum information, and for their support over the years; Danielle Kaminski for leading me through my first steps doing ESR; Will Myers for much help on all technical aspects of ESR experiments; Junjie Liu for many fruitful discussions about ideas for experiments and invaluable help in most experiments done in the 020 lab; Prabhak and Bob for preparing my crystal samples; Matthias Mergenthaler for providing the niobium-titanium-nitride CPW resonators; Riccardo Manenti for a lot of hours in the cleanroom fabricating SAW resonators on lithium niobate. Last but not least, I want to thank my amazing wife, Mel for being so patient with me.

I dedicate this thesis to my wonderful family, who have cheered me on for many years and I know they will for many years to come.

Contents

List of Figures

Chapter 1

Introduction

The burgeoning field of quantum information processing is set to revolutionise industry in the next decades with the realisation of long anticipated technologies such as quantum cryptography [2, 3] and quantum simulation and computation [4, 5]. Research in the field of quantum computing has received much public interest in recent years due to one of its potential applications of breaking classical encryptions based on large prime numbers, using Shor's algorithm [6]. Governments and industry are pushing forward in an arms race to have the first functional quantum computer, and thus the field is well funded and flourishing. Of course, there is much more to quantum technology than to do with encryption. Quantum computers and simulators have the potential to accelerate progress in general optimisation, pharmacology and artificial intelligence, to name a few [7]. Furthermore, quantum systems have great potential for application in sensing [8].

Many quantum systems have been studied very extensively and are even reaching maturity as building blocks for quantum computers, most notably superconducting qubits [9], which are the main contenders for the job of the processor in a quan-

tum computer. Solid state spin systems have properties that make them suitable as quantum memories for storing quantum information over longer periods than superconducting qubits can [10].

Hybrid quantum devices can be loosely defined as devices combining two or more building blocks of different physical nature [11, 12, 13]. This type of research is important as it has the potential to integrate vastly different systems with different properties into the same device. This can also open up entirely new ways of measuring various quantities, expanding our fundamental knowledge. Examples of hybrid device research includes coupling nanomechanical resonators to superconducting qubits [14] and coupling solid state spin ensembles to micron-scale microwave resonators [15].

1.1 Project overview

This project was conceived as a fusion between Arzhang Ardavan's results on electric field spin manipulation of Mn^{2+} spins in zinc oxide, and Peter Leek's expertise on surface acoustic waves (SAWs). The overall aim of the project has been to investigate coupling between SAWs and spin impurities in the substrate. This is an interesting direction within spin-lattice coupling in the context of quantum information technology since the planar structure of SAW devices is highly compatible with superconducting quantum circuits. A recent paper lists the virtues of SAWs for quantum information processing, calling the typical SAW transducer a "universal quantum transducer" for the ability of SAWs to enable long-range coupling of various types of qubits [16].

As we initially were focused on using the Mn^{2+}:ZnO system for our experiments, the first steps taken were to develop fabrication of SAW devices on ZnO substrates. This work proved to be worthy of publication [17] since bulk ZnO has not been a typical substrate for SAW devices previously.

To enable magnetic-field dependent experiments in our milli-Kelvin dilution fridge, we built a custom setup with the help of the cryomagnetics group in our department. Rather than using an expensive vector-magnet that requires three separate magnets to specify a field direction, we opted for one split-coil magnet and a rotating sample stage to be able to change the angle of the sample axis compared to the fixed magnetic field axis. We fabricated coplanar waveguide resonators using aluminium on both ZnO and sapphire to test their feasibility for spin coupling experiments. Shortly thereafter, we attempted to measure SAW-spin coupling using a SAW resonator fabricated on ZnO with unintentional Mn^{2+} impurities. At this time we have yet to observe the SAW-spin coupling in Mn^{2+}:ZnO.

Since the early attempts to observe SAW-spin coupling in Mn^{2+}:ZnO were unsuccessful, alternative spin systems with stronger coupling and/or higher spin concentration were sought. It turned out that some of our ZnO samples had a high amount of Fe^{3+} impurities. These were investigated and found to have even larger electric field effect than Mn^{2+}. Furthermore, temperature dependence of both static Hamiltonian parameters and the electric field effect was compared, supporting the conclusion that the electric field effect is in this case proportional to the zero-field splitting.

Another spin system identified as high potential for SAW-spin coupling experiments was iron-doped lithium niobate (LN). Very large zero-field splitting and readily avail-

able highly doped substrates led us to try this system. We treated a part of the samples to reduce Fe^{3+} ions to Fe^{2+}, and compared spectra. In an attempt to yield samples with even higher iron density and higher quality crystal structure, a wafer of stoichiometric undoped lithium niobate was diffusion doped by evaporating a layer of iron and annealing at high temperature.

After investigating the Fe:LN system with traditional ESR, we fabricated SAW resonators on both Fe^{3+}:LN and Fe^{2+}:LN. The latter were more promising due to the spin system's enormous crystal field splitting, and indeed this is where we observed a spin resonance signal. We measured the $\Delta m_s = 2$ transition as a function of field angle, temperature and power.

1.2 Thesis outline

In Chapter 2, we discuss the relevant background and theory for this project, including electron spin resonance, spin-lattice interaction and surface acoustic wave devices. Relevant results in the field are described.

In Chapter 3, the experimental equipment and methods are explained, including a non-standard setup intended for rotating a microwave device in a fixed axis magnetic field inside a dilution fridge. An experiment showing the field and angle dependent performance of a coplanar waveguide resonator is reported as a test for the new setup.

In Chapter 4, we present ESR experiment results on Fe^{3+} spins in ZnO as well as Fe^{2+} in lithium niobate. This includes electric field effect results for Fe^{3+}:ZnO.

In Chapter 5, results from various SAW device experiments are presented, including a SAW delay line and resonator on ZnO and resonators on lithium niobate.

In Chapter 6, we present our surface acoustic wave spin resonance (SAWSR) experiment results coupling a one-port SAW resonator to Fe^{2+} spins in lithium niobate.

We conclude with a summary of what has been accomplished and an outlook including proposed future experiments involving SAWs and electron spins.

Chapter 2

Theory and background

This project is concerned with the coupling of spin ensembles to surface acoustic waves. We will here review some background theory that is important to this topic, namely the physics of electron spin resonance, spin-lattice coupling and surface acoustic waves. We will also review the background field of quantum information, with particular focus on the powerful concept of cavity QED. We will give motivation for the need for hybrid device research to bridge the gap between different physical systems to harness their different qualities.

2.1 Quantum Information and Cavity-QED

Some of the basic building blocks of quantum information processing (QIP) are: quantum two-level systems (qubits) with long coherence time, read-out methods for determining the state of the qubit, and one- or multi-qubit logic gate operations. Since read-out and gating involve the interaction of different systems, the study of these interactions is of great importance to the field. A very general but crucial interaction is the one between a bosonic field and a two-level system (TLS), such

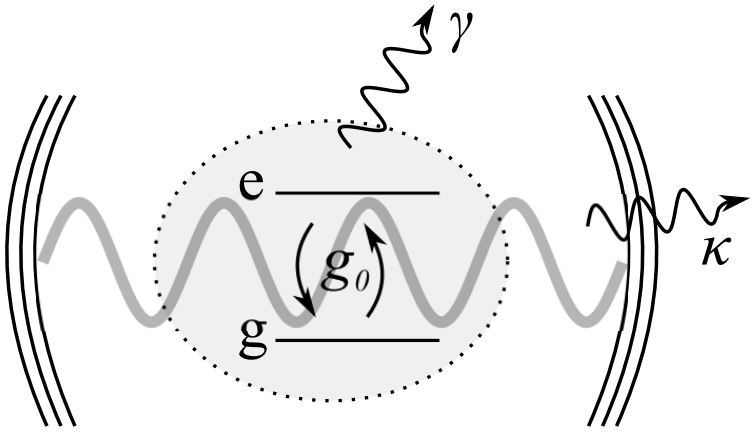

Figure 2.1: Schematic of a quantum two-level system interacting with a bosonic cavity mode.

as between light and an atom, and is described in detail in various quantum optics texts [18, 19, 20]. As such interactions can be quite small, the approach is to confine the bosonic field in a cavity to enhance the field strength of a single boson to useful levels and increase the interaction time of the boson with the TLS. The study of this system is called cavity quantum electrodynamics (cavity-QED). When the resonant frequency of the cavity is close to the transition frequency of the TLS, the rotating wave approximation (RWA) is usually applied and the approximated Hamiltonian of such a system describes the Jaynes-Cummings model:

$$H_{\mathrm{JC}} = \hbar\omega_c \left(\hat{a}^\dagger \hat{a} + \frac{1}{2}\right) + \frac{\hbar\omega_{\mathrm{TLS}}}{2}\hat{\sigma}_z + \hbar g_0 \left(\hat{a}^\dagger \hat{\sigma}_- + \hat{a}\hat{\sigma}_+\right). \tag{2.1}$$

Here, ω_c is the resonant frequency of the cavity, $\hbar\omega_{\mathrm{TLS}}$ is the energy splitting of the two-level system, $\hbar g_0$ is the interaction strength, $\hat{a}$ is the annihilation operator relating to the bosonic field and $\hat{\sigma}_\pm$ are pseudospin-1/2 operators for the TLS. The Jaynes-Cummings model is not valid if multiple bosonic modes, qubits with more than two levels, or very large cavity-qubit detunings need to be considered.

Defining $|m, s\rangle$ as the system state with m bosons and the TLS in state $s \in \{g, e\}$ (g

being the ground state and e the excited state), the eigenstates of the J-C models are superpositions of $|n, e\rangle$ and $|n+1, g\rangle$ with energies (at zero detuning between cavity and TLS, $\omega_{\mathrm{TLS}} = \omega_c$)

$$E_n^{\pm} = (n + 1/2)\hbar\omega_c \pm \sqrt{n+1}\hbar g_0 \tag{2.2}$$

where n is the number of photons (bosons) in the system. An energy splitting $\Delta E = 2\hbar\sqrt{n+1}g_0$ is observed. In fact, there is a splitting even when $n = 0$, since there is a vacuum field with energy $E_0 = \frac{1}{2}\hbar\omega_c$. This is called the vacuum Rabi splitting, with frequency $\Delta\Omega^{\mathrm{vac}} = 2g_0$. For an ensemble of N atoms, the collective excitation has a $\sqrt{N}$ enhancement to the coupling strength and thus a vacuum Rabi frequency of $\Delta\Omega^{\mathrm{vac}} = 2\sqrt{N}g_0$.

In any real system, both the cavity mode and the two-level system experience losses at rates κ and γ, respectively. The system is schematically depicted in Figure 2.1. The quality factor of the cavity is related to the loss rate

$$Q = \frac{\omega_c}{\Delta\omega_c} = \omega_c\tau = \frac{\omega_c}{\kappa} \tag{2.3}$$

where κ is equated to $\Delta\omega_c$, the width of the resonance, and τ is the mode lifetime. The loss rate κ can be a sum of multiple different contributions, depending on the type of resonator. There are at least three different regimes depending on the relative strength of parameters: weak coupling ($g_0 \ll \kappa, \gamma$), strong coupling ($\kappa, \gamma \ll g_0 \ll \omega_{\mathrm{TLS}}$) and ultra-strong/deep strong coupling ($g_0 \sim \omega_{\mathrm{TLS}}$). The Jaynes-Cummings Hamiltonian is valid for weak and strong coupling, but the RWA breaks down in the ultra-strong coupling regime. Being in the strong coupling regime rather than the weak, in essence means that there is time to transfer the energy between the two level system and the

cavity mode before the state dissipates. It also has the mathematical meaning that the eigenstates are qualitatively the same as that of the non-dissipative J-C model, while the eigenstates in the weak coupling regime have no energy splitting at zero detuning.

A multitude of systems have been proposed and realised for qubits, such as trapped ions [21, 22], various types of solid state spin systems [15, 23] and superconducting qubits [24, 25]. Their various properties such as size, energy gap, coherence time and gate operation time, vary widely between the systems [12].

2.1.1 Hybrid systems

As different quantum systems have their advantages and disadvantages, there has been a lot of research focused on creating hybrid quantum systems [12, 11, 13]. The main effort has been focused on interfacing atomic, molecular and optical (AMO) and solid state spin qubits with superconducting (SC) qubits, since the SC circuit architecture is easily scalable and controllable. The AMO/spin qubits typically have much longer coherence times than the SC qubits, and could thus act as quantum memories in a SC circuit. Two main categories of proposals exist: directly coupling a SC qubit to an AMO/spin qubit, and indirectly coupling them through a quantum cavity resonator (usually a coplanar waveguide resonator).

A direct-coupling scheme was realised in 2011 [26] where an ensemble of nitrogen-vacancy centres in diamond was placed in close vicinity to a superconducting flux qubit with highly tuneable energy splitting. Strong coupling was observed with a

vacuum Rabi splitting of 70 MHz. The relaxation rates of the qubit and spin ensemble were about $\gamma \simeq 7\,\mathrm{MHz}$ and $\kappa \ll 0.1\,\mathrm{MHz}$, respectively.

Indirect coupling has also been achieved, by strongly coupling NV centres to a coplanar waveguide resonator [15]. The coupling strength between the ensemble of $N \sim 10^{12}$ spins and the resonator was $g \simeq 11\,\mathrm{MHz}$, the relaxation rate of the resonator $\kappa \simeq 0.1\,\mathrm{MHz}$ and the linewidth of the spins $\gamma \simeq 6\,\mathrm{MHz}$. In direct succession of this progress, a SC qubit was coupled to the ensemble of NV centres using a SC resonator as a quantum bus [27]. Superposition states were prepared in the qubit, transferred over to a collective excitation of the spin ensemble and shortly thereafter retrieved back to the qubit, offering a proof of principle for a quantum memory.

There have also been successes in coupling micro- and nano-mechanical resonators to quantum systems, aided by advances in cooling techniques [12, 28], bringing mechanical systems to the quantum regime. Most mechanical resonators (cantilevers, nano drums, etc.) have fairly low resonant frequencies and thus need to be actively cooled to extremely low temperatures to avoid thermal excitation. Very recently, some highly relevant research has been done on coupling NV centres in diamond to mechanical bulk resonances [29] and even surface acoustic waves [30].

2.2 Spin physics

Many fundamental particles, such as electrons, protons and neutrons carry a magnetic moment due to the fundamental property called spin. The magnetic moment is a

vector that is parallel to the spin vector:

$$\boldsymbol{\mu} = \gamma \boldsymbol{S} \tag{2.4}$$

where the gyromagnetic ratio γ depends on the particle. For free electrons, $\gamma = -\frac{g\mu_B}{\hbar}$, where $g \simeq 2$ is the g-factor, which signifies that electrons have about twice as high a magnetic moment compared to the classical model of a spinning charged particle. The Bohr magneton $\mu_B = \frac{e}{2m_e}$ comes from the classical consideration.

2.2.1 Magnetic moment in a magnetic field

There are two main effects of placing a magnetic moment $\boldsymbol{\mu}$ in an applied magnetic field $\boldsymbol{B}_0$. Firstly, a torque on the magnetic moment

$$\boldsymbol{\tau} = \boldsymbol{\mu} \times \boldsymbol{B_0} \tag{2.5}$$

which causes it to precess around $\boldsymbol{B}_0$ if it is not parallel to it. Secondly, the orientation of $\boldsymbol{\mu}$ gets a potential energy associated with it, expressed by

$$E = -\boldsymbol{\mu} \cdot \boldsymbol{B}_0 \tag{2.6}$$

or, taking the magnetic field axis to be the z axis,

$$E = -\mu_z B = \frac{g\mu_B}{\hbar} S_z B_0. \tag{2.7}$$

The effect of the torque $\boldsymbol{\tau}$ is to make the moment precess around the magnetic field (see Figure 2.2(a)), and it does so with the Larmor angular frequency

$$\omega_L = -\gamma B_0. \tag{2.8}$$

If we go to a rotating frame of reference rotating with the Larmor frequency, the moment appears stationary. If now we apply an additional smaller magnetic field B_1 in the plane perpendicular to B_0 (see Figure 2.2(b)) that rotates with the Larmor frequency, it appears static in the rotating frame. The moment will then precess around $\boldsymbol{B}_1$ with a frequency $\omega_1 = \gamma B_1$. This explains how applying a correctly polarised electromagnetic field oscillating with the Larmor frequency will make the magnetic moment oscillate between states of different energy.

2.2.2 Bloch equations

Let us give a mathematical explanation for the statements about Larmor precession and the rotating frame. Felix Bloch introduced phenomenological equations describing the dynamics of macroscopic magnetisation $\boldsymbol{M}$ including characteristic relaxation times, where $\boldsymbol{M}$ can be considered an average polarisation of an ensemble of microscopic spins. Starting with no relaxation, the equation in vector form is the simple fundamental one from which Larmor precession is derived:

$$\frac{d\boldsymbol{M}(t)}{dt} = \gamma \boldsymbol{M}(t) \times \boldsymbol{B}(t) \tag{2.9}$$

or separated into components:

$$\frac{dM_x(t)}{dt} = \gamma(\boldsymbol{M}(t) \times \boldsymbol{B}(t))_x = \gamma(M_y(t)B_z(t) - M_z(t)B_y(t)) \tag{2.10}$$

$$\frac{dM_y(t)}{dt} = \gamma(\boldsymbol{M}(t) \times \boldsymbol{B}(t))_y = \gamma(M_z(t)B_x(t) - M_x(t)B_z(t)) \tag{2.11}$$

$$\frac{dM_z(t)}{dt} = \gamma(\boldsymbol{M}(t) \times \boldsymbol{B}(t))_z = \gamma(M_x(t)B_y(t) - M_y(t)B_x(t)). \tag{2.12}$$

Let z be the axis along which the polarising static magnetic field B_0 is applied. If we write $M_{xy} = M_x + iM_y$ and $B_{xy} = B_x + iB_y$, we can write one equation for the

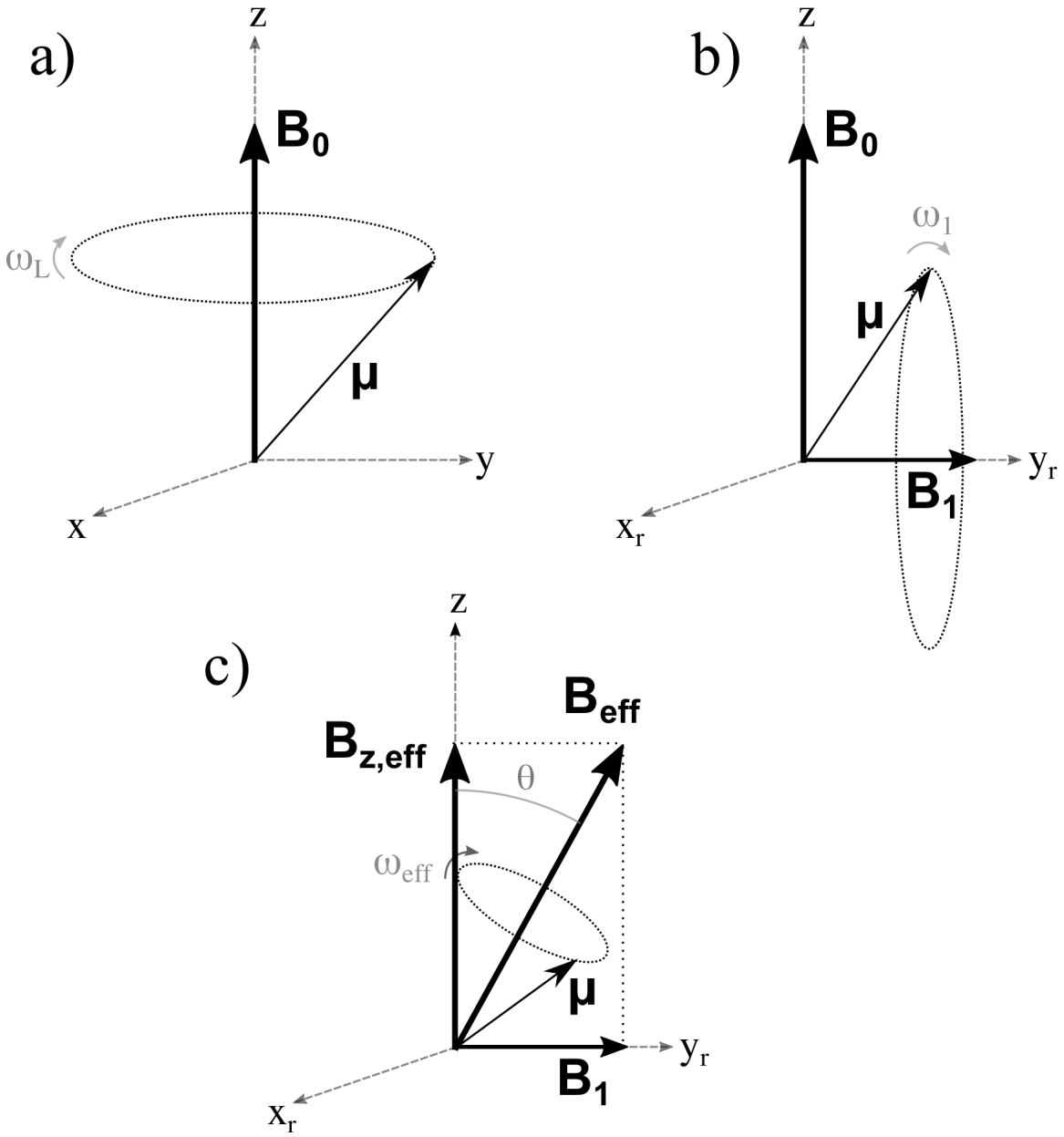

Figure 2.2: (a) A magnetic moment $\boldsymbol{\mu}$ placed in a static magnetic field $\boldsymbol{B}_0$ experiences a torque that makes it precess around $\boldsymbol{B}_0$ at the Larmor frequency $\omega_L = -\gamma B_0$. (b) In a frame of reference rotating at the Larmor frequency, $\boldsymbol{\mu}$ will appear stationary. Applying a time-dependent magnetic field $\boldsymbol{B}_1$ rotating around $\boldsymbol{B}_0$ also at the Larmor frequency, $\boldsymbol{\mu}$ will appear to rotate around $\boldsymbol{B}_1$ with the frequency $\omega_1 = \gamma B_1$.
(c) If the applied transverse B_1 oscillates at a frequency $\omega \neq \omega_L$, there is a non-zero effective z component to the magnetic field, and $\boldsymbol{\mu}$ precesses around an effective $\boldsymbol{B}_{\text{eff}}$ with a frequency $\omega_{\text{eff}} \geq \omega_1$.

parallel magnetisation and one for the transverse magnetisation:

$$\frac{dM_{xy}(t)}{dt} = -i\gamma(M_{xy}(t)B_z(t) - M_z(t)B_{xy}(t)) \tag{2.13}$$

$$\frac{dM_z(t)}{dt} = i\gamma/2(M_{xy}(t)\overline{B_{xy}(t)} - \overline{M_{xy}(t)}B_{xy}(t)). \tag{2.14}$$

With $B_z = B_0$ and $B_x = B_y = 0$, the equations are

$$\frac{dM_{xy}(t)}{dt} = -i\gamma M_{xy}(t)B_0 \tag{2.15}$$

$$\frac{dM_z(t)}{dt} = 0 \tag{2.16}$$

which has the solution $M_{xy} = M^0_{xy}e^{-i\gamma B_0 t}$, $M_z = M_0$, where $M_0 = M_z(t = 0)$ and $M^0_{xy} = M_{xy}(t = 0)$. This shows that $\boldsymbol{M}$ precesses around the z axis with the angular Larmor frequency $\omega_L = -\gamma B_0$.

We can add phenomenological terms to account for relaxation of magnetisation:

$$\frac{dM_{xy}(t)}{dt} = -i\gamma(M_{xy}(t)B_z(t) - M_z(t)B_{xy}(t)) - \frac{M_{xy}(t)}{T_2} \tag{2.17}$$

$$\frac{dM_z(t)}{dt} = i\gamma/2(M_{xy}(t)\overline{B_{xy}(t)} - \overline{M_{xy}(t)}B_{xy}(t)) - \frac{M_z(t) - M_0}{T_1} \tag{2.18}$$

where we are assuming that the polarising magnetic field B_0 induces a steady state finite magnetisation M_0.

2.2.2.1 Rotating frame

Switching to a rotating frame of reference amounts to writing $\tilde{M}_{xy} = M_{xy}e^{-i\omega t}$ and $\tilde{B}_{xy} = B_{xy}e^{-i\omega t}$, yielding equations of motion in the rotating frame:

$$\frac{d\tilde{M}_{xy}(t)}{dt} = -i(\gamma B_z(t) - \omega)M_{xy}(t) + i\gamma\tilde{B}_{xy}(t)M_z(t) - \frac{\tilde{M}_{xy}(t)}{T_2} \tag{2.19}$$

$$\frac{dM_z(t)}{dt} = i\gamma/2(\tilde{M}_{xy}(t)\overline{\tilde{B}_{xy}(t)} - \overline{\tilde{M}_{xy}(t)}\tilde{B}_{xy}(t)) - \frac{M_z(t) - M_0}{T_1}. \tag{2.20}$$

In the case of $B_{xy} = 0$, $B_z = B_0$ and without relaxation, M_z is stationary and $\tilde{B}_{xy}$ precesses at an effective angular frequency of $\omega_{\text{eff}} = \gamma B_0 - \omega$, giving rise to the definition of an effective magnetic field $B_{\text{z,eff}} = B_0 - \omega/\gamma$. In the resonant case of $\omega = \gamma B_0$, $B_{\text{z,eff}} = 0$ and the magnetic moment is stationary.

If we now apply a circularly polarised transverse magnetic field B_1 with frequency ω, and move into the rotating frame (also rotating with frequency ω), the effective magnetic field $\boldsymbol{B}_{\text{eff}}$ is the vector sum of $B_{\text{z,eff}}$ and B_1, which we can take to be along for example the y_r axis without loss of generality. The magnetic moment will then precess around $\boldsymbol{B}_{\text{eff}}$, as shown in Figure 2.2(c), with a frequency of $\omega_{\text{eff}} = \sqrt{(\omega_L - \omega) + (\gamma B_1)^2}$. The angle that $\boldsymbol{B}_{\text{eff}}$ makes with the z axis is $\theta = \tan^{-1}\left(\frac{B_1}{B_0 - \omega/\gamma}\right)$, with the limiting case of $\omega = \omega_L$ where the effective magnetic field equals $\boldsymbol{B}_1$ and makes a 90° angle with the z axis. The steady state solution is easily found in the resonant case, and we find that

$$M_z^{\infty} = \frac{M_0}{1 + \gamma^2 B_1^2 T_1 T_2}. \tag{2.21}$$

2.2.3 Quantum mechanical treatment

The Bloch equations are useful for describing the dynamics of a classical magnetic moment or an ensemble of simple quantum spins like single free electrons, but for a valid description of the dynamics of a general spin system we need a quantum mechanical treatment. Due to the quantum physics of angular momentum, particle spin is quantised, characterised by the total spin quantum number $S = n/2$ where n is any non-negative integer. The spin projected on any axis i can only take the values $S_i = \hbar m_s^{(i)}$, where $m_s^{(i)} \in \{-S, -(S-1), ..., (S-1), S\}$. There are thus $2S + 1$

possible states for the projected spin. The electron has a spin quantum number of $S = 1/2$, and can thus have projected spin $S_z = \pm\hbar/2$. As the spin S_z is quantised, the energy has discrete allowed values

$$E = g\mu_B B_0 m_s \tag{2.22}$$

or in the case of the electron,

$$E = \pm g\mu_B B_0/2. \tag{2.23}$$

In traditional ESR studies, we work with a large ensemble of spins which each can occupy different energy states. At a finite temperature T, the equilibrium distribution of spins between the different energy levels follows a Boltzmann law, so the number of spins that are in the state with energy E_i is

$$n(E_i) \propto \exp\left(-\frac{E_i}{k_B T}\right) \tag{2.24}$$

where k_B is the Boltzmann constant. Thus, in equilibrium there is always a higher population in the lower of any two energy levels.

The general approach to understand a given spin system is to construct a microscopic Hamiltonian from knowledge of the environment, and then treat the applied excitation with perturbation theory. In the simple example we have so far treated classically, where a free spin J is placed in a static field B_0 taken to be along the z axis, the Hamiltonian is

$$H = -\boldsymbol{\mu} \cdot \boldsymbol{B} = -\hbar\gamma B_0 J_z \tag{2.25}$$

and the eigenstates are defined by the quantum number of J_z, m, with eigenenergies

$$E_m = \langle m|H|m\rangle = -\hbar\gamma B_0 \langle m|J_z|m\rangle = -\hbar\gamma B_0 m. \tag{2.26}$$

The oscillating transverse field $\boldsymbol{B}_1$ is then treated as a perturbation to the Hamiltonian:

$$H_1 = -(B_x\mu_x + B_y\mu_y) = -\frac{\hbar\gamma B_1}{2}\left(J_+e^{-i\omega t} + J_-e^{i\omega t}\right) \tag{2.27}$$

where $J_\pm = J_x \pm iJ_y$. Using time-dependent perturbation theory we find that the rate of transition between states $|n\rangle$ and $|m\rangle$ is

$$w_{nm} = \frac{\pi}{2}|\langle n|\, H_1\, |m\rangle\,|^2 f(\omega) \tag{2.28}$$

where $f(\omega)$ is a shape function accounting for a distribution of Larmor frequencies. The total energy absorption is

$$\frac{\mathrm{d}E}{\mathrm{d}t} = \hbar\omega\left(n(E_m) - n(E_n)\right)w_{nm}. \tag{2.29}$$

In the simple case above, the only nonzero matrix elements $\langle n|\, H_1\, |m\rangle$ of the perturbation are those where $n = m \pm 1$, giving us the selection rule for the transition:

$$\Delta m = \pm 1. \tag{2.30}$$

A more in-depth quantum mechanical treatment can be found in [31, 32].

2.2.4 Microscopic Hamiltonian

As discussed above, to describe any spin system beyond the free electron efficiently, we need to define the microscopic Hamiltonian. For most spin systems beyond the free electron, we find an effective spin Hamiltonian describing only the energy levels accessible at the energy scale used in ESR. The Zeeman term has already been discussed, and it describes the shifting of energy levels due to an externally applied

magnetic field. To account for anisotropy in molecules and crystal structures, the g factor is written in tensor form:

$$H_0 = \frac{\mu_B}{\hbar} \boldsymbol{B} \cdot \boldsymbol{g} \cdot \boldsymbol{S}. \tag{2.31}$$

It is this term that is tuned when the magnetic field is swept in ESR experiments. For convenience, we often write $\beta = \frac{\mu_B}{\hbar}$.

2.2.4.1 Hyperfine splitting

When the spin system has both electron spin $\boldsymbol{S}$ and nuclear spin $\boldsymbol{I}$, the magnetic dipole interaction between the two, as well as Fermi contact interaction and electric quadrupole interaction [31], can give rise to a Hamiltonian term called the hyperfine splitting term:

$$H_{\text{hf}} = \boldsymbol{S} \cdot \boldsymbol{A} \cdot \boldsymbol{I} \tag{2.32}$$

where the hyperfine splitting tensor $\boldsymbol{A}$ quantifies the magnitude of the possibly anisotropic interaction. For example, Mn^{2+} has $S = 5/2$ and $I = 5/2$, giving rise to a 6-fold splitting of each $\Delta m_S = \pm 1$ resonance, as m_I can take any of the values $\pm 1/2$, $\pm 3/2$ and $\pm 5/2$.

2.2.4.2 Crystal field effect

The crystal field effect [33] is the most important Hamiltonian part for us to consider, as this is what is responsible for the coupling of lattice vibrations to spins. An ion in a crystal experiences a crystal field potential due to its own electrons interacting with the neighbouring ions:

$$V_c = \sum_i q_i V_i = \sum_{i,j} \frac{q_i q_j}{4\pi\varepsilon_0 |\boldsymbol{R}_j - \boldsymbol{r}_i|} \tag{2.33}$$

where i sums over the electrons of the unfilled shell, and j sums over neighbouring ions. The potential can be expanded in spherical harmonics Y_n^m with the position of the nucleus as origin:

$$V_c = \sum_{n,m} A_n^m r^n Y_n^m(\theta, \phi). \tag{2.34}$$

The number of non-zero terms is greatly reduced by two considerations. Firstly, when evaluating the effect of V_c on energy levels of the ion, its matrix element with respect to the relevant electron's wave function must be calculated:

$$V_{ij} = \langle \psi_i | \, V_c \, | \psi_j \rangle \, . \tag{2.35}$$

As the orbital part of the electron wave function is described by spherical harmonics, the matrix elements consist of an integral over the product of three spherical harmonics. A mathematical rule states that the integral of three spherical harmonics is nonzero only if the n of the three functions can form a triangle, i.e. none of the numbers can be larger than the sum of the others or smaller than their difference. When dealing with 3d electrons (e.g. Mn^{2+} and Fe^{3+}), which are described by spherical harmonics of order 2, the expansion of V_c can only contain terms with $n \leq 4$. Secondly, symmetry considerations will further reduce the number of terms. For example, in a tetrahedral symmetry with axial anisotropy, there is a trigonal symmetry around the anisotropy axis. For 3d ions, m can then be limited to $0, \pm 3$.

2.2.4.3 Stevens equivalent operators

In the effort of evaluating the matrix elements of V_c, a transformation from spherical harmonics to so-called Stevens equivalent operators $O_n^m(\hat{L}_i)$ [34] is beneficial. As a

result of this, the crystal field Hamiltonian terms are generally represented as

$$H_{\mathrm{CF}} = \sum_{n,m} B_n^m O_n^m \tag{2.36}$$

where the same symmetry arguments hold for O_n^m as for the spherical harmonics. The following equations show us a few useful Stevens operators:

$$O_2^0 = 3L_z^2 - X \tag{2.37}$$

$$O_2^2 = \frac{1}{2}(L_+^2 + L_-^2) = L_x^2 - L_y^2 \tag{2.38}$$

$$O_3^0 = 5L_z^3 - (3X - 1)L_z \tag{2.39}$$

$$O_3^3 = \frac{1}{2}(L_+^3 + L_-^3) \tag{2.40}$$

$$O_4^0 = 35L_z^4 - (30X - 25)L_z^2 + 3X^2 - 6X \tag{2.41}$$

$$O_4^3 = \frac{1}{4}((L_+^3 + L_-^3)L_z + L_z(L_+^3 + L_-^3)) \tag{2.42}$$

$$X = L(L + 1) \tag{2.43}$$

where L_+ and L_- are angular momentum operators. Convention as well as convenience has resulted in other crystal field terms being used, depending on the ion. For example, the second order zero-field splitting Hamiltonian is conventionally written as

$$H_{\mathrm{ZFS}} = DS_z^2 + E(S_x^2 - S_y^2), \tag{2.44}$$

which by comparison to the Stevens operator Hamiltonian means that $D = 3B_2^0$ and $E = B_2^2$ [35]. Here, the effective Hamiltonian spin S notation is used, which can sometimes be different from the total electron spin.

An important consideration in determining the effective spin Hamiltonian of an ion in a crystal is the relative magnitude of spin-orbit interaction compared to the crystal field interaction. For most transition metals, the crystal field energy scale is an order of magnitude larger than that of spin-orbit interaction, meaning that total spin S and total orbital angular momentum L are good quantum numbers. In this case, the spin-orbit interaction is treated as a perturbation after treating the crystal field effect. An example derivation is shown in reference [33].

2.2.4.4 Hamiltonian of Mn^{2+} and Fe^{3+} in trigonal axis field

Following Abragam and Bleaney [31], the Hamiltonian including crystal field effect and Zeeman effect can be written

$$H = \beta \boldsymbol{B} \cdot \boldsymbol{g} \cdot \boldsymbol{S} - \frac{2}{3} B_4 (O_4^0 + 20\sqrt{2} O_4^3) + B_2^0 O_2^0 + B_4^0 O_4^0 \tag{2.45}$$

but is usually written in the form

$$\begin{aligned} H =& \beta \boldsymbol{B} \cdot \boldsymbol{g} \cdot \boldsymbol{S} + D \left(S_z^2 - \frac{1}{3} S(S+1) \right) && (2.46) \\ &+ \frac{1}{6} a \left(S_\xi^4 + S_\eta^4 + S_\zeta^4 - \frac{1}{3} S(S+1)(3S^2+3S-1) \right) && (2.47) \\ &+ \frac{1}{180} F \left(35 S_z^4 - 30 S(S+1) S_z^2 + 25 S_z^2 - 6S(S+1) + 3 S_z^2 (S+1)^2 \right) && (2.48) \end{aligned}$$

where $\xi\eta\zeta$ is the perpendicular axes system of the crystal field, the z axis is along the trigonal axis ([111] direction in the $\xi\eta\zeta$ system), and the relation between the

parameters is

$$D = 3B_2^0 \tag{2.49}$$

$$a = 120B_4 \tag{2.50}$$

$$F = 180B_4^0. \tag{2.51}$$

The strongly allowed transitions have been evaluated assuming Zeeman interaction to be dominant:

$$|\pm\frac{5}{2}\rangle \leftrightarrow |\pm\frac{3}{2}\rangle : g\beta B = g\beta B_0 \mp \left(2D(3\cos^2\theta - 1) + 2pa + \frac{1}{6}Fq\right) - 32\delta_1 + 4\delta_2 + \epsilon_1 \tag{2.52}$$

$$|\pm\frac{3}{2}\rangle \leftrightarrow |\pm\frac{1}{2}\rangle : g\beta B = g\beta B_0 \mp \left(D(3\cos^2\theta - 1) - \frac{5}{2}pa - \frac{5}{24}Fq\right) + 4\delta_1 - 5\delta_2 + \epsilon_2 \tag{2.53}$$

$$|+\frac{1}{2}\rangle \leftrightarrow |-\frac{1}{2}\rangle : g\beta B = g\beta B_0 + 16\delta_1 - 8\delta_2 + \epsilon_3 \tag{2.54}$$

where

$$B_0 = \frac{hf}{g\beta} \tag{2.55}$$

$$p = (1 - 5\phi) \tag{2.56}$$

$$\phi = (l^2m^2 + m^2n^2 + n^2l^2) \tag{2.57}$$

$$\epsilon_1 = \frac{a^2}{g\beta B_0}\left(\frac{5}{3}\phi(1 - 7\phi)\right) \tag{2.58}$$

$$\epsilon_2 = -\frac{a^2}{g\beta B_0}\left(\frac{5}{48}(3 + 178\phi - 625\phi^2)\right) \tag{2.59}$$

$$\epsilon_3 = \frac{a^2}{g\beta B_0}\left(\frac{10}{3}\phi(7 - 25\phi)\right) \tag{2.60}$$

$$q = 35\cos^4\theta - 30\cos^2\theta + 3 \tag{2.61}$$

$$\delta_1 = \frac{D^2}{g\beta B_0}\cos^2\theta\sin^2\theta \tag{2.62}$$

$$\delta_2 = \frac{D^2}{4g\beta B_0}\sin^4\theta \tag{2.63}$$

where l, m, n are the cosines of the angle of $\boldsymbol{B}$ to the crystal field axes.

In the case when the magnetic field is parallel to the anisotropy axis of the crystal ($\theta = 0$), the cosines are all equal to $l = m = n = 1/\sqrt{3}$, and $\phi = 1/3$, $p = -2/3$. Thus, the equations (2.54) simplify to

$$|\pm\frac{5}{2}\rangle \leftrightarrow |\pm\frac{3}{2}\rangle : g\beta B = g\beta B_0 \mp \left(4D - \frac{4}{3}(a - F)\right) + \epsilon_1 \tag{2.64}$$

$$|\pm\frac{3}{2}\rangle \leftrightarrow |\pm\frac{1}{2}\rangle : g\beta B = g\beta B_0 \mp \left(2D + \frac{5}{3}(a - F)\right) + \epsilon_2 \tag{2.65}$$

$$|+\frac{1}{2}\rangle \leftrightarrow |-\frac{1}{2}\rangle : g\beta B = g\beta B_0 + \epsilon_3. \tag{2.66}$$

As a is usually a fairly small parameter, the terms $\epsilon_1, \epsilon_2, \epsilon_3 \propto a^2/(g\beta B_0)$ can often be dropped when extracting the value of D and $a - F$ from the parallel spectrum.

As there are two non-equivalent sites in the lattice, that have different orientation of the neighbouring lattice ions, the terms depending on ϕ can cause a splitting in the spectrum when the field is oriented away from the anisotropy axis. This splitting can be used to get the value of a.

2.2.5 Absorption measurements

The first thing one usually wants to do when confronted with an unknown spin system is to learn something about its Hamiltonian. As we have shown above, the spin system has a specific eigenlevel energy structure for a given magnetic field, orientation, etc.. There can be one or more allowed level transitions at different frequencies depending on the complexity of the system. At a fixed magnetic field B_0, one could then irradiate the spins with a microwave range signal at frequency f, sweep f and observe absorption of the signal when it's on resonance with an energy level difference

in the spin system. Due to experimental reasons, measurements are most commonly done at a fixed frequency f and sweeping the magnetic field B_0, as represented in Figure 2.3. The absorption spectrum A then gives information about the relative position of the energy levels. To increase sensitivity in the measurement, the magnetic field is modulated by a small amplitude ΔB_0 at a typical frequency of $1 - 100\,\mathrm{kHz}$, and the signal at this frequency is picked out using a lock-in amplifier. This results in the actual plot observed being the derivative of absorption. We refer to this type of measurement as a continuous wave (CW) experiment, and it is described in experimental detail in section 3.1.1.

The strength of the absorption signal depends on the rate of energy absorbed, which can be shown to be

$$\frac{\mathrm{d}W}{\mathrm{d}t} = \frac{M_0 B}{T_1}\frac{M_z - M_0}{M_0} = \frac{M_0 B}{T_1}\frac{\gamma^2 B_1^2 T_1 T_2}{1 + \gamma^2 B_1^2 T_1 T_2} \tag{2.67}$$

which shows that the absorption increases with microwave power up to a saturating value. The linewidth also gets broadened by the factor $1 + \gamma^2 B_1^2 T_1 T_2$, and if it is limited by the relaxation rate, it is [36]

$$(\Delta B_{pp})^2 = \frac{4}{3\gamma T_2^2}(1 + \gamma^2 B_1^2 T_1 T_2) \tag{2.68}$$

where ΔB_{pp} is the peak-to-peak linewidth of the resonance.

2.2.6 Spin dynamics

To probe the dynamics of a spin system, we need to make time-resolved measurements. This means sending time-dependent pulses of microwave radiation to manipulate the spins and then observing how they evolve over time.

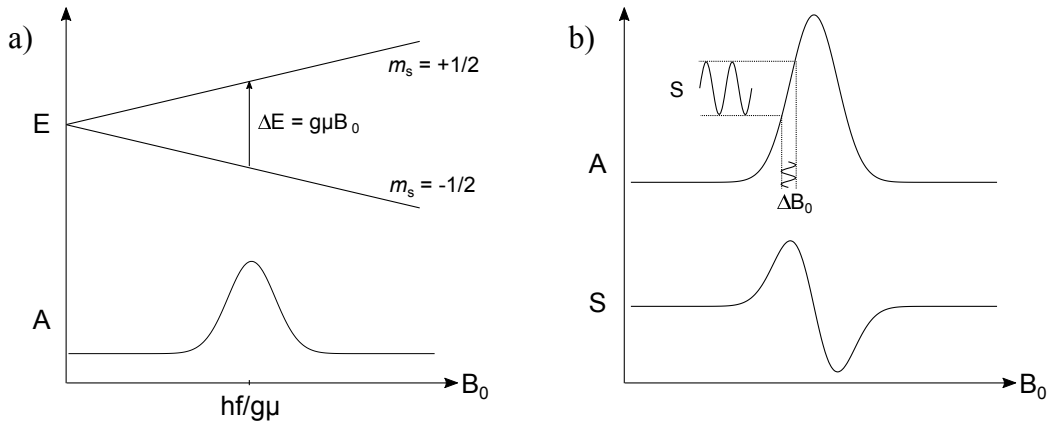

Figure 2.3: a) The energy levels of a free electron placed in a magnetic field, and a sketch of the absorption as a function of applied magnetic field B_0 when irradiated with a frequency f. b) For increased sensitivity, the absorption A is measured with a modulation of the magnetic field, resulting in a derivative signal $S = \frac{\mathrm{d}A}{\mathrm{d}B}$ being recorded.

For talking about the dynamics of ESR transitions, it is useful to introduce the concept of the Bloch sphere. The idea is essentially that whenever you are resonantly addressing two levels $|g\rangle$ and $|e\rangle$, and all other transition frequencies are far off from the one under consideration, we can map the levels onto a $S = 1/2$ pseudo spin. The lower level ground state $|g\rangle$ maps to the north pole of the sphere, $|e\rangle$ to the south pole, and any coherent superposition of the two are on the surface of the sphere. Any coherent superposition

$$|\psi\rangle = \cos(\theta/2)\,|g\rangle + \sin(\theta/2)e^{i\phi}\,|e\rangle \tag{2.69}$$

can thus be represented on the surface of the Bloch sphere with the angles θ and ϕ defined in Figure 2.4. Any decoherence is represented by a reduction of the transverse component and thus a reduction of the length of the vector.

As discussed previously, applying a resonantly rotating magnetic field B_1 to a spin will make the spin precess around B_1, with an angular frequency of $\omega_1 = \gamma B_1 = g\mu_B B_1/\hbar$.

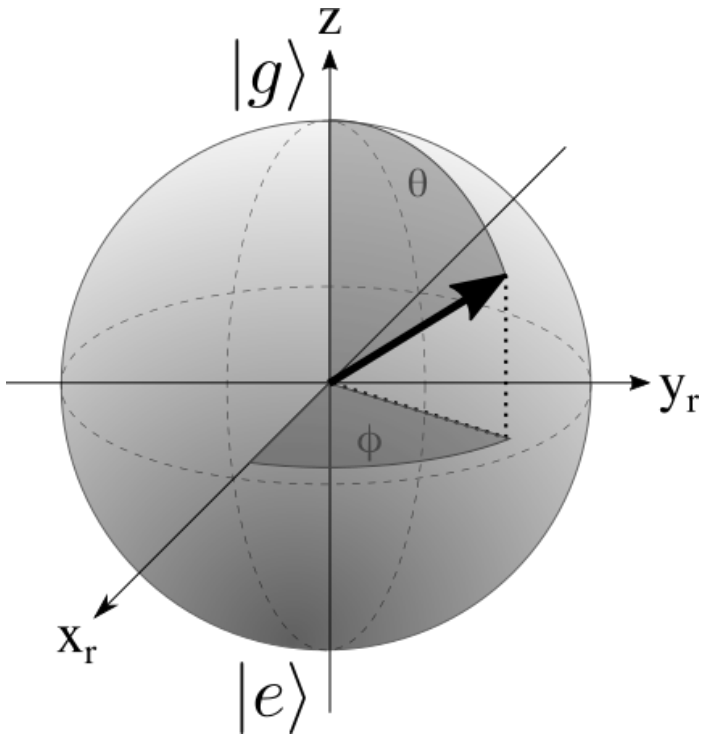

Figure 2.4: Bloch sphere representation of a two-level system quantum state, $|\psi\rangle = \cos(\theta/2)\,|g\rangle + \sin(\theta/2)e^{i\phi}\,|e\rangle$.

If we apply this field as a pulse for a time t_p, the flip angle will be

$$\alpha = \omega_1 t_p = g\mu_B B_1 t_p/\hbar \tag{2.70}$$

to flip the spin a quarter ($\pi/2$ pulse) or half rotation (π pulse), we apply pulses of lengths $t_{\pi/2} = \pi\hbar/(2g\mu_B B_1)$ and $t_\pi = \pi\hbar/(g\mu_B B_1)$. These are the fundamental operations that make up the majority of pulse sequences used in pulsed ESR. For these pulse lengths to be much shorter than the relevant time scales in our system, such as relaxation times, the pulses are amplified quite strongly. The resultant pulse lengths are often in the tens to hundreds of nanoseconds range.

2.2.6.1 Free induction decay

One of the simplest experiments that can be done is to apply a $\pi/2$ pulse and observe what happens. This flips the spins so that there is no net longitudinal magnetisation, but all of it is in the transverse component, rotating in the lab frame with the resonant frequency ω. When a spin rotates, it radiates energy into the resonator. When the phase distribution of the precessing spins is narrow enough, they radiate in phase and a signal is picked up with a low noise amplifier. The phase coherence is lost over time as described phenomenologically above, and so the signal decays. This signal is called free induction decay (FID), and for exponential decay e^{-t/T_2^*}, we can extract a decoherence time T_2^*.

2.2.6.2 Hahn echo

The FID is not a good way to measure the phase coherence time T_2 because the decay time measured is affected by static inhomogeneities in the local magnetic field at the spin locations. The slight variation in field makes different spins precess with slightly different frequency, and thus phase coherence is lost quicker than if the field was homogeneous, $T_2^* < T_2$. This can be illustrated by the spins "fanning out" on the Bloch sphere equator, as illustrated in Figure 2.5. The simple way to counteract this effect is to apply a π pulse to flip the spins by half a rotation more after a waiting period τ. The effect of this is to reverse the ,,fanning out", and the spins refocus in a single point on the Bloch sphere after a further time τ, producing a so-called Hahn echo signal. The intensity of this echo signal depends on τ, since there are decoherence events that can not be reversed by the π pulse. If we vary τ and plot the

echo intensity as a function of 2τ, the exponential decay of the resulting plot can give a good estimation of T_2 in some circumstances. In many cases, the decay is better fitted with a stretched exponential,

$$f(2\tau) = Ae^{-(2\tau/T_m)^n}, \tag{2.71}$$

often attributed to lattice relaxation dynamics of surrounding spins [37]. The parameter T_m is called the spin-echo phase memory.

A variation on the Hahn echo can be used to measure the longitudinal relaxation. First, a π pulse is applied, and after a time τ_1, a Hahn echo sequence with a τ relatively short compared to T_m is performed. The echo intensity is proportional to the magnetisation at the beginning of the Hahn echo sequence. By varying τ_1 and plotting the echo intensity, we observe the decay of the longitudinal magnetisation and can extract T_1.

2.2.6.3 Relaxation processes

Longitudinal relaxation (characterised by T_1) involves a loss of energy for the spin system. Spontaneous dipole emission is always present, but the rate is usually negligible in ESR [32]. The dominant mechanism for the exchange of energy is the thermal motion of the environment. The relaxation of spin in a solid is governed by coupling of the spin to phonons in the solid, called spin-lattice relaxation. The simplest one is the direct process, where a single phonon of frequency ω_s is absorbed or emitted by the spin. Depending on the temperature, a Raman process can be more efficient, where a phonon of a frequency $\omega_{\nu 1} \approx \omega_{\max}$ is absorbed and a phonon of frequency $\omega_{\nu 2} = \omega_{\nu 1} \pm \omega_s$ is emitted. This involves the spin jumping to a virtual higher energy

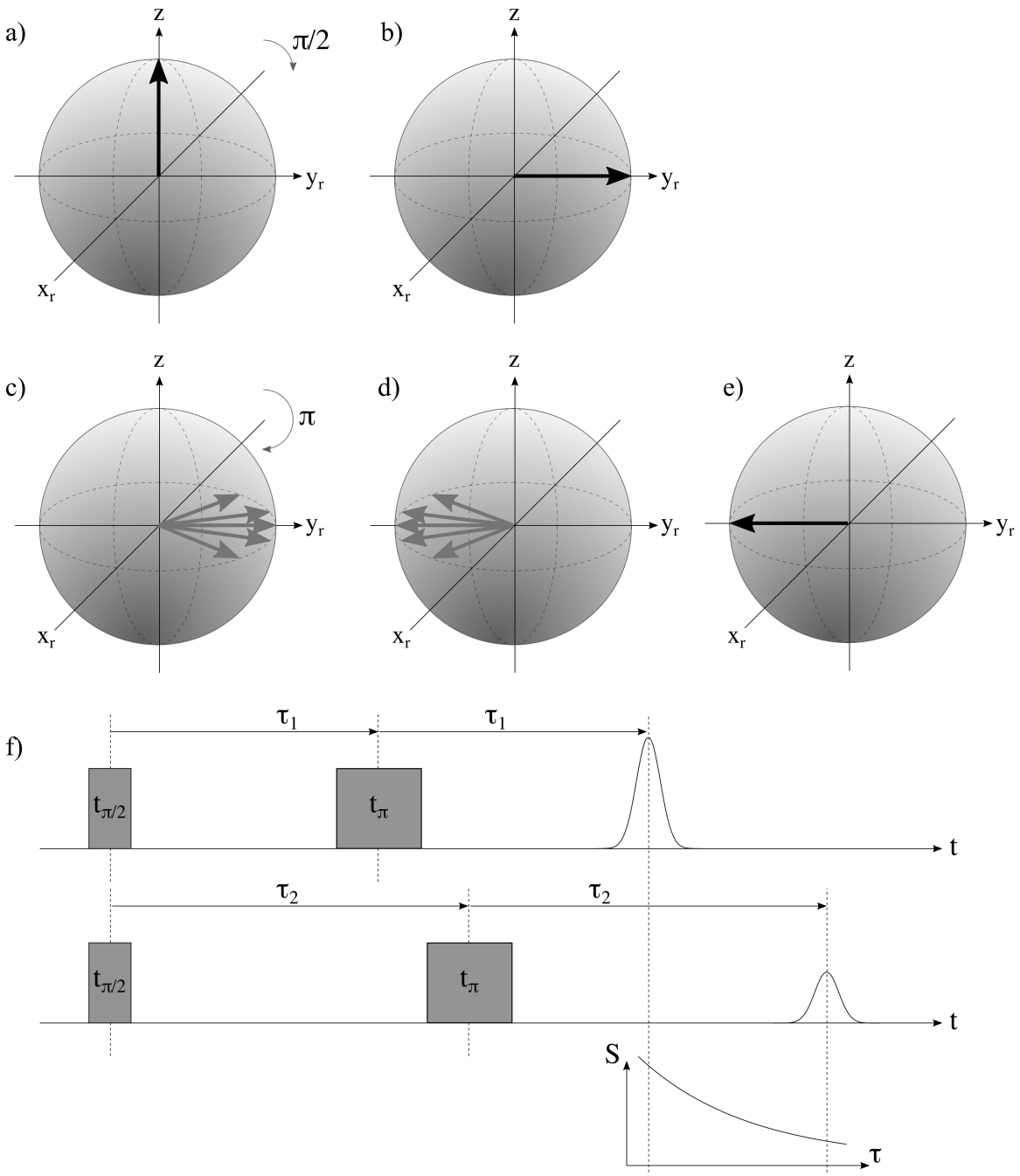

Figure 2.5: Schematic of a Hahn echo pulse sequence. (a) Starting with the system in the pseudospin in the ground state, a $\pi/2$ pulse is applied to flip the spin to a superposition of ground and excited state (b). (c) The ensemble of spins spreads around the Bloch sphere due to inhomogeneities in the field. After a time τ, a π rotation is applied around the same axis as the $\pi/2$ pulse (d). This causes the spins to refocus on the opposite side of the Bloch sphere after another τ period (e). (f) Varying τ and plotting the intensity of the echo gives a characteristic decay curve, yielding the echo phase memory T_m.

state intermediately. If there is an actual excited energy level of the spin involved, the process is more efficient and called an Orbach process.

Transverse relaxation does not need to include an exchange of energy with the environment. A longitudinal relaxation spin flip also destroys the phase correlation of that spin with the other spins, and so contributes to the transverse relaxation. But the process where two spins interact and exchange their states (flip-flop) is twice as efficient at destroying coherence as it involves two spins. If flip-flops happen at rate $1/T_2'$, the transverse relaxation rate is then

$$\frac{1}{T_2} = \frac{1}{T_2'} + \frac{1}{2T_1}, \tag{2.72}$$

meaning $T_2 \leq 2T_1$.

There are other processes that can contribute to relaxation (see e.g [32]), and some of them depend on how the spins are excited and measured. Instantaneous diffusion is an imperfection in the refocusing of a Hahn pulse due to the surrounding spins of the spin being measured also getting flipped during the π pulse, slightly modifying the local magnetic field inhomogeneously throughout the sample. Spectral diffusion is a similar phenomenon which is due to flips of surrounding spins that were not excited by the narrow-band pulse (called B spins).

2.3 Spin-lattice interaction

Although electron spins are most commonly manipulated by magnetic field through the magnetic dipole interaction, section 2.2.4.2 hints that there is another way to modify the spin Hamiltonian of spins in crystal hosts. Deforming the crystal lattice affects the crystal field effect parameters by changing the relative distances between the spins and the surrounding lattice ions. Static strain applied to the crystal can thus change the energy levels, and lattice vibrations can resonantly excite spins just like an oscillating magnetic field.

A phenomenological approach to the interaction of lattice vibrations with spin impurities is discussed in [33]. Taking into consideration lattice effects on the $\boldsymbol{g}$ tensor and hyperfine splitting as well as the zero-field splitting $\boldsymbol{D}$, the Hamiltonian containing the interaction terms can be written as

$$\begin{aligned} H =& \beta \boldsymbol{B} \cdot \boldsymbol{g} \cdot \boldsymbol{S} + \boldsymbol{S} \cdot \boldsymbol{D} \cdot \boldsymbol{S} + \boldsymbol{I} \cdot \boldsymbol{A} \cdot \boldsymbol{S} + \\ & \beta \boldsymbol{B} \cdot \boldsymbol{h} \cdot \boldsymbol{S} + \boldsymbol{S} \cdot \boldsymbol{d} \cdot \boldsymbol{S} + \boldsymbol{I} \cdot \boldsymbol{a} \cdot \boldsymbol{S} \end{aligned} \tag{2.73}$$

where the last three terms are the dynamic counterparts of the first three terms, and depend on the strain $\boldsymbol{\epsilon}$ of the lattice through fourth rank tensors:

$$d_{ij} = \sum_{k,l} G_{ijkl} \epsilon_{kl} \tag{2.74}$$

$$h_{ij} = \sum_{k,l} F_{ijkl} \epsilon_{kl} \tag{2.75}$$

$$a_{ij} = \sum_{k,l} Z_{ijkl} \epsilon_{kl}. \tag{2.76}$$

Strain is a unitless measure of the deformation of a crystal, which is defined in Section 2.4.1. The symmetry of the crystal determines the number of non-zero and

independent components of the tensors $\boldsymbol{G}$, $\boldsymbol{F}$ and $\boldsymbol{Z}$, and in many cases one of the three terms dominates. For example, we will only be concerned with the $\boldsymbol{G}$ tensor, which constitutes a modulation of the zero-field splitting, and this tensor can always be written in Voigt notation. For example, for both ZnO (C_{6v}) and lithium niobate (C_{3v}), the equations defining the independent components are

$$G_{13} = -\frac{1}{2}G_{33} \tag{2.77}$$

$$G_{31} = -(G_{11} + G_{12}) \tag{2.78}$$

i.e. there are three independent components.

Crystal strain can thus be used to tune spin energy levels, but also to resonantly excite spin transitions by applying an AC strain.

2.3.1 Piezoelectric crystals

If the crystal containing the spins is piezoelectric, one way to induce strain is to apply an electric field. This allows for a much simpler way to probe spin-lattice interaction. In fact, the theory can be centred on the effect of electric fields on spin resonance, and the phenomenon is then often referred to as linear electric field effect (LEFE) [35]. There are two classes of experiments to be performed; applying static electric fields and seeing how it affects the energy levels of the spins, or applying oscillating electric fields and observing resonant transitions, referred to as paraelectric resonance. In the former, if the LEFE is large enough, the shift of the resonances with electric field can be directly observed in the EPR spectrum, or the magnetic field modulation can be exchanged for electric field modulation and the signal strength then analysed. For a

more sensitive measurement, a pulsed experiment can be performed where a simple Hahn echo is modified by applying a static electric field pulse either before or after the π pulse. The difference in transition energy causes the spins to precess with different speeds before and after the π pulse, and the difference will determine the phase of the final echo.

2.3.2 Axial anisotropy

In the crystal symmetries that we are concerned with, the static crystal field Hamiltonian $H = DS_z^2$ describes an axial anisotropy. However, Equation (2.77) shows that strain along various axes has the potential to modify the anisotropy and introduce non-axial terms to the Hamiltonian. It is thus not trivial to fully explain the spin-lattice coupling unless the full $\boldsymbol{G}$ tensor is known.

Some approximations and simplifications can be made to move forward. Let's assume that we have a $S = 5/2$ system with an axial anisotropy ($H = DS_z^2$), as most of our experiments do. If a static electric field E_z is applied along the c axis of the crystal, this will only modify the parameter D and not add a parameter E as in Equation (2.44), since an axially applied field will affect the x and y axes equally. Any change in the energy levels will then be attributed to a modification of D. For small fields, the effect is linear,

$$D = D_0 + \kappa E_z \tag{2.79}$$

where D_0 is the zero-field splitting without an electric field applied, E_z the electric field along the z axis, and κ is a proportionality constant. Note that the effect only occurs in crystals with broken inversion symmetry, which validates the linear nature

Table 2.1: Energy shifts of the transitions in a $S = 5/2$ system with axial anisotropy with an electric field E_z applied along the anisotropy axis.

Transition	ΔE
$\pm 1/2 \rightarrow \mp 1/2$	0
$\pm 1/2 \rightarrow \pm 3/2$	$\pm 2\kappa E_z$
$\pm 3/2 \rightarrow \pm 5/2$	$\pm 4\kappa E_z$

of the effect. The change in transition energy with applied electric field depends on the states involved in the transition:

$$\Delta E = \kappa E_z (m_{s,f}^2 - m_{s,i}^2). \tag{2.80}$$

For $S = 5/2$, Table 2.1 summarises the shifts. These shifts can as earlier described be measured by direct observation of the resonance shift on an ESR spectrum, or by applying pulsed static electric fields in pulsed ESR experiments and observing phase shifts.

As we only need to consider contributions from strain along the z axis, we can write

$$D = D_0 + G_{33}\epsilon_3 = D_0 + G_{33} d_{33} E_z \tag{2.81}$$

where d_{33} is a piezoelectric coefficient. If we extract κ, we can thus easily calculate

$$G_{33} = \kappa / d_{33}. \tag{2.82}$$

2.3.2.1 Resonant excitation with strain field

If a sinusoidally varying strain field is applied, it is possible to resonantly excite transitions between spin levels. For this to happen, the interaction Hamiltonian must not be diagonal, i.e. it must contain terms with $S_\pm$. For this to be the case, the

quantisation axis must not be parallel to the anisotropy axis. This can be ensured by applying the Zeeman magnetic field at an angle to the anisotropy axis. For ESR frequencies larger than the zero-field splitting we can approximate the quantisation z axis to be along the magnetic field. The Hamiltonian thus becomes

$$\begin{aligned} H =& H_0 + D(S_z\cos(\theta) + S_x\sin(\theta))^2 \\ =& H_0 + D\left(S_z^2\cos^2(\theta) + \frac{\sin(2\theta)}{2}S_z(S_+ + S_-) + \frac{1}{4}\sin^2(\theta)(S_+^2 + 2S_+S_- + S_-^2)\right). \end{aligned} \tag{2.83}$$

A resonant variation of D can thus excite both $\Delta m_s = \pm 1$ and $\Delta m_s = \pm 2$ transitions, depending on the orientation of the magnetic field. The single transitions are maximised at $\theta = 45°$ while the double transitions are maximised at $\theta = 90°$, at which angle no single transitions should be seen.

2.3.2.2 Non-axial strain

As mentioned earlier, applying non-axial strain can modify the E crystal field parameter as well as D, even if $E = 0$ without applied stress. This means that there can be strain-mediated transitions at any field angle, and in particular when the field is parallel to the anisotropy axis, as shown in the work of MacQuarrie *et al.* [29].

2.3.3 Literature review

2.3.3.1 Acoustic paramagnetic resonance

There has in fact been a fair amount of work done in the field of acoustic paramagnetic resonance decades ago [33]. The most common approach is to use a pulse-echo method. The sample is in form of a crystal rod with paramagnetic ion impurities,

mounted on a piezoelectric transducer. A short pulse of up to 10 GHz frequency is sent to the transducer and gets converted to an acoustic pulse that travels through the rod, gets reflected at the end, and picked up again at the transducer. Measuring the amplitude of the echo while sweeping magnetic field allows to plot the attenuation as a function of field.

Another approach is to essentially do CW-EPR, but with the mechanical resonance of a sample rod instead of a microwave cavity. It is difficult to get higher frequencies than about 1 GHz using sample rod resonances, which is why the pulsed method was more common.

2.3.3.2 LEFE of Mn^{2+} spins in ZnO

Previous work in Prof. Arzhang Ardavan's group was the inspiration for this project. In the publication of Richard George *et al.* [38], Mn^{2+} impurities ($S = 5/2$) in ZnO were investigated with ESR techniques. The spin system has an axial zero-field splitting of $D \simeq 708$ MHz, with additional hyperfine splitting of about $A = 221$ MHz [39]. Firstly, the linear electric field effect was measured by evaporating electrodes to opposing sides of the sample and applying an electric field pulse within a spin-echo sequence as described above. They extracted a LEFE coefficient for the zero-field splitting of $\kappa = 20.8 \pm 0.2$ rad s^{-1}/Vm^{-1} (see Equation (2.79)). Secondly, the LEFE was used to drive electric dipole transitions, by placing the sample in an electric field antinode in the ESR resonator rather than the usual magnetic field antinode. The angle was varied to show that the transitions vanish when the c axis is parallel to the static magnetic field, and increase linearly in amplitude with angle to first order.

Hamiltonian parameter	Value [MHz]
D	-1780 ± 3
a	117 ± 15
F	12 ± 15

Table 2.2: Table with Hamiltonian parameters for Fe:ZnO, measured by Walsh *et. al.*. [40]

2.3.3.3 Fe^{3+} in ZnO

An early ESR investigation of Fe^{3+} in ZnO [40] determined the Hamiltonian parameters as listed in Table 2.2. They did not notice any measurable temperature dependence of the parameters.

A study by Tribollet *et al.* [41] praises Fe^{3+} in ZnO for its very long coherence time and suggests it as a potential spin qubit. They measured an instantaneous diffusion-limited spin coherence time of $T_m \approx 150$ µs at $T = 6$ K with a standard Hahn echo decay method. Beyond instantaneous diffusion, the coherence time is limited by nuclear spectral diffusion at ≈ 450 µs, and finally at ≈ 1.4 ms by spin-lattice processes. The authors suggest that a single spin could be read out with optical methods and coherently manipulated with pulsed ESR techniques, citing work [42] where the coherent dynamics of a single Mn^{2+} spin in a CdTe quantum dot was measured using optical pump-probe methods.

2.3.3.4 Fe-doped lithium niobate

Lithium niobate ($LiNbO_3$) is a material widely used in surface acoustic wave applications because of its very large piezoelectric effect. The acousto-electric coupling is about an order of magnitude higher than that of ZnO.

Iron doped lithium niobate (Fe:LN) is used in holographic memory applications due to its strong photorefractive effect. It is thus commercially available in various doping strengths. In as-grown Fe:LN, grown with the Czochralski method, the ratio of Fe^{2+} ions over Fe^{3+} is about 0.1-0.2 [43]. This ratio can be altered with a redux process by annealing in H_2 [44], or an argon-oxygen mixture, with increased efficiency when packed in Li_2CO_3 powder [45].

Due to its highly polar character, spin impurities in lithium niobate can have very large zero-field splittings. For example, Fe^{3+} in lithium niobate has a zero-field splitting parameter D close to 5 GHz [46] . However, for maximising spin-lattice coupling, the Fe^{2+} ion is of particular interest. Theoretical work reports very large D and G_{ij} parameters. In reference [47], Hamiltonian parameters are calculated theoretically, as summarised in Table 2.3. The values are different depending on whether the Fe^{2+} ion is on the Li or Nb site, but the preferred site is Li [43]. This enormous D value means that it is impossible to observe $\Delta m_s = \pm 1$ with traditional ESR. However, the $m = \pm 1$ states are degenerate at zero-field (for $E = 0$), and are split continuously with the Zeeman field. It is thus possible to see the forbidden $|m_s = -1\rangle \leftrightarrow |m_s = +1\rangle$ transition if the excitation method allows it, for example using a parallel mode ESR resonator, or with acoustic excitation. One paper reports absorption through the $|m_s = -1\rangle \leftrightarrow |m_s = +1\rangle$ transition, using thermally detected ESR and placing the sample in a resonant electric field [48]. Here, they claim zero-field splitting parameters $D \simeq 450$ GHz and a non-Gaussian distribution of E up to a maximum of $E \simeq 6$ GHz.

One of the difficulties with performing spin physics experiments using commercially

Table 2.3: Theoretically calculated parameters for the Fe^{2+}:LN system [47].

	Li site	Ni site
g_1	2.78	2.97
g_3	2.0	2.0
D	1.16 THz	1.45 THz
G_{33}	-7.28 THz/strain	-45.6 THz/strain
G_{11}	2.50 THz/strain	9.35 THz/strain

available lithium niobate is that it is usually highly non-stochiometric (often called congruent), i.e. the ratio of Li to Ni atoms is not 1 [49, 43]. This means that the direct environment of the magnetic ions is quite variable, resulting in inhomogeneous broadening due to the distribution of Hamiltonian parameters. The resulting linewidths can be quite broad, on the order of hundreds of Gauss for Fe^{3+} [49]. There have been advances in growing near-stochiometric lithium niobate, but acquiring such crystals with high concentration of magnetic impurities is non-trivial. One method that can be easily tried is to introduce the dopant into pure stoichiometric crystal by diffusion [50].

Recently, a low temperature study of the coupling of Fe^{3+}:LN to an electromagnetic mode was done using whispering gallery modes [51]. Quality factors of the WGM ranged from about 10^4 to 10^5, and the doping amount was 0.005 wt %. The summary concludes that although spin coupling was easily visible, strong coupling was not achieved. They state that increasing the Fe concentration would not help either, as the ensemble losses would offset the gain in coupling strength. However, this claim is not supported with data, and it is also not clear whether they used near-stochiometric material or congruent.

2.3.3.5 Coherent control of NV centres with mechanical resonator

Significant advances have recently been made on coupling mechanical resonators to spin qubits using NV centres in diamond. Using a bulk-mode mechanical microresonator on single crystal diamond containing about 10^{12} NV/cm^3, a Rabi oscillation of $\Omega_R/2\pi = 3.8$ MHz was achieved. An interesting part of this research is that the transition that was coherently manipulated was the $|-1\rangle \leftrightarrow |+1\rangle$ magnetically forbidden transition. The Hamiltonian used in the paper is the following:

$$H_{\mathrm{NV}} = (D_0 + \epsilon_{\parallel}\sigma_{\parallel})S_z^2 + PI_z^2 + A_{\parallel}I_zS_z + \gamma_{\mathrm{NV}}B_{\parallel}S_z \tag{2.84}$$

$$+\gamma_{\mathrm{NV}}B_{\perp}S_x - \epsilon_{\perp}\sigma_x(S_x^2 - S_y^2) + \epsilon_{\perp}\sigma_y(S_xS_y + S_yS_x) \tag{2.85}$$

where σ is the mechanical stress. As the NV in a single crystal has four possible ways to orient itself (tetrahedral symmetry), choosing to orient the magnetic field along one of them will put three quarters of the NVs at an angle of $\theta = 70.5°$ to the field. In the paper, the resonance corresponding to the NV centres aligned parallel to the magnetic field is addressed and thus the $\epsilon_{\perp}$ coefficient is the term responsible for coupling the $m_s = \pm 1$ levels through mechanical stress. However, as the static magnetic field defines the spin quantisation axis, the $\epsilon_{\parallel}$ term should contribute as well if the same experiment were performed on the resonance corresponding to the $\theta = 70.5°$ NVs.

2.3.3.6 Optomechanical control of NV centres using SAW mode

A very recent publication reports coupling of SAWs to the internal electronic states of NV centres in diamond [30]. The NV centres are first initialised in their $|m_s = 0\rangle$

state with a 532 nm laser. From there, an optical transition at $\lambda = 637$ nm to an excited state $|E_y\rangle$ exists. Lattice vibrations couple to this state, so when a high-powered SAW wave of 900 MHz is applied, sidebands appear on either side of the $\lambda = 637$ nm transition. The sideband resonances were used to drive Rabi oscillations. Although this is not technically an experiment coupling different spin states using acoustic excitation, it is closely related and interesting due to the very large coupling coefficient of 610 THz/strain.

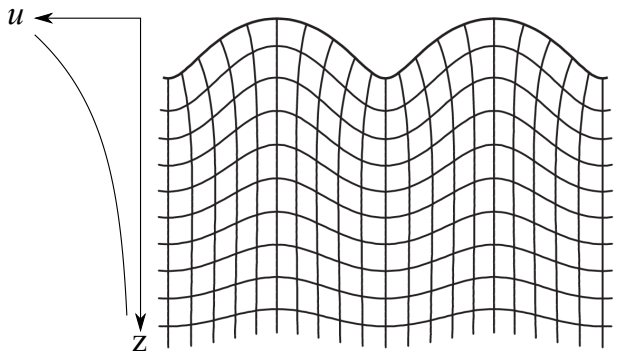

Figure 2.6: Visualisation of a Rayleigh wave, an acoustic mode bound to the surface of a solid, exponentially decaying into the material and travelling along the surface.

2.4 Surface Acoustic Waves

As explained in the previous section, lattice vibrations can be used to drive electron spin resonances. Bulk modes and resonators such as cantilevers have been used, but one type of acoustic resonance that has only very recently (research published in the late stages of the current project [30]) been successfully used for electron spin resonance is surface acoustic waves (SAWs). These are mechanical waves that are localised to the surface of a material. They were first described by Lord Rayleigh [52], giving the name to one of the various SAW modes, Rayleigh waves (see Figure 2.6). Their existence spans all the way from the seismic scale of earthquakes down to the micrometer scale of electronics. Piezoelectric crystals are a crucial ingredient in SAW devices, since this couples the mechanical strain to an electric field, making the waves excitable by applying AC electric fields.

2.4.1 Theory

Acoustic waves in solids are variations of the relative positions of atoms, and the physics is governed by elastic equations of the solid material. For a simple, non-

piezoelectric solid, this is just a generalisation of Hooke's law ($F = -k\Delta x$):

$$T_{ij} = \sum_{kl} c_{ijkl}\epsilon_{kl} \tag{2.86}$$

where ϵ is the strain in the solid, T is the stress, and c is the elasticity tensor. Indices run over the three space dimensions. The strain can be defined in a symmetrised way

$$\epsilon_{ij} = \frac{1}{2}\left(\frac{\partial u_i}{\partial x_j} + \frac{\partial u_j}{\partial x_i}\right) \tag{2.87}$$

where $\boldsymbol{u(x)}$ is the mechanical displacement at the point $\boldsymbol{x}$. The stress describes the internal forces in the solid, and $T_{ij}(\boldsymbol{x})$ is defined as the force per unit area applied in the i direction, on the plane perpendicular to the j direction. Thus, T_{ij} describes compressive and tension forces when $i = j$, and shear forces when $i \neq j$. It can be shown that $T_{ij} = T_{ji}$.

The elasticity tensor c_{ijkl} has 81 elements, but due to the symmetries of the stress and strain, i and j can be interchanged, as well as k and l, and furthermore ij can be swapped with kl, resulting in a maximum of 21 independent elements. Crystal symmetry usually reduces this number much further. The symmetry of two indices i, j gives rise to the Voigt notation, where i, j can be represented with a single index n. For $i = j$, one writes $n = i$. For $i \neq j$ one defines $n(i = 2, j = 3) = 4$, $n(i = 1, j = 3) = 5$, $n(i = 1, j = 2) = 6$. The numbering is defined by the equation $n = 9 - i - j$ for $i \neq j$. The 4-dimensional tensor can thus be represented with a two-dimensional matrix c_{mn}.

2.4.1.1 Equations of motion

The equation of motion is obtained by considering the forces on an elementary cube of volume δ^3 located at $\boldsymbol{x}'$. The net force in direction i depends on the difference of T_{ij} from one side of the cube to the other, and for an infinitesimal δ we find the total force to be

$$\delta^3 \sum_j \frac{\partial T_{ij}(\boldsymbol{x}')}{\partial x_j}. \tag{2.88}$$

The mass of the cube is $\rho\delta^3$, so using Newton's law we find the equation of motion

$$\rho \frac{\partial^2 u_i}{\partial t^2} = \sum_j \frac{\partial T_{ij}}{\partial x_j} = \sum_{jkl} c_{ijkl} \frac{\partial^2 u_l}{\partial x_j \partial x_k}. \tag{2.89}$$

2.4.1.2 Piezoelectric material

The equations coupling the electric field with the mechanical displacements in a piezoelectric crystal are in the stress-charge form [53]

$$T_{ij} = \sum_{kl} c^E_{ijkl} \epsilon_{kl} - \sum_k e_{kij} E_k \tag{2.90}$$

$$D_i = \sum_j \varepsilon^S_{ij} E_j + \sum_{jk} e_{ijk} \epsilon_{jk} \tag{2.91}$$

where e is the piezoelectric tensor, ε^S the permittivity for constant strain, E the electric field, D the electric displacement field and c^E is the elasticity tensor at a constant electric field. The indices j, k of the piezoelectric tensor can be contracted using Voigt notation.

Using Eq. (2.90) and Newton's second law, we get the equation of motion

$$\rho \frac{\partial^2 u_i}{\partial t^2} = \sum_{jkl} c^E_{ijkl} \frac{\partial^2 u_l}{\partial x_j \partial x_k} + \sum_{kj} e_{kij} \frac{\partial^2 \Phi}{\partial x_j \partial x_k}, \tag{2.92}$$

and Poisson's equation,

$$\nabla \cdot \boldsymbol{D} = \sum_{ijk} e_{ijk} \frac{\partial^2 u_k}{\partial x_i \partial x_j} - \sum_{ij} \varepsilon_{ij}^S \frac{\partial^2 \Phi}{\partial x_i \partial x_j} = 0 \tag{2.93}$$

where Φ is the electric potential, $\boldsymbol{E} = -\nabla\Phi$. This is justified because the magnetic field arising through Maxwell's equations is negligibly small due to the low velocity of the wave.

With the above equations one can in principle derive the SAW modes for any crystal orientation, given a reasonable ansatz for the form of the solution. This includes a harmonic plane wave behaviour in the direction of propagation and an exponential decay into the crystal. The mechanical and electric boundary conditions need also be considered. As there is no variation of the mode in-plane perpendicular to the propagation direction, the electric field is constrained to the sagittal plane (the plane spanned by the crystal surface normal and the direction of propagation vector).

Determining the analytical solution of a SAW mode can be a difficult task, and a fairly simple way to get around it is to use a simulation tool such as Comsol [1] to find the eigenmodes corresponding to the SAW modes. It is straightforward to verify that it is the desired SAW mode visually, and the resonant frequency, SAW velocity and strain distribution are immediately available.

2.4.2 SAW devices

The fundamental building blocks in SAW device fabrication are interdigital transducers (IDTs, see Fig. 2.7), which transform an electrical signal into an acoustic one

[1] https://www.comsol.com/

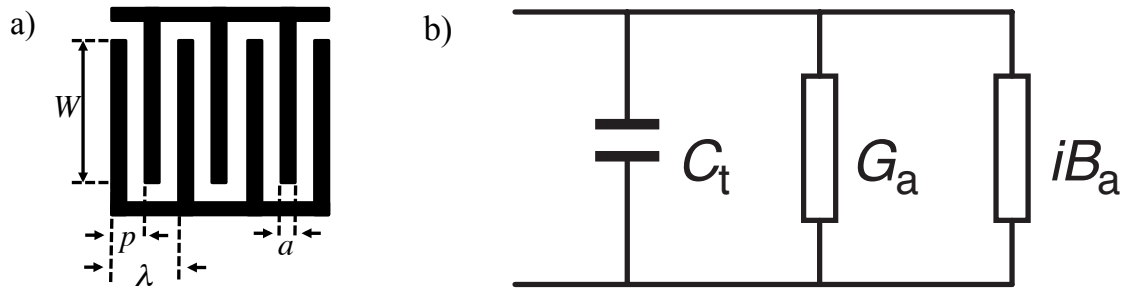

Figure 2.7: Interdigital transducer (IDT) with the parameters defined: finger width a, pitch p, wavelength λ and aperture width W. Alternating voltage is applied between the two electrodes to generate a SAW. b) The equivalent circuit of an IDT, with C_t the IDT capacitance, G_a the acoustic conductance and B_a the acoustic susceptance.

and vice versa. To model the response of a SAW device, it is often abstracted to the level of an electric circuit that is equivalent in impedance near the resonant frequency. With that in mind, let us consider the devices from an electric circuit point of view.

A frequently used property is the admittance Y, which is the inverse of impedance, i.e. $Y = I/V$. The admittance of a single IDT is modelled by an acoustic conductance G_a to allow for the electric energy to be dissipated into the acoustic mode, a susceptibility B_a to allow for phase shifts and the capacitance C_t between the two combs of the IDT. The total admittance is therefore

$$Y_t(\omega) = G_a(\omega) + i(B_a(\omega) + \omega C_t). \tag{2.94}$$

A careful analysis [53] of the acoustic conductance in the case of the simplest type of IDT (uniform width W, regular spacing with $a/p = 0.5$) gives a result close to the central frequency $\omega_c = 2\pi v/(2p)$

$$G_a(\omega) \simeq G_a(\omega_c) \left[\frac{\sin X}{X}\right]^2 \tag{2.95}$$

$$B_a(\omega) \simeq G_a(\omega_c) \frac{\sin(2X) - 2X}{2X^2} \tag{2.96}$$

with

$$G_a(\omega_c) = 2.87\omega_c N_p^2 W \frac{\Delta v}{v}\varepsilon_\infty, \quad X = \pi N_p(\omega - \omega_c)/\omega_c, \tag{2.97}$$

where v is the free surface velocity of the SAW mode, $\Delta v = v - v_m$ where v_m is the metallised surface velocity, N_p is the number of electrode pairs, W is the aperture width of the IDT and $\varepsilon_\infty \simeq \varepsilon_0 + \sqrt{\varepsilon_{11}\varepsilon_{33} - \varepsilon_{13}^2}$ is an effective permittivity. This result explains why the parameter $\Delta v/v$ is called the coupling coefficient for a specific SAW mode. Without going into detail, the shape $\frac{\sin X}{X}$ comes from the Fourier transform of the charge density on the IDT, which is a periodic rectangular function.

For a delay line, a device with two IDTs, the amplitude of the admittance between the two is a product of the respective conductances:

$$|Y_{12}| = \sqrt{G_a^a(\omega)G_a^b(\omega)}. \tag{2.98}$$

However, when the two transducers are connected to load impedances, a more useful approach is to relate the incoming and outgoing voltage signals at each transducer by the S-matrix:

$$\begin{bmatrix} V_{o1} \\ V_{o2} \end{bmatrix} = \begin{bmatrix} S_{11} & S_{12} \\ S_{21} & S_{22} \end{bmatrix} \begin{bmatrix} V_{i1} \\ V_{i2} \end{bmatrix} \tag{2.99}$$

where V_{i1}, V_{i2} are the incoming voltage signals and V_{o1}, V_{o2} are the outgoing voltage signals of IDT 1 and 2, respectively. This is precisely what is measured with a vector network analyser (VNA), which has standard load impedances $Y_0 = 50\ \Omega$. The values of the S-matrix can then be related to the admittance matrix and the applied external load on the IDTs Y_0. For the transmission from port 1 to port 2, the result is

$$|S_{21}| = \frac{2G_a^2(\omega_c)}{Y_0^2}\left[\frac{\sin X}{X}\right]^4. \tag{2.100}$$

2.4.2.1 SAW resonators

Periodic grooves or metallic electrodes (gratings) can behave as high quality SAW reflectors, since surface discontinuities reflect part of the SAW. These periodic reflectors are analogous to Bragg reflectors for light. To create a SAW resonator, one or two IDTs are placed in between two mirror gratings (see Figure 2.8), depending on whether a reflection or transmission measurement is desired. The internal quality factor Q_i of the resonator depends on multiple parameters such as substrate loss, electrode/grating loss, reflectivity of the mirror gratings, and distance between the gratings. An experimental survey of some of these parameters can be found in Riccardo Manenti's paper [54]. The external quality factor Q_e is determined by the coupling strength of the IDT to the SAW mode, and can be estimated with the formula

$$Q_e = \frac{1}{5.74 v_0 Z_C C_S W K^2} \frac{L_c}{N_p^2} \tag{2.101}$$

where Z_c is the impedance of the electrical port leading to the IDT, C_s is the capacitance of a single pair of fingers, W is the width of the IDT, $K^2 = 2\Delta v/v$, L_c is the cavity length and N_p is the number of finger pairs.

The reflection coefficient of a one-port resonator is

$$S_{11}(f) = \frac{(Q_e - Q_i)/Q_e + 2iQ_i(f - f_0)/f}{(Q_e + Q_i)/Q_e + 2iQ_i(f - f_0)/f} \tag{2.102}$$

which describes a circle in the complex plane. Impedance mismatches can cause the circle to get rotated around the point $1 + 0i$, and this is phenomenologically modelled by rearranging the above equation and adding a rotation ϕ [55]:

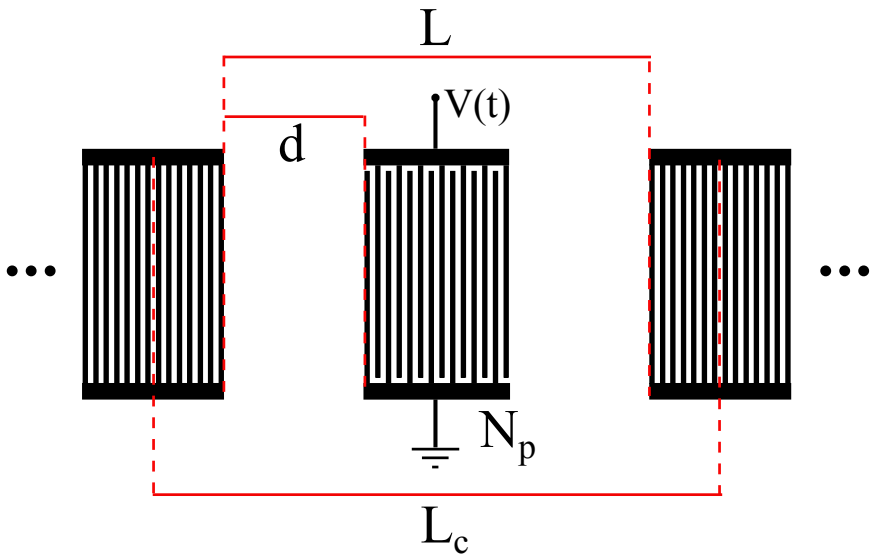

Figure 2.8: Schematic of a one-port SAW resonator. The effective cavity length L_c is larger than L due to the SAW penetration length into the gratings.

$$S_{11}(f) = 1 - \frac{2Q_i/Q_e}{(Q_e + Q_i)/Q_e + 2iQ_i(f - f_0)/f} e^{i\phi}. \tag{2.103}$$

Figure 2.9 shows plots of Equation (2.103) with $\phi = 0°$ and $\phi = 20°$ (dashed). When measuring resonators, one usually looks at the amplitude of the signal. The left plot shows what the asymmetry looks like on an amplitude plot. This model is a general one, and is appropriate for most one-port resonators, including coplanar waveguide resonators which will be a topic in this thesis. Spectral measurement data is fitted with equation (2.103) to extract Q_e and Q_i.

2.4.3 Literature review

Recently, advances have been made to measure single SAW phonons. In reference [56], a simple delay line is fabricated on GaAs and a single-electron transistor put in the path of the SAW between the two IDTs. The IDTs have fairly low reflectivity,

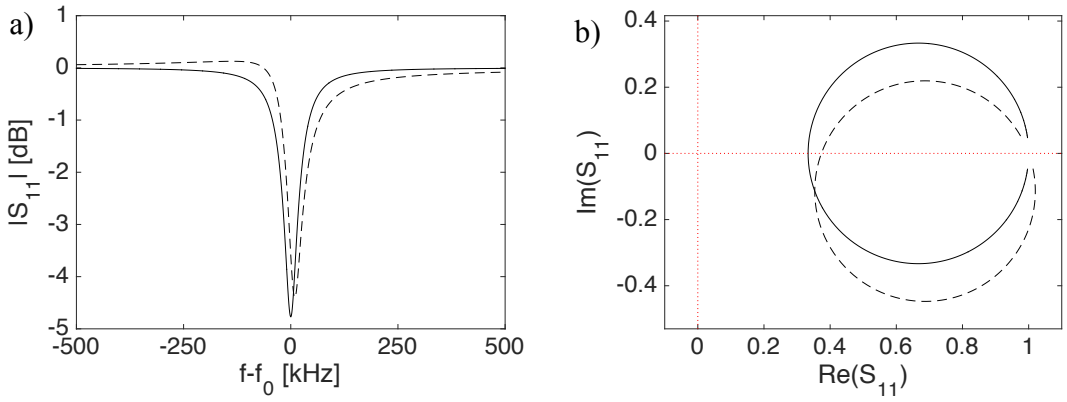

Figure 2.9: Reflection coefficient S_{11} plotted as amplitude (a) and in the complex plane (b). Dashed line corresponds to a 20° rotation due to impedance mismatching.

so there is not a strong cavity confinement of the SAW. However, the record-high sensitivity of the SET allowed Gustafsson et al. to measure single phonons that are freely propagating, after 10^7 averages. A few years later, the same group performed an experiment coupling freely propagating SAWs to a transmon-type superconducting qubit [57]. This allowed them to reproduce some effects from quantum optics, such as the reflection of the propagating SAW by the transmon at resonance, and the reflection saturation at single-phonon level.

In our own group, Riccardo Manenti has done an extensive study of SAW resonators at low temperature, expanding the state of knowledge on SAW propagation loss at low temperature and low power [54]. The propagation loss was found to follow a polynomial dependence on frequency, and a drive power dependent loss that saturates at low power and is consistent with coupling to a bath of two-level systems [58].

A major research goal in our group is to couple a transmon to a resonator-confined SAW mode, as opposed to the freely propagating SAW of Gustafsson *et al.*. In fact, it is clear that SAWs have the potential to play an important role in combining various

elements in circuit QED. This is well summarised by Schuetz *et al.* [16], where they propose basic SAW devices as ,,universal, on-chip quantum transducers" due to their beneficial properties.

2.4.3.1 SAWs for charge transport

SAWs are already an important concept in quantum technology research in the context of confined electrons. Semiconducting heterostructures and nanostructures in conjunction with gate electrodes can be used to define quantum dots electrostatically [59]. The electric potential of a SAW can act as a dynamic gate voltage to create moving quantum dots. This effect can be used to provide charge pumping between reservoirs through a semiconducting structure such as an electrostatically defined 1D channel in a 2D electron gas [60] or a carbon nanotube [61].

2.4.3.2 SAW excitation of spin waves

In magnetostrictive materials, elastic strain modifies the magnetic susceptibility of the ferromagnetic material. This property has recently been utilised to resonantly couple SAWs to spin waves [62] and subsequently generate spin currents using SAWs [63].

2.4.3.3 Previous work on SAWs with ZnO

Most work on ZnO SAW devices has been focused on ZnO films deposited on top of substrates such as Si, SiO_2/Si, GaAs, quartz, sapphire, SiC and diamond [64]. The reason for this seems to be that lower propagation loss can be achieved, as well as higher phase velocities and thus higher frequencies. Weber *et al.* [65] investigated ZnO

films on a SiO_2/Si substrate, with ZnO thicknesses of $h/\lambda = 0.4$ and 0.04 [65]. The fundamental Rayleigh mode for the thicker film has a propagation loss of 27 dB/m while for the thinner one it is only 7 dB/m. This suggests that the propagation loss of a SAW mode on thick film or bulk ZnO could be quite high, likely inhibiting its commercial use. However, these numbers are acquired at room temperature, and as will be seen later in this thesis, device characteristics are highly dependent on temperature. Another reason for the apparent lack of research with SAW devices on bulk ZnO substrates could be that it is only recently that high quality single-crystal bulk samples have been available [66].

2.5 Diffusion doping

As it can be difficult to acquire substrates with the right type and amount of impurity doping, introducing impurities to a nominally pure substrate by diffusion is a useful option. The diffusion of impurities in a solid can be described by Fick's first and second law [50]:

$$J = -D\nabla C \tag{2.104}$$

$$\frac{\partial C}{\partial t} = \nabla(-J) \tag{2.105}$$

where C is the concentration of impurities, J is the flux of impurities, and D is the diffusion coefficient. D can depend on many things, and often depends on temperature according to the Arrhenius equation:

$$D = D_0 e^{-E_A/kT} \tag{2.106}$$

where E_A is an activation energy related to the energy barrier the impurity must overcome to diffuse through the crystal. The coefficient is often vanishing at room temperature, so diffusion is induced by annealing the crystal for a period of time. To find out the final impurity density profile, Equations (2.104)-(2.105) are solved with proper boundary conditions. For the simplified case of an initial delta function at the surface, the result is a Gaussian distribution:

$$C(x) = \frac{N}{\sqrt{\pi Dt}} e^{-x^2/(4Dt)}. \tag{2.107}$$

The solution for an infinite point source, on the other hand, has the shape of a complementary error function. Depositing a thin layer of impurities at the surface

and diffusing the whole layer into the crystal over a period of time does not fully correspond to either of those cases, but if the standard deviation of the final impurity distribution in the crystal is much larger than the thickness of the initial layer, it is well approximated by the Gaussian distribution above.

It has been reported that lattice deformation of the lithium niobate crystal doped with Fe depends on both the Fe concentration and $[Fe^{2+}]/[Fe^{3+}]$, i.e. the degree of reduction [67]. It is important to keep in mind that this deformation may be large enough to cause strain in the D parameter, and thus a broadening of the linewidth.

Chapter 3

Experimental equipment and methods

During the course of this project, multiple different measurement setups have been used for our experiments. Standard ESR spectrometers were used to characterise spin systems and a low temperature dilution refrigerator was employed to characterise SAW devices. More customised setups have been used in experiments investigating magnetic field dependence of devices. A split coil superconducting magnet was constructed for magnetic field dependent experiments in the dilution refrigerator, and a custom setup was also used for our SAW-spin coupling experiments. In this chapter we review the different experimental setups and methods used in the project.

3.1 Electron spin resonance

3.1.1 Continuous wave measurements

Most of the electron spin resonsnce (ESR) measurements done in this thesis were performed with a Bruker E680 spectrometer that can be used for both continuous wave (CW) and pulsed measurements at either X band or W band. The CW measurement

setup consists of a microwave bridge, which has a tuneable microwave source to apply power to the sample, and a sensitive diode to measure the signal coming back [36] (see Figure 3.1). The bridge output is connected to a microwave resonator with tuneable coupling, and the sample is placed in the resonator. There are two reasons to use a resonator. Firstly, the enhanced B_1 field makes for higher absorption. Secondly, the way the signal is measured in the experiment is based on critically coupling the resonator. When the resonator is critically coupled, there is nearly zero reflection of the signal back to the microwave bridge. When the magnetic field is swept and the spin system brought into resonance with the microwave frequency, the spins start absorbing energy and the Q of the resonator drops. It is thus not critically coupled anymore and starts reflecting some of the incoming signal. This reflected signal is measured with the diode, and the intensity of this signal is directly proportional to the absorption in the sample.

To optimise the quality of the signal, two important measures are taken. Firstly, the measuring diode is put in its most linear range by mixing the incoming signal with a reference signal of appropriate amplitude and phase. Secondly, the static magnetic field B_0 is modulated at a typical frequency of $1 - 100$ kHz using small coils usually located in the resonator, and the signal is measured using a lock-in amplifier. This reduces the noise by orders of magnitude, but also results in the signal measured being the derivative of the absorption, as shown in Figure 2.3. Care should be taken not to over-modulate, i.e. keep the modulation amplitude ΔB_0 several times smaller than the width of the spin resonance, or the line shape will get distorted. The intensity of the signal depends on various parameters, such as concentration of the spins, filling

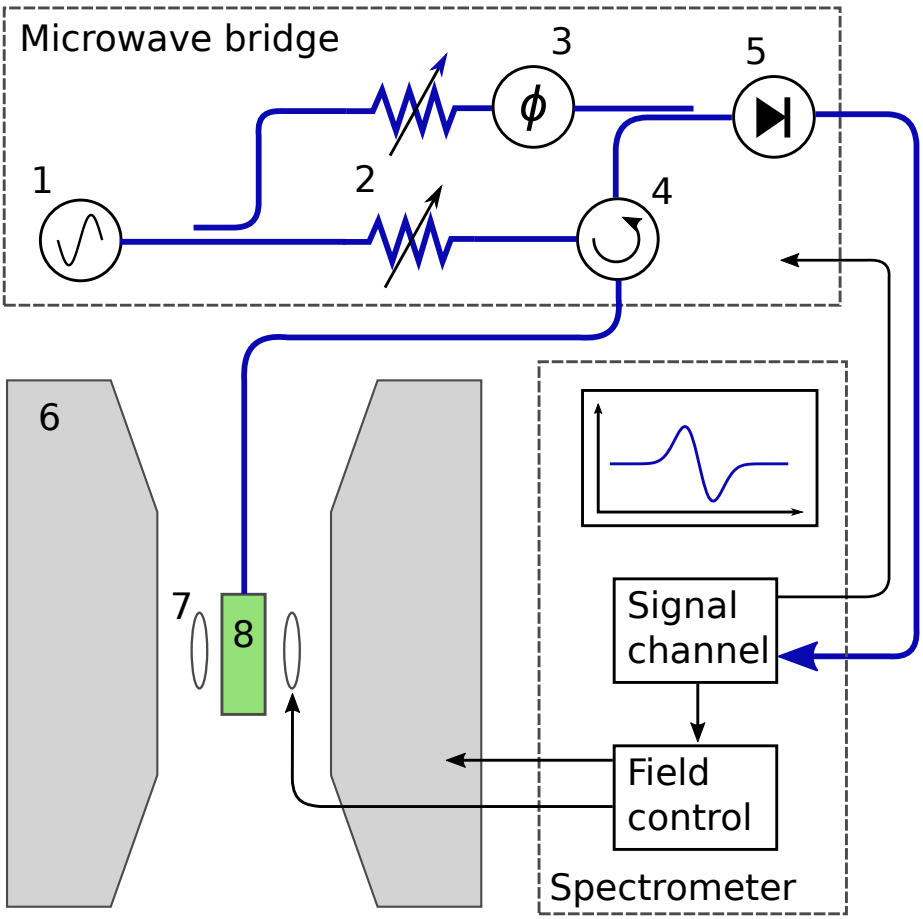

Figure 3.1: CW ESR experimental setup. 1: Microwave source, 2: Variable attenuators, 3: Phase shift, 4: Circulator, 5: Diode, 6: High-field magnet, 7: Modulation field coils, 8: ESR resonator and sample space.

factor of the sample in the resonator, microwave power and the modulation amplitude [36]. To extract quantities such as total spin number, the integrated intensity must be used. This requires a double integration of the CW derivative signal.

As discussed in Section 2.2.5, the absorption is proportional to B_1^2 and thus to the applied power (at low enough power), but the signal measured with the change in the resonator is proportional to B_1, the square root of the microwave power. Including the saturation factor, the amplitude of the ESR signal is thus

$$A \propto \frac{B_1}{1 + \gamma^2 B_1^2 T_1 T_2}. \tag{3.1}$$

3.1.2 Pulsed ESR

As described in Section 2.2.6, dynamics of spin systems can be investigated by sending short, well defined microwave pulses to flip the spins by $\pi/2$ or π on the Bloch sphere, and observing their evolution. The Bruker E680 is also capable of pulsed measurements. In this setup, the resonator is over-coupled to avoid the applied pulse ringing inside for an extended time. To be able to apply $\pi/2$ and π pulses that are on the order of tens of nanoseconds, the pulses are strongly amplified with a travelling wave tube (TWT) amplifier. Furthermore, as the signal that gets emitted by the spins as an echo is extremely weak, it needs a much more sensitive measurement than the diode used for CW experiments. The signal instead gets routed to a low noise amplifier. The amplifier would get damaged if a strong signal gets picked up, so it gets blocked automatically when the high power pulses are sent to the resonator. Furthermore, it is important to make sure there is no ,,ringdown" of the pulses, i.e.

that the pulses have escaped the resonator before the block is turned off. This is done by properly overcoupling the resonator.

For LEFE experiments, the sample is connected to a Agilent 33500B voltage pulse generator that is triggered by a pulse sent by the Bruker E680. The 33500B is limited to 20 V pulses. Higher voltage pulse generators are expensive but would allow for performing LEFE experiments on a broader range of systems, as well as potentially investigating non-linear effects.

3.2 Fabrication

One of the most challenging parts of quantum technology research is the device fabrication. In our case, this generally consists of transferring one or more metallic patterns onto a crystal substrate. There are different ways of achieving this, but we use the so-called lift-off procedure (See Figure 3.2). This consists of covering the substrate in a fluid material called resist that is sensitive to either ultraviolet light (UV) or high-energy electrons. Then we create a pattern in the resist using UV or electron beam lithography, respectively, removing part of the resist and leaving a mask in the shape of the pattern. Next, a metal is evaporated directly onto the wafer and subsequently the unwanted metal is lifted off by dissolving the resist mask in a strong solvent, leaving a metal layer on the substrate in the shape of the lithography pattern. This procedure can be repeated multiple times to create more complicated structures, and with some ingenuity, a single lift-off process can be used to create multilayer structures such as Josephson junctions for superconducting qubits [68].

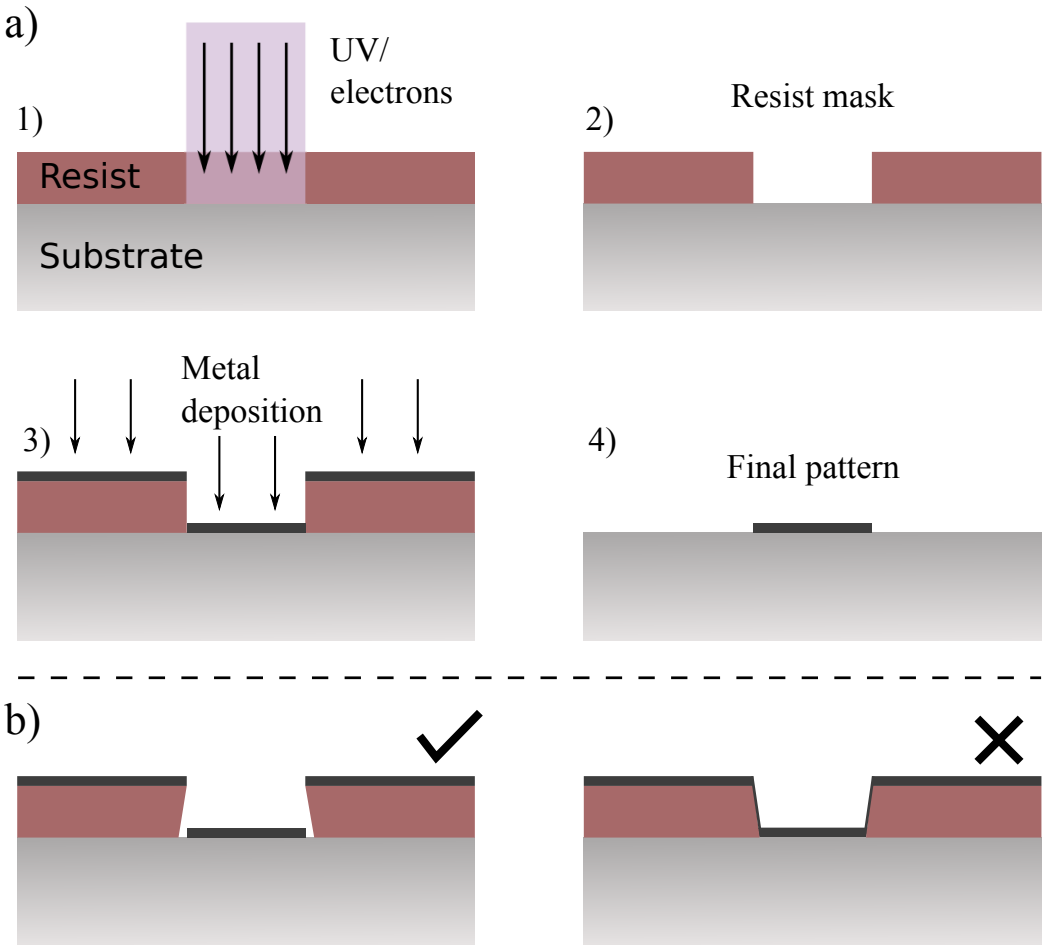

Figure 3.2: (a) Lift-off procedure. 1) A layer of resist is deposited on top of a clean wafer using a spin-coater, and a pattern is exposed using UV light or electron beam. 2) The resist is developed, leaving a mask of resist on the wafer. 3) Metal is deposited perpendicularly on top of the wafer using evaporation or other means. 4) The resist is dissolved in a solvent, lifting off the metal on top but leaving the desired metallic pattern on the substrate. (b) A slight undercut of the resist profile after exposure is preferable as it helps with lift-off.

We use both ultraviolet photolithography (UV-PL) and electron beam lithography (EBL), depending on the minimum feature size of the pattern. EBL can easily be used to create features of width down to around 100 nm, while with UV-PL we are limited by diffraction to features not much smaller than a micron. In UV-PL, we design an array of patterns that is then transferred to a metallic pattern on a glass mask (purchased from JD Photo Data [1]). The mask is placed on top of the resist-covered substrate and the whole pattern is exposed at once by flashing a UV lamp above the mask. In EBL on the other hand, no pre-fabricated mask is needed. The pattern design is loaded into the EBL machine, and is printed onto the resist in a similar fashion as an ink-jet printer, dot by dot.

The reason why we don't use EBL for all our fabrication is that making a single device with large ground planes can take hours and cost hundreds of pounds, while UV-PL can be used to make batches of up to 100 5×5 mm^2 chips in one exposure at a fraction of the cost. Therefore, when convenient, we use UV-PL to create devices with micron-sized features or larger, and also sometimes to create the ground planes and bonding pads of a device. The finer features are later created with EBL, taking only a few minutes instead of hours.

3.2.1 EBL

As explained earlier, a beam of electrons is focused into a few-nm size spot on the substrate, and then moved around with high precision to print the desired pattern in the resist. The EBL setup used is a JEOL 5500FS. The electrons are accelerated

[1] http://www.jd-photodata.co.uk/

with high voltage, ranging from a few kV up to 100 kV. The kinetic energy of the electrons is directly proportional to the acceleration voltage, and the profile of the exposed resist depends strongly on the voltage amongst other parameters. As shown in Figure 3.2(b), it is important that the cross-section resembles the left picture more than the right, i.e. that there is a slight undercut to avoid a connection between the metal on the substrate and the metal on top of the resist.

To achieve the best results and consistency, it is important to do a dose test for each new combination of substrate, resist type and thickness, and acceleration voltage. In the case of fabricating SAW resonators, the dose test consists of exposing a few resonator sections with different line widths ranging from 400 nm down to 100 nm, repeated in an array with different doses. Observing the resulting patterns is often enough to choose the right dose depending on the line width desired, but for optimal dose choice, it is best to evaporate metal and perform the lift-off procedure, and see which dose results in the best final pattern. The final procedures used in our work are detailed in Appendix A.

3.3 Dilution refrigerator microwave setup

A dilution refrigerator is necessary for experiments where aluminium is desired to be in its superconducting state, i.e. well below 1.2 K, to work at all. Secondly, to perform coherent manipulations of a quantum system it is crucial to avoid thermal excitations. The phonon frequency that corresponds to $T = 10\,\mathrm{mK}$ is $f_{\mathrm{thermal}} = k_B T/h \simeq 200\,\mathrm{MHz}$, assuring that devices of a few GHz are extremely likely to be in the ground state.

The fridge (Oxford Instruments Triton) consists of 6 stages of decreasing temperature ranging from room temperature down to 10 mK. All microwave cables (UT85) and DC wiring must be fed through the top plate (room temperature) and pass through each of the temperature stages. Figure 3.3 shows a schematic of the fridge with the microwave cabling inside. The cabling, attenuation and amplification inside the fridge are carefully designed to meet certain constraints. Firstly, the material and number of cables must be chosen to keep the heat load on each stage below the cooling power of the fridge, or it won't cool properly. Secondly, some experiments require extremely low microwave noise at the device. The thermal microwave noise generated in the cables themselves at the higher temperature stages can be enough to ruin these experiments. It is therefore important to attenuate the lines strongly in this case. The strong attenuation requires strong amplification of the extracted signal to be able to detect it.

On the left of Figure 3.3 are shown cables with a relatively low total attenuation of 9 dB, which is mostly to avoid resonances along the lines. These lines can be used when characterising resonators or in general when it is not necessary to control the number of excitations down to single digits. On the right, the attenuated input and amplified output lines are shown. The attenuation is spread out and thermally anchored at three different temperature stages. For one-port resonator experiments, it is necessary to use circulators to redirect the reflected signal to the output line. Two circulators (Raditek Cryo with magnetic shields) are used to avoid any reflection from the amplifier going back to the device. The input allows for a continuous microwave signal (RF1, Rohde & Schwarz SMF100A) to be sent in, as well as a pulsed microwave

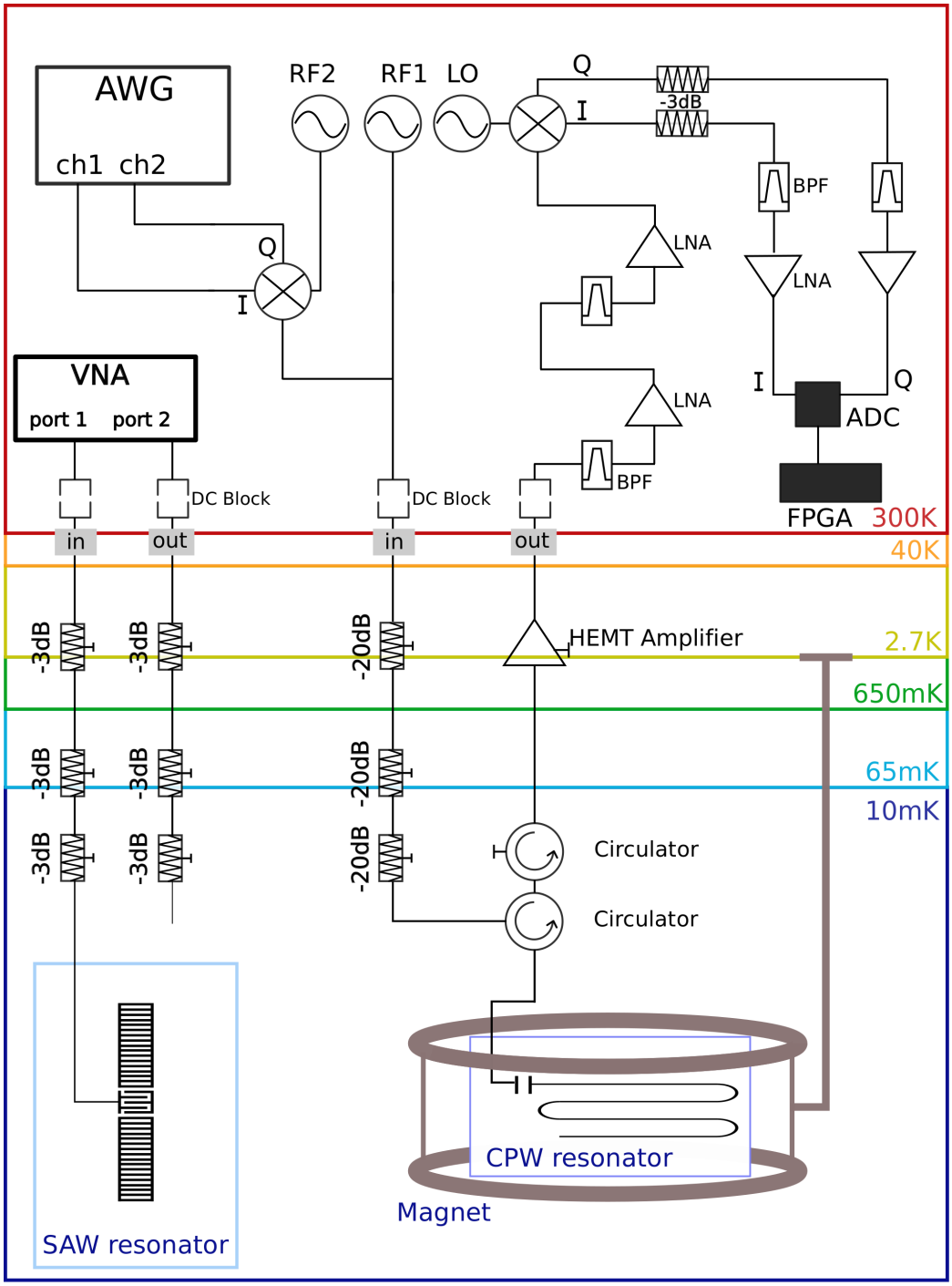

Figure 3.3: Schematic of dilution fridge measurement setup. Devices can either be measured on low attenuation lines with a vector network analyser (VNA) or on highly attenuated lines for low noise measurements. The FPGA measurement setup is described in detail in the main text.

signal, achieved by mixing a continuous one (RF2, Rohde & Schwarz SMF100A) with a DC pulse from the arbitrary waveform generator (AWG, Textronix 5014C) using an IQ mixer (Marki-Microwave IQ-4509). The output line is amplified with a high-electron-mobility transistor (HEMT) amplifier (Low Noise Factory LNF-LNC1-12A) anchored at the 2.7 K stage. This amplifier is ultra low noise and amplifies the signal by 39 dB. After the signal has left the fridge, there is a further stage of amplification to bring the signal level to an optimal range. The low-noise amplifiers (LNA, Mini-Circuits ZVA-183+) amplify the signal by another 26 dB, before it gets down-converted to 62.5 MHz with an IQ mixer (Marki-Microwave IQ-0618). After this, there is a final set of 24 dB LNAs (Mini-Circuits ZFL-500LN+) before the signal gets picked up by an analog-digital converter (ADC, 4DSP FMC104) connected to a field-programmable gate array (FPGA, Xilinx Virtex-6 FPGA with ML605 board) board, which is designed to be able to rapidly read the digitised signal and average it in hardware.

3.4 Superconducting magnet with rotating sample

To perform spin-coupling experiments in our dilution fridge, we decided to build a superconducting magnet ourselves. Buying commercially made magnets can be very expensive, and the physical design is not very complicated. As our department has a competent cryomagnetics group, the technical aspects of this task were relatively straightforward. We opted for a simple split-coil design with a single fixed axis, since the task would be much more complicated if we were to build a three-axis vector

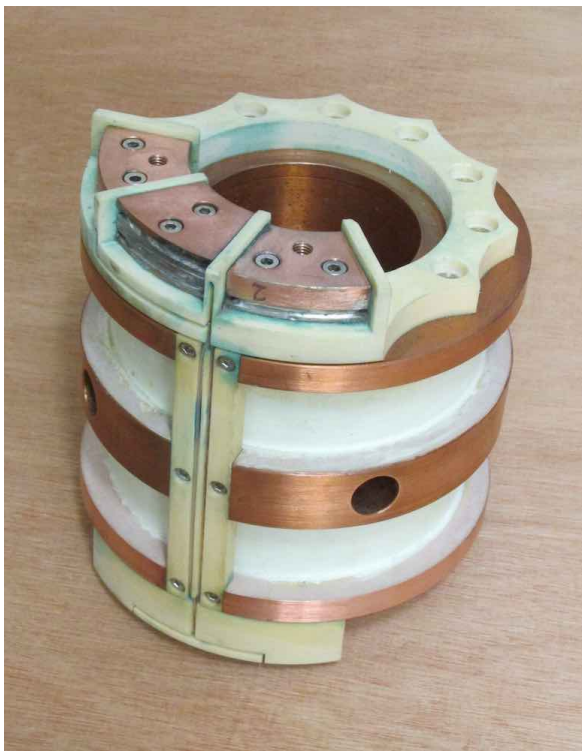

Figure 3.4: In-house built superconducting magnet.

magnet to control the field direction.

Our magnet consists of a copper spool, or former, onto which superconducting wire is wound (see Figure 3.4, wires covered with white resin). The wire must of course be wound such that the current is going in the same direction around the spool in both coils, such that the magnetic fields point in the same direction. The wires are terminated in large copper blocks, and the superconducting leads in the fridge terminate in identical blocks that screw on tightly to minimise contact resistance. The constraints we worked with when designing the magnet dimensions were firstly the total wire length, of which we had about 3000 metres, a minimum inner diameter and a minimum distance between the coils to allow for optical sample access for greater flexibility. The magnet bolts onto the 4 K shield of the fridge and must fit around the

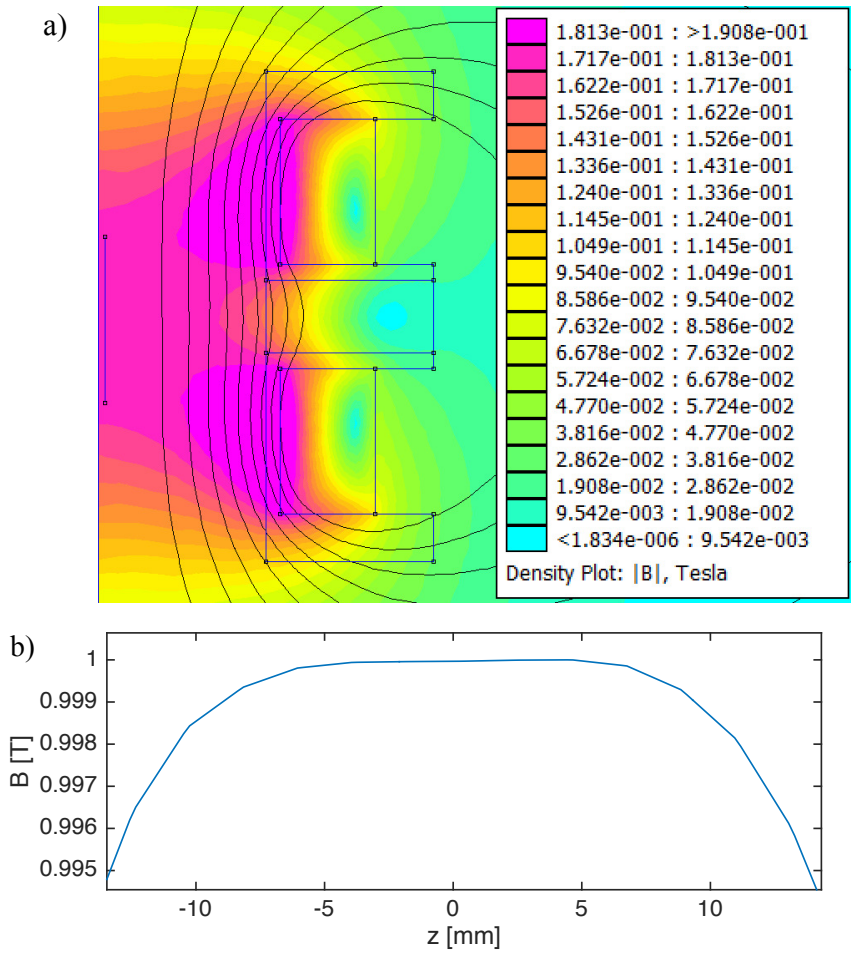

Figure 3.5: a) Simulation of the magnet field using the FEMM software. b) The line plot shows the uniformity of the field along the line shown on the left of the image in a) (magnet axis).

tail of the still shield into which the sample is placed. Using first simple magnetic coil equations and then full simulations in FEMM [2], a design was settled upon that yields approximately 1 T at a current of 10 A and has a well-optimised field uniformity in the centre.

The magnetic field strength was initially calibrated by using a magnetic sample from Alexy Karenowska's group, consisting of a YIG (yttrium-iron-garnet) sphere located close to an antenna. The YIG sphere has a magnetic mode with a well known g

[2] http://www.femm.info/

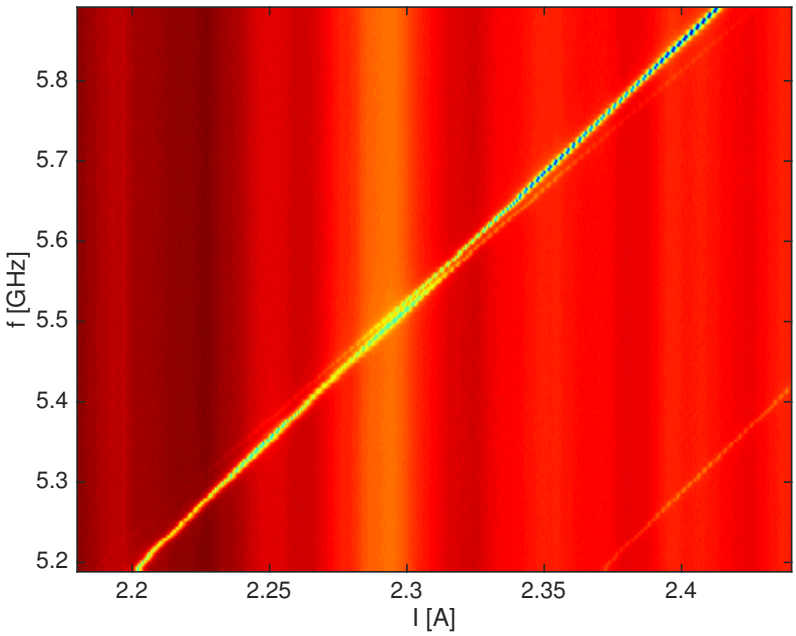

Figure 3.6: Measurement of a YIG sphere near an antenna as a function of current applied to the magnet.

factor, and by tracing the resonance frequency as a function of applied current to the magnet (see Figure 3.6), the relation between current and field was found to be $79.31 \pm 0.01\,\mathrm{mT/A}$, assuming that the YIG has $g = 2$.

3.4.1 Rotator

It is often important either to be able to align the magnetic field carefully in the plane of a superconducting device, or to record magnetic field dependence at various angles of the field to the sample. This is easy with a vector magnet where the field can be pointed in any direction, but with a fixed field axis this means that the sample needs to be rotated. Rotating stages that are designed to work at sub-Kelvin temperatures are not common, but one such is the piezo-controlled rotating stage (Attocube ANRv220 used in our case). The motion is achieved by piezoelectric crystals to which a sawtooth

voltage is applied. On the slope, the piezo contracts/expands slowly and brings the stage with it, and on the sharp voltage decline the piezo moves so quickly that it slips beneath the stage, resulting in a net movement. The speed of motion is controlled by setting the voltage amplitude and the repetition frequency. One problem that is very difficult to solve is that mechanical motion will sharply increase the temperature of the base plate which usually is at 10 mK. The only thing one can do is to rotate slowly and wait on the order of ten minutes for the temperature to settle after rotation.

A bigger problem with rotating a sample is the connection of microwave signals. Typically, rigid microwave cables and microwave connectors that snap (MMPX) or screw (SMA) onto the sample holder are used. Even highly flexible thin coaxial cables cannot be guaranteed to bend nicely near zero temperature. One option is to print coplanar waveguides onto a flexible Kapton ribbon that is known to work nicely at low temperature [69]. Another way is to design the sample holder in such a way that the axis of the board connector coincides with the axis of rotation, and slightly file down the cable connector so that it can rotate relatively freely in the board connector. This is what we opted for, and the final setup can be seen in Figure 3.7.

3.5 Sample holder and PCB design

In any experiment involving a fabricated microwave circuit, we need a suitable sample holder to place the device. The sample holder fulfils multiple purposes. Firstly, the microwave signal needs to be transmitted from the fridge cables to the device somehow, and this is usually done by designing a printed circuit-board (PCB) around the sample device, with microwave connectors for the cable to connect to. From the

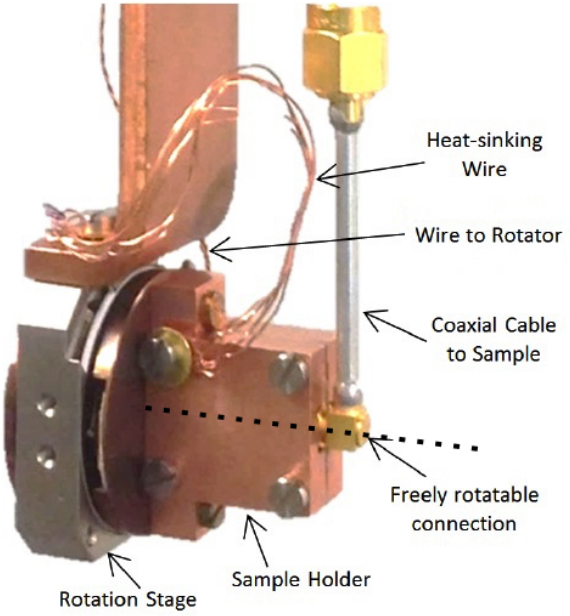

Figure 3.7: Sample holder mounted on a rotating piezo-stage with a freely rotating MMPX cable attached. Dotted line shows axis of rotation.

connectors, coplanar waveguides are printed on the board and lead to the edge of the sample, where a wire bonder is used to create an electric connection between the PCB and the sample. Secondly, the sample holder protects the device from the environment. Thirdly, it provides a good way of thermalising the sample by clamping on to the cold stage or a copper extension of it.

The sample holder to use with the rotator is shown in Figure 3.8. As shown in Figure 3.7, it screws directly onto the face of the rotator, with the rotational axis passing straight through the sample and coinciding with the axis of the MMPX connector. The design also includes DC connections for the possibility of applying static voltages or currents to the device, such as a gate voltage.

For experiments in the helium cryostat, we made the sample holder shown in Figure 3.9. We need to provide a small modulation magnetic field to perform lock-in

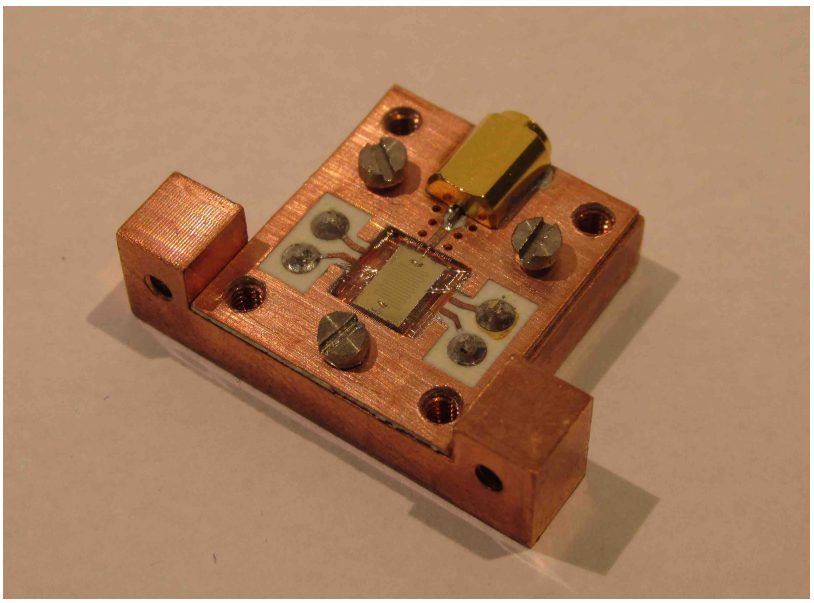

Figure 3.8: Sample holder designed for use with the rotator. Sample space fits 5×5 mm^2 chip. Pictured with a CPW resonator mounted. DC connectors were included in the design but ultimately not used.

measurements in CW-ESR type experiments. For this purpose, we created a plastic version of the sample holder lid, since the rapidly oscillating magnetic field would not penetrate the thick copper lid. We created a small modulation coil to screw onto the plastic lid.

3.6 Testing magnet-rotator setup with a CPW resonator

As a first experiment to try out our new magnet-rotator setup, we decided to fabricate aluminium coplanar waveguide resonators on ZnO and other substrates, and measure their performance in magnetic field with angle dependence. This would also allow us to estimate the feasibility of observing coupling between the CPW mode and the spin impurities in the substrate. Use of CPW resonators for spin physics experiments requires a high quality factor to be maintained in the required magnetic field. This

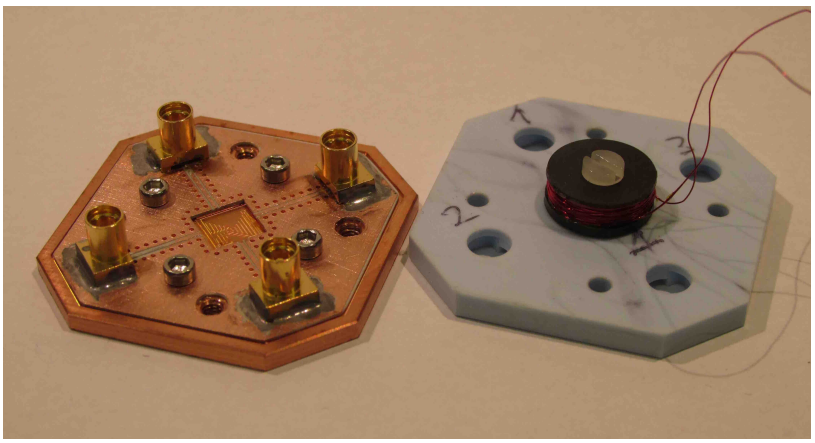

Figure 3.9: Sample holder designed for multiple devices on one 5×5 mm^2 chip. The lid is made from machinable plastic to allow the modulation field to penetrate. Modulation coil screws on to the lid.

usually means using more exotic superconductors than aluminium, such as Nb or NbTi, which is not always a readily available in-house technique. Aluminium is a superconductor that our group has extensive experience in making devices with using lift-off techniques. It has a fairly low bulk critical magnetic field at about $B_{cb} = 10.5$ mT. However, thin film superconductors benefit from modified in-plane and perpendicular critical fields [70]

$$B_{c\parallel} = \frac{2\sqrt{6}B_{cb}\lambda}{d} \tag{3.2}$$

$$B_{c\perp} = \frac{8\pi e}{h}(B_{cb}\lambda)^2\frac{1-t^2}{1+t^2} \tag{3.3}$$

where λ is the penetration depth of the superconductor, d is the thickness of the film and $t = T/T_c$. The critical field when it makes an angle θ with the superconductor plane is found with the equation [70]

$$\frac{B_c \sin\theta}{B_{c\perp}} + \left(\frac{B_c \cos\theta}{B_{c\parallel}}\right) = 1 \tag{3.4}$$

meaning that close to $\theta = 0$, $B_c \simeq B_{c\parallel}$. Inspired by this we decided to investigate how high a field we could reach with a coplanar waveguide resonator made from aluminium

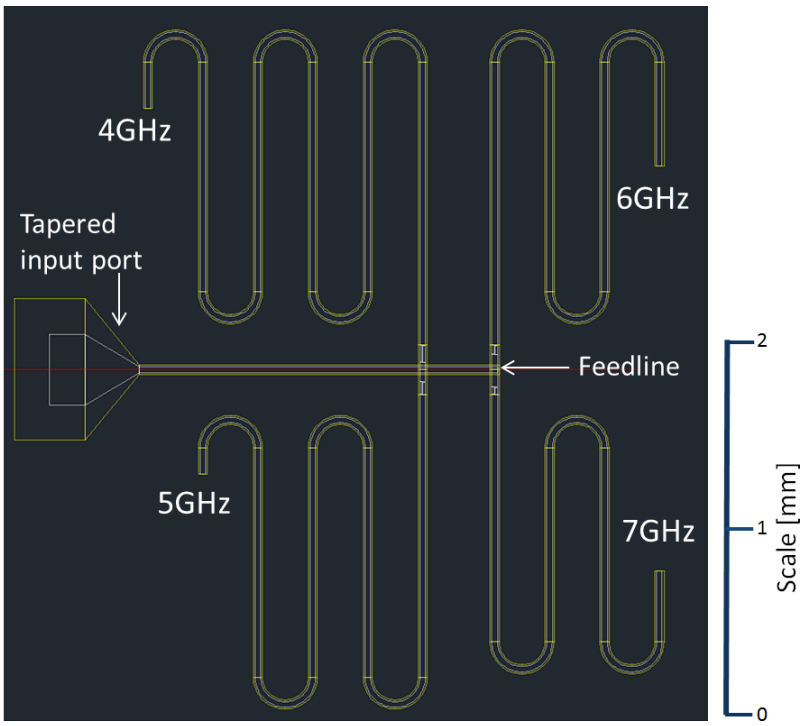

Figure 3.10: Multiplexed CPW resonator design.

without destroying the resonance.

We fabricated CPW resonators using photolithography, starting with ZnO as a substrate. The design we used is shown in Figure 3.10. It is a one-port multi-resonator design, measured in reflection mode. Computer simulations of the design with the finite element software HFSS [3] showed that all resonators should couple to the feedline. What we found with the resonator on ZnO was that the resonance was extremely broad, with $Q \sim 100$. We suspect that this means the coplanar waveguide mode has high acoustic loss on such a strongly piezoelectric substrate.

We subsequently fabricated CPW resonators using an aluminium film of thickness $d = 20\,\mathrm{nm}$ on a sapphire substrate instead. This proved to be much better, allowing us to measure quality factors of up to about $Q_i \approx 80000$. Strangely, we never saw

[3] http://www.ansys.com/products/electronics/ansys-hfss

more than one resonance, whereas we were expecting to see four. This could be due to imperfect fabrication procedures, or there might be a flaw in our design.

We then used this resonance to test our magnet and rotator setup. With the field approximately in-plane with the resonator, we swept the field to positive and negative values and recorded the complex trace of the resonance at each point. Figure 3.11 shows the internal quality factor and frequency, fitted with Equation (2.103) as a function of applied field. The first observation is that the frequency shift is symmetric around $B \approx -0.5$ mT, possibly offsetting an ambient magnetic field in the lab. Second, the frequency shift is well fitted with a square dependence on field, for low field strength. The reason for this is a change in the kinetic inductance, and the equation describing this dependence is [71]

$$f_0(B) = f_0(0)\left(1 - \frac{L_K(0)\chi(T)}{L_T}\frac{B^2}{B_c^2}\right) \tag{3.5}$$

where L_T is the total inductance, $L_K(0)$ is the kinetic inductance at zero field and $\chi(T)$ is a temperature dependent scaling factor. Fitting this equation to the field dependence of the measured resonator frequency gives us γB_c, where $\gamma = \sqrt{L_T/(L_K(0)\chi(T)}$.

Since we have the sample mounted on a rotating stage, we can vary the angle that the static magnetic field makes with the plane of the film. By varying the angle and measuring γB_c at each angle (plotted in Figure 3.12), we could fit Equations (3.2)-(3.4) to extract the values $\gamma = 0.9 \pm 0.1$ and $\lambda = 76 \pm 7$ nm. This gives us $B_{c\parallel} \approx 200$ mT. Note that as Figure 3.12 reveals, we did not have a readout of the actual angle of the rotator and could only go by the number of steps taken with the controller, which we roughly correlated with angle at room temperature. It is possible

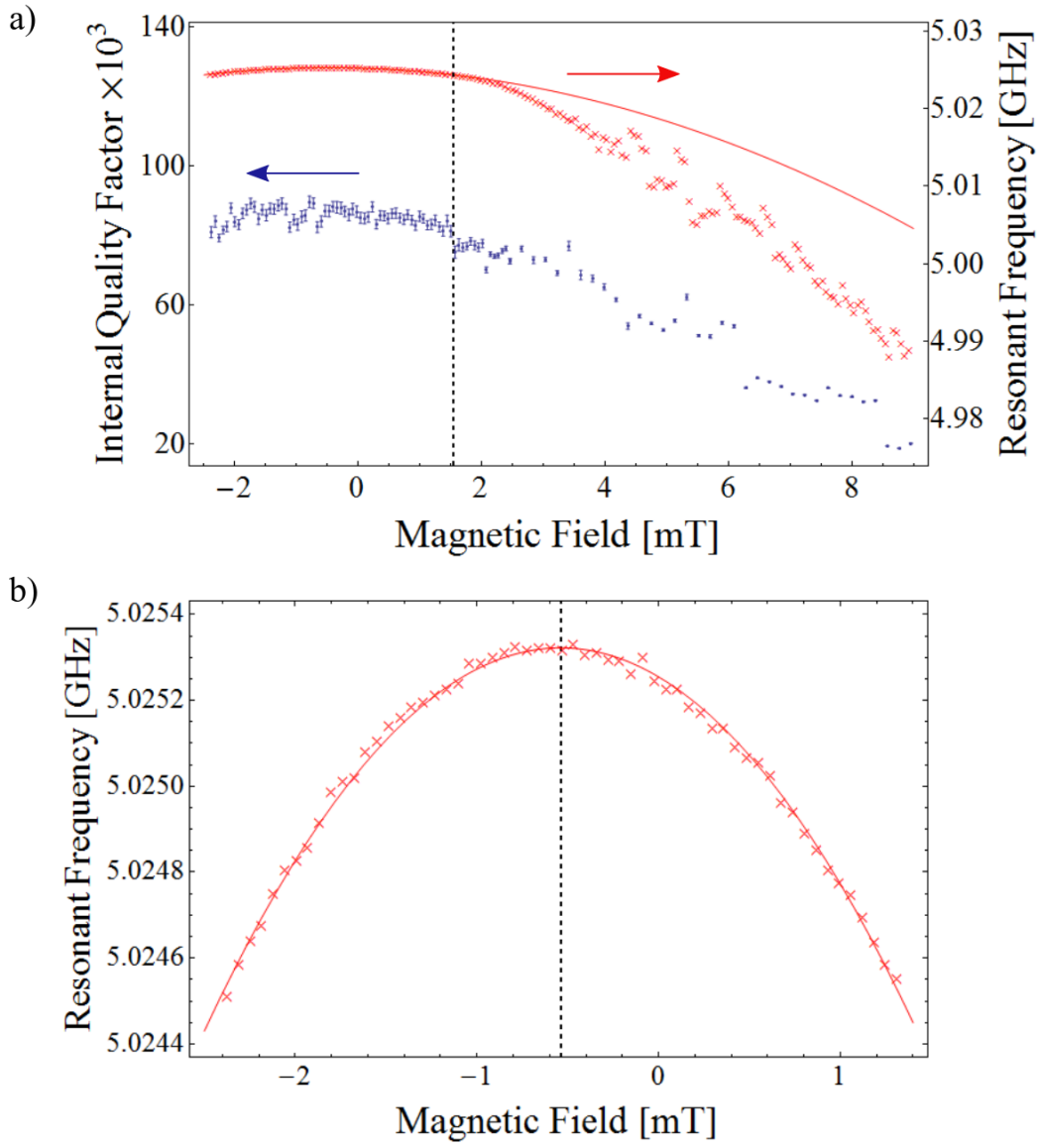

Figure 3.11: Response of a CPW resonator on sapphire in magnetic field. a): Q_i and f as a function of applied magnetic field. Crosses are f, dots are Q_i. b) Expanded view of f only, showing the quadratic dependence on applied field [1].

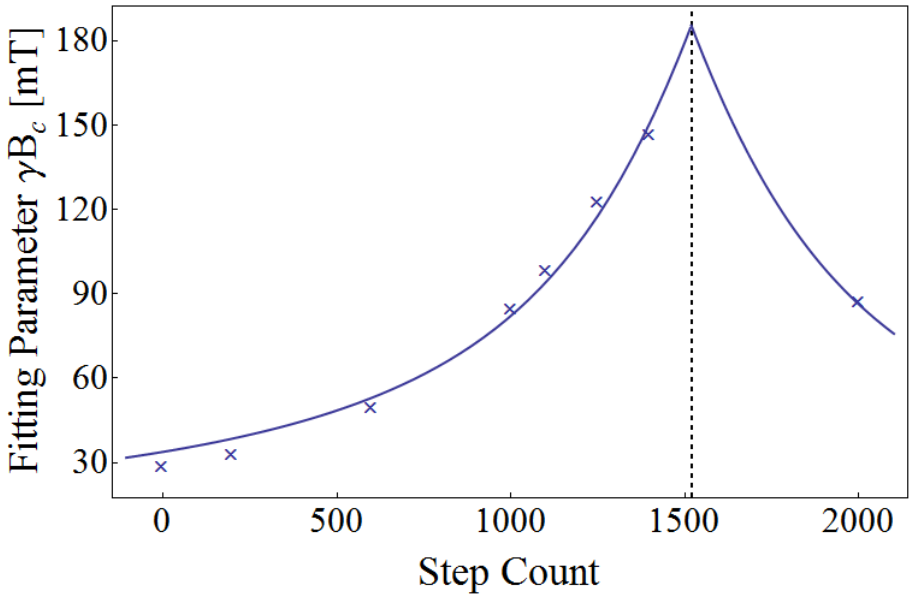

Figure 3.12: Dependence of the parameter γB_c on angle (rotator step count). [1].

to implement a reliable angle readout as the rotator has an internal sliding resistor, but this requires developing a pulsed resistance measurement at low temperature, which is non-trivial.

The reasonably high $B_{c\parallel}$ is promising for the use of aluminium CPW resonators for spin experiments. However, even with the field nearly in-plane, the resonance was completely gone at $B \approx 50$ mT. This is most likely due to generation of vortices where superconductivity is suppressed [72]. It is thus clear that with our current setup it would be hard to do magnetic field-dependent spin coupling experiments unless the resonator frequency is very close to a spin resonance at zero field. This is possible for spin systems with a large zero-field splitting.

3.7 Spin resonance experiments in cryostat

To set up an experiment in the dilution fridge can take on the order of a week longer than just inserting the sample in a cryostat, due to all the aspects of the fridge cycle such as cool-down time, as well as the need to schedule measurements within the group. Measuring in a cryostat is relatively quick and easy, given the availability of liquid helium. The sample is mounted on the end of a probe which is inserted into the cryostat, and after about an hour of temperature stabilisation to the required temperature ranging from liquid helium temperature up to about 200 K, measurements can begin.

The cryostat available to us is an Oxford Instruments helium cryostat with a 6 T superconducting split coil magnet installed. The main drawback of using the cryostat compared to the dilution fridge, apart from the temperature constraint, is that the measurement equipment needs to be assembled according to needs each time. It is not trivial to set up pulsed measurements, while the highly advanced FPGA assembly by the dilution fridge allows for nearly arbitrary pulsed measurements to be set up.

Performing a CW-ESR type experiment with a SAW or CPW resonator is fairly straightforward, and the schematic for the setup is shown in Figure 3.13. The concept is practically identical to traditional CW-ESR, although instead of using a diode to read the RF power, an IQ mixer is used to down-convert to a DC signal which is then measured by the lock-in amplifiers (SRS SR830). Also, a SAW or CPW resonator does not have tuneable coupling, and can thus not be critically coupled, losing a lot

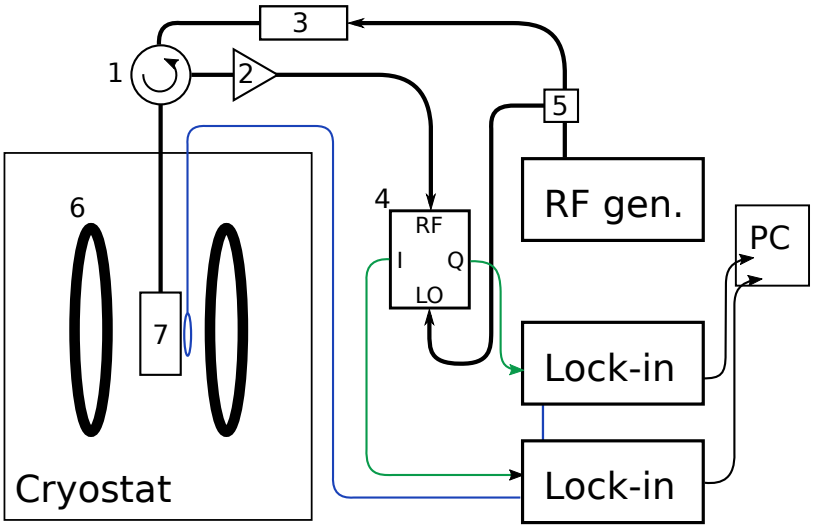

Figure 3.13: Setup for spin resonance experiments. 1: Circulator, 2: Amplifier, 3: Attenuator, 4: IQ mixer, 5: Splitter, 6: Magnet, 7: Sample holder and modulation coil.

of sensitivity. The same setup can be used to measure the frequency response of the resonator itself by turning off the modulation and connecting the I and Q ports of the mixer to voltmeters instead of the lock-in amplifiers.

3.7.1 IQ mixer and lock-in amplifier measurement

The RF generator is set to the resonant frequency of the resonator, ω_r. The signal is split at the source, with half going straight to the LO port of the IQ mixer and one getting attenuated before entering the resonator, amplified on the output of the circulator, and then fed to the RF port of the mixer. The signal arriving at the RF port is

$$S(t) = A\cos(\omega_r t + \phi) \tag{3.6}$$

where ϕ_r is the phase relative to the LO. The IQ mixer then mixes the two signals together, and outputs

$$I = A_{\mathrm{LO}} A \cos(\phi) + I_0 \tag{3.7}$$

$$Q = A_{\mathrm{LO}} A \sin(\phi) + Q_0 \tag{3.8}$$

where constant offsets I_0 and Q_0 are artifacts of the mixer. As the magnetic field is swept, both A and ϕ can change when the spins are in resonance with ω_r. The lock-in amplifier provides a modulation signal to the small magnetic coil on the sample, of frequency ω_m. The signals thus become time dependent again:

$$I(t) = A_{\mathrm{LO}}(A_0 + A' \cos(\omega_m t + \phi_m)) \cos(\phi_0 + \phi' \cos(\omega_m t + \phi_m)) + I_0 \tag{3.9}$$

$$Q(t) = A_{\mathrm{LO}}(A_0 + A' \cos(\omega_m t + \phi_m)) \sin(\phi_0 + \phi' \cos(\omega_m t + \phi_m)) + Q_0 \tag{3.10}$$

where ϕ_m is a modulation phase delay caused by the inductance of the modulation coil. These signals are each fed into a lock-in amplifier. In the amplifier, the signal gets digitised, and processed by integration into two channels, X and Y, defined as:

$$X = \frac{1}{T} \int_0^T \cos(\omega_m t) I(t) \mathrm{d}t \tag{3.11}$$

$$Y = \frac{1}{T} \int_0^T \sin(\omega_m t) I(t) \mathrm{d}t \tag{3.12}$$

or with $Q(t)$ instead of $I(t)$, depending on which is being measured. This integration picks out the part of the signal that oscillates with frequency ω_m, or in mathematical terms returns the Fourier coefficient for that frequency. The longer the time constant T chosen, the less noisy the output is, but it must be short enough not to distort the shape of the signal. The reason for having two channels X and Y is that this way,

one retrieves the full signal, whatever the modulation phase delay ϕ_m happens to be. The X amplitude gets maximised when ϕ_m is close to 0° or 180°, and Y is maximised 90° out of phase. The full signal can be mapped to either X or Y by rotating the signal in $X - Y$ space:

$$(X_I, Y_I) \longrightarrow (X_I \cos(\theta) - Y_I \sin(\theta), X_I \sin(\theta) + Y_I \cos(\theta)) \tag{3.13}$$
$$(X_Q, Y_Q) \longrightarrow (X_Q \cos(\theta) - Y_Q \sin(\theta), X_Q \sin(\theta) + Y_Q \cos(\theta)).$$

The total signal in each of the channels X_I, Y_I, X_Q, Y_Q is calculated by first correcting for any linear background and then calculating the sum of squares for each sweep,

$$X_I^{\mathrm{SSQ}} = \sum_i X_I^2(B_i) \tag{3.14}$$

and similarly for the other channels to get $Y_I^{\mathrm{SSQ}}, X_Q^{\mathrm{SSQ}}, Y_Q^{\mathrm{SSQ}}$. The total signal in the X and Y channels are defined as

$$X^{\mathrm{SSQ}} = X_I^{\mathrm{SSQ}} + X_Q^{\mathrm{SSQ}} \tag{3.15}$$

and similarly for Y. The angle θ in Equation (3.13) is then varied until X^{SSQ} is maximised and Y^{SSQ} minimised, at which point most of the signal should be in the X channels. When this has been done, it should be possible to vary the angle in $I - Q$ space in a similar way until the amplitude change and phase shift are separated into each channel.

Chapter 4

Electron spin resonance of high-spin impurities in piezoelectric crystals

Electron spin resonance (ESR) experiments on Mn^{2+} in ZnO have shown that there is a linear dependence of the zero-field splitting D on electric field applied along the anisotropy axis of 20.8 ± 0.2 (rad/s)/(V/m) [38]. This provides motivation for experiments coupling surface acoustic waves to Mn^{2+}:ZnO. In ESR experiments on further samples of ZnO, we were able to observe both the previously reported Mn^{2+} spins as well as clear signals from an additional impurity, which we were able to identify as Fe^{3+}. Having a larger zero-field splitting, the new impurity was a promising candidate for spin-lattice coupling experiments. We performed analysis of the ESR spectrum to determine Hamiltonian parameters, did relaxation measurements to determine T_1 and T_2, and finally measured the linear electric field effect (LEFE).

Following a lead from the only paper showing attempts of coupling SAWs to spin ensembles [47], we also investigated iron doped lithium niobate, working with a wafer doped with 0.05% iron and performed basic ESR investigations.

Most of the ESR experiments were performed on a Bruker E680 pulsed spectrometer, in either X-band or W-band mode. A schematic of the setup for CW experiments is shown in Figure 3.1.

4.1 Fe^{3+} in ZnO

The ZnO samples used in the Mn^{2+} experiments were sold as undoped, but these nominally pure systems usually contain unintentional impurities. The unintended content can vary widely between different samples obtained, and one of the samples investigated showed strong resonances separate from those due to the known Mn^{2+} ions. As explained in the following section, this was determined to be Fe^{3+} ions.

4.1.1 Hamiltonian determination

Continuous wave experiments were done with an MD5 X-band loop-gap resonator in the Bruker E680 spectrometer. Angle dependence of the spectrum was recorded using a goniometer. As Figure 4.1(a) shows, the resonances are strongly angle dependent. Due to the hyperfine splitting of the Mn^{2+} ion as well as the forbidden transitions showing up at oblique angles, the spectrum is quite crowded in the range 3000-4000 G. Although it is technically possible to pick out individual resonances and track them through the rotations in small steps, we can also exploit the fact that the different impurities have different relaxation times to saturate them selectively. Luckily, Mn^{2+}, which has already been studied extensively in our group, has longer relaxation times than Fe^{3+} in zinc oxide, so we can saturate the Mn^{2+} to get a clearer look at the iron. Figure 4.1(b) shows the angular dependence of the CW spectrum at high microwave

power. It is clear that the Mn^{2+} impurities are mostly saturated, and what is left is the spectrum of Fe^{3+}. The resonance at around 1750 G is due to impurities in the dielectric of the resonator, and is thus of course not dependent on the angle of the sample. There is a clear splitting of all the Fe^{3+} resonances at oblique angles due to the two non-equivalent sites in the ZnO lattice.

The CW spectrum was measured at $\theta = 0°$ at various temperatures. Using Equations (2.54), the parameters g, D and $a - F$ were extracted. The latter two are plotted in Fig. 4.2. The room temperature values extracted are $D = -1785$ MHz and $a - F = 108$ MHz. This compares well to the values extracted in [40], $D = -1781 \pm 3$ MHz and $a - F = 100 \pm 30$ MHz.

A linear fit to the temperature dependence of D (filled circles) gives a shift of -0.203 ± 0.022 MHz/K. Note that D is negative, meaning that the absolute value of D increases with temperature. The errors in the data are too big to be able to infer any temperature dependence of $a - F$. This temperature dependence of D was not reported in the original study of the system [40].

4.1.2 Relaxation measurements

To perform the LEFE measurements we must switch to pulsed ESR. To effectively measure the LEFE effect, we first gathered some knowledge about the relaxation dynamics of the spin system. The relaxation times T_1 and T_m were measured for various temperatures both at X band (9.7 GHz) and W band (94 GHz). The results from X band are shown in Figure 4.3, and results from W band in Figure 4.4.

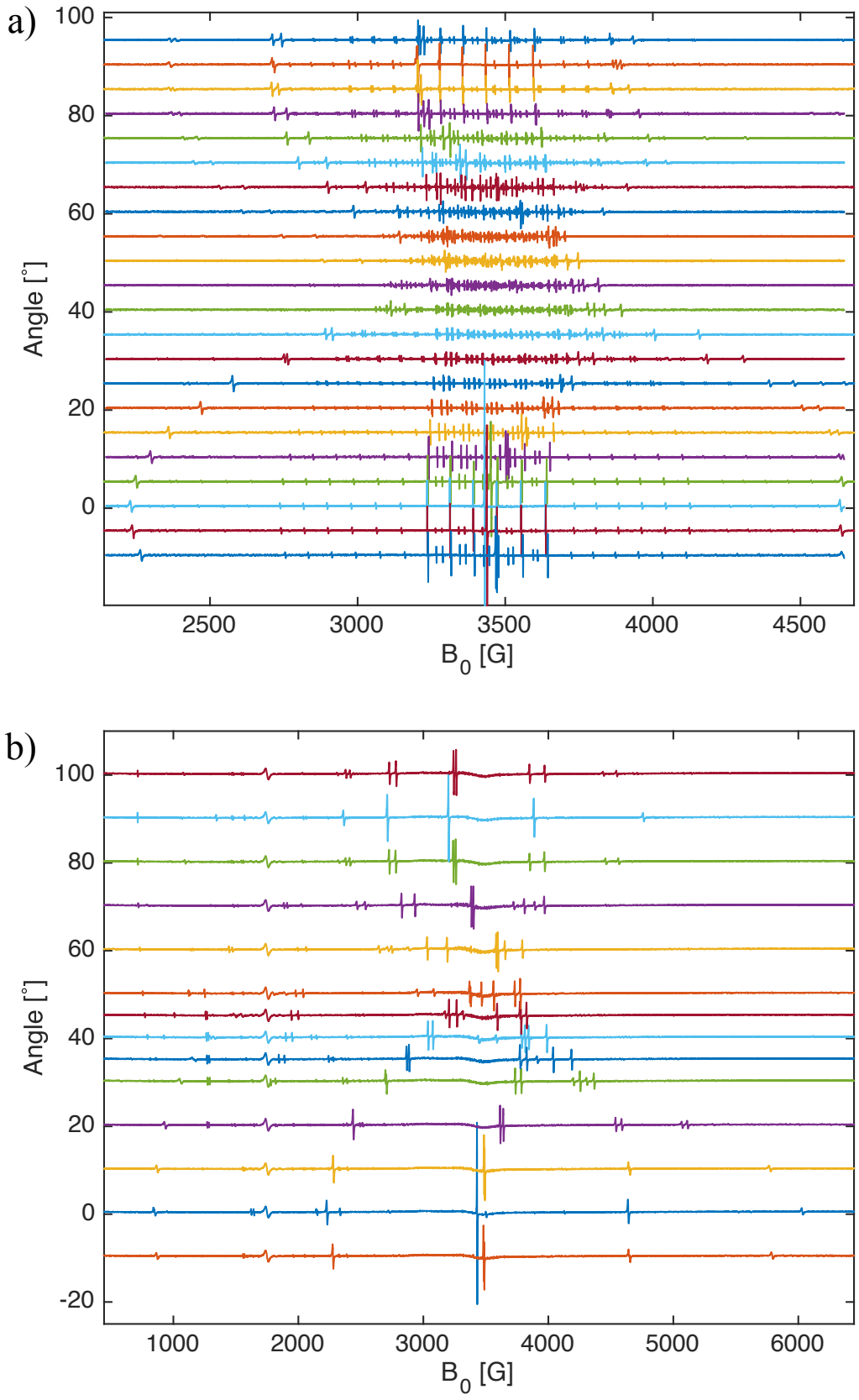

Figure 4.1: CW spectrum of ZnO sample with Mn and Fe impurities. a) low power, b) high power.

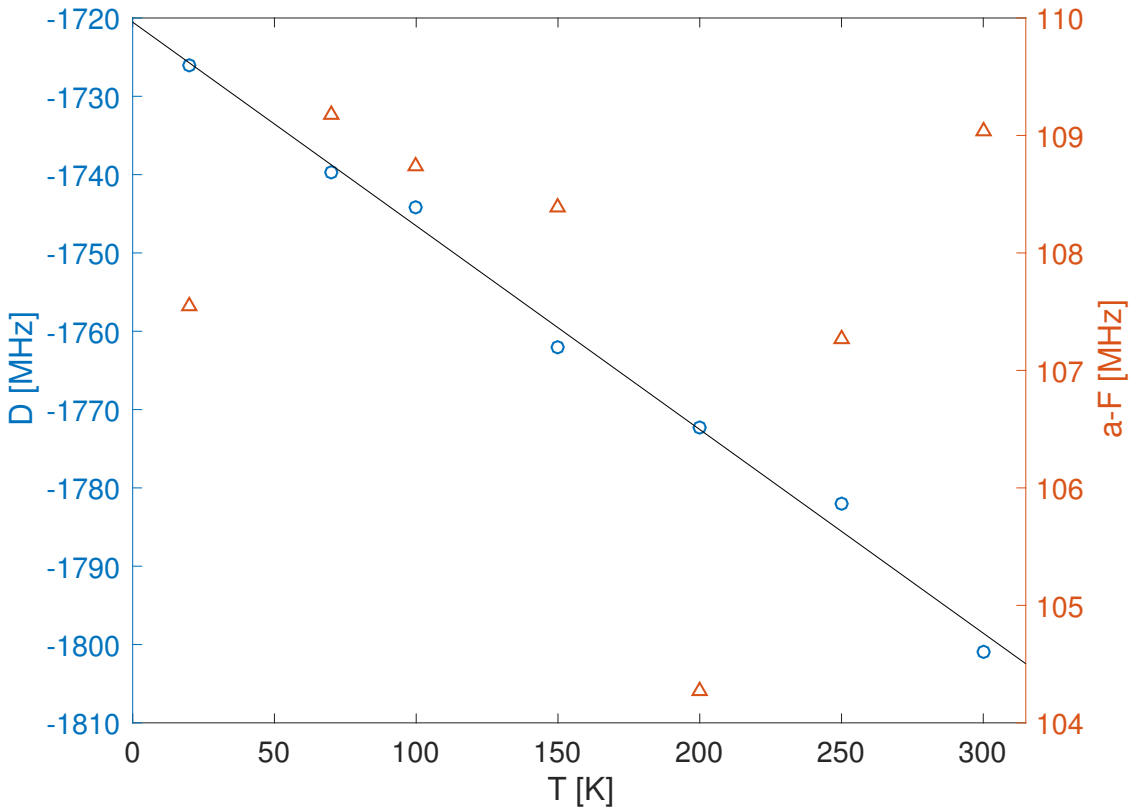

Figure 4.2: Temperature dependence of D (circles) and $a - F$ (triangles), Fe^{3+}:ZnO Hamiltonian parameters extracted from CW spectra. The line is a linear fit to the D values.

One clear feature is that the coherence time T_m is noticeably field dependent at low temperature. The inset in Figure 4.3 shows that the T_m measured at 5 K are ordered such that higher fields yield shorter T_m. At W band, the high versus low temperature behaviour of T_m is even more clear, although the low temperature field dependence is not completely monotonic. At high temperature, the $|-1/2\rangle \leftrightarrow |+1/2\rangle$ has the longest T_m, followed by $|\pm 1/2\rangle \leftrightarrow |\pm 3/2\rangle$, and the shortest one belongs to $|\pm 3/2\rangle \leftrightarrow |\pm 5/2\rangle$. This is easily understood as incoherent thermal D strain, which affects the transitions involving high $|m_s|$ more. Figure 4.5 shows that both T_1 and T_m converge for X and W band at high temperature, but deviate in favour of X band at low temperature.

As the T_2 of ZnO:Fe^{3+} at low temperature was investigated quite thoroughly in [41], we did not spend much effort pursuing relaxation measurements beyond what has been described here, such as determining contributions of different diffusion processes.

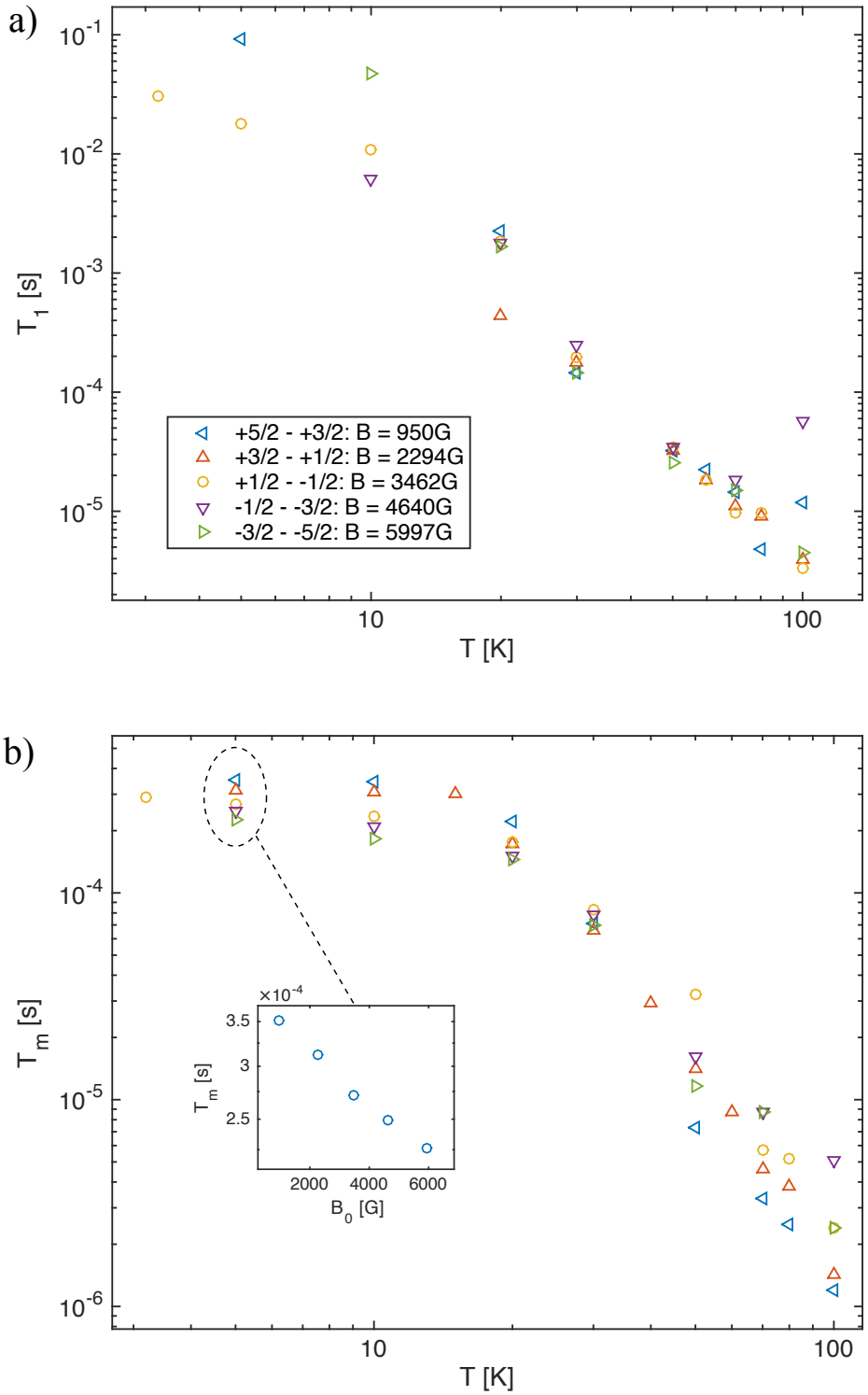

Figure 4.3: Relaxation time T_1 (upper) and T_m (lower) of Fe:ZnO resonances as a function of temperature, taken at 9.7 GHz (X band). The inset in the lower plot shows T_m as a monotonically decreasing function of magnetic field at low temperature.

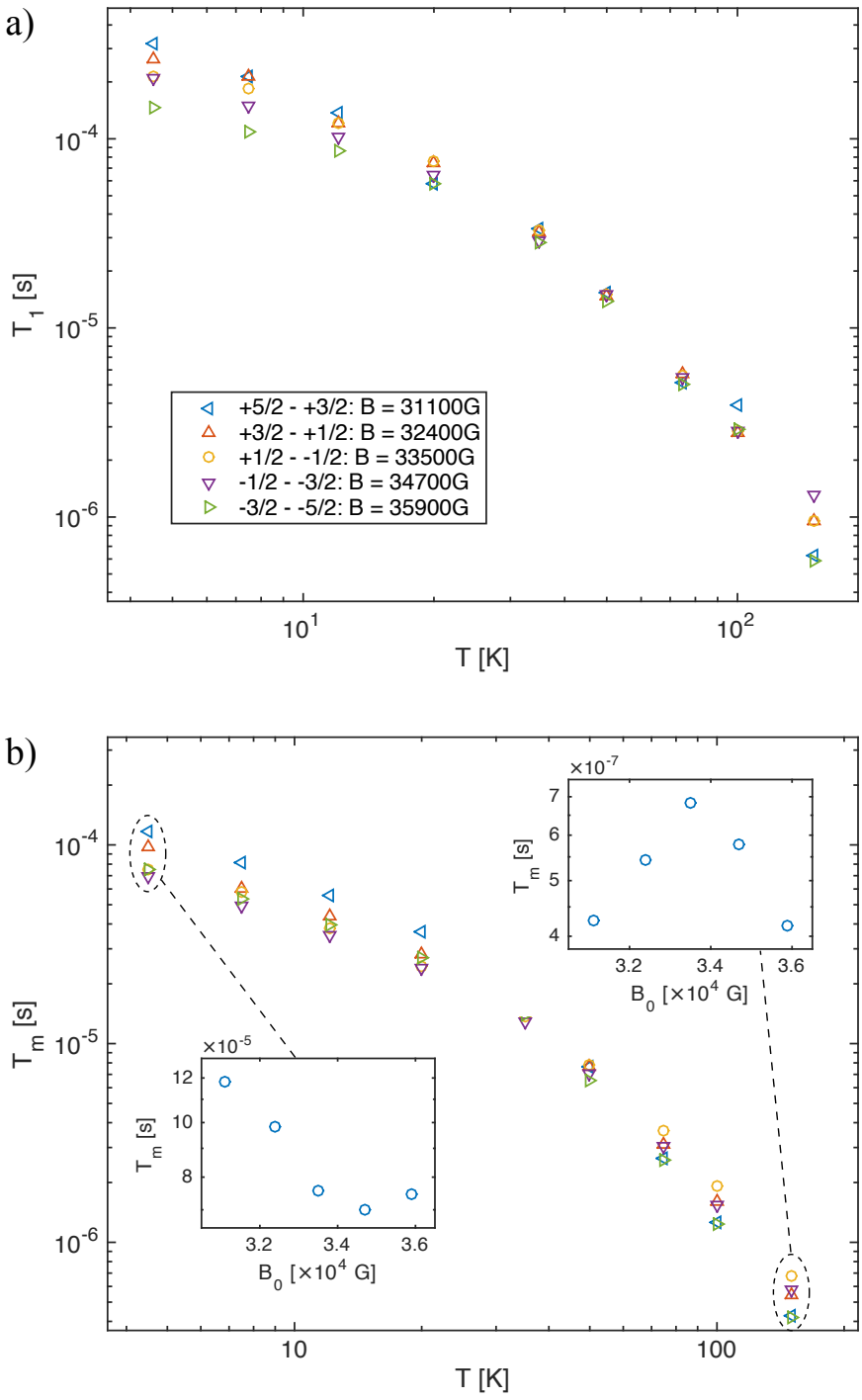

Figure 4.4: Relaxation time T_1 (upper) and T_m (lower) of Fe:ZnO resonances as a function of temperature, taken at 94 GHz (W band). The insets show the difference between high temperature and low temperature ordering of T_m as a function of magnetic field.

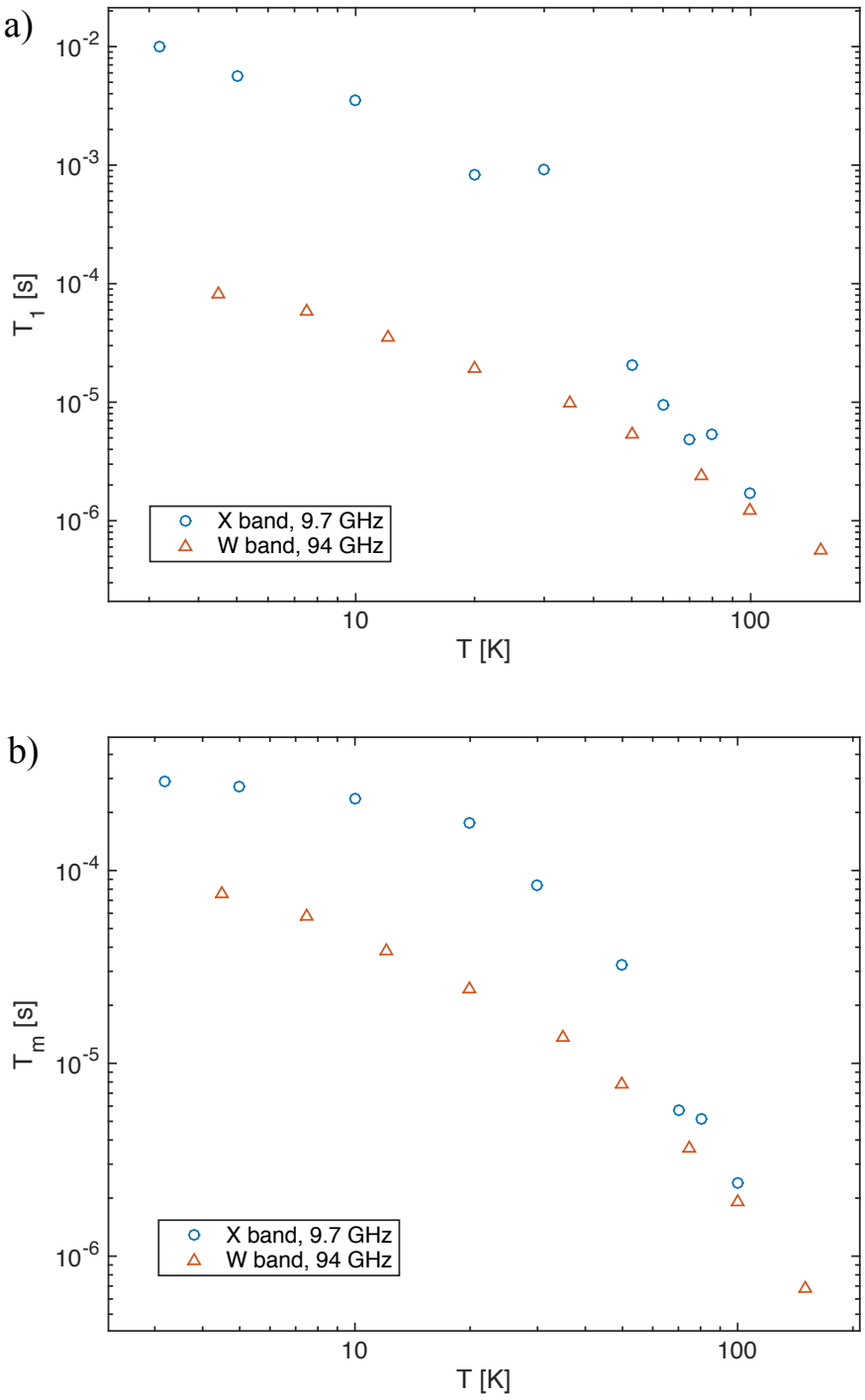

Figure 4.5: Relaxation time T_1 (upper) and T_2 (lower) of Fe^{3+}:ZnO, $|-1/2\rangle \leftrightarrow |+1/2\rangle$ transition, as a function of temperature. Comparison between 94GHz and 9.7GHz.

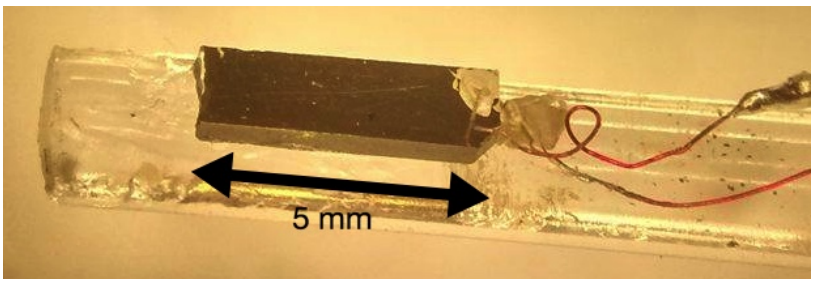

Figure 4.6: ZnO chip used for LEFE experiment. Its size is $5 \times 2 \times 0.5\,\mathrm{mm}^3$, and 100 nm of gold is evaporated on each side. The chip is electrically contacted on each side with a thin wire and silver paste.

4.1.3 Linear electric field effect experiments

Approximately 100 nm of gold was evaporated on both sides of a $d = 0.5$ mm thick 2×5 mm piece of ZnO. This is much thinner than the room temperature penetration depth of gold at $f = 10\,\mathrm{GHz}$, $\delta = \sqrt{\frac{\rho}{\pi f \mu}} \simeq 750\,\mathrm{nm}$ [73], and should thus not perturb or attenuate the microwave magnetic field much at the sample. One corner of each side was contacted to thin copper wire with silver paste, and the chip was stuck with vacuum grease to a quartz rod with a flat side, as shown in Figure 4.6. The wires were fed through a custom-made insertion rod with an N16 vacuum flange. An Agilent 33500B pulse generator was connected to the top, triggered by the E680 spectrometer. Applying a voltage V_0 with the pulse generator creates an electric field at the sample of $E_c = V_0/d$. In all LEFE experiments, the pulse amplitude was set to $V_0 = 20$ V, resulting in an electric field $E_c = 4 \times 10^4$ V/m. The thickness of the chip can vary slightly over its area since it was polished after being cut to a $5 \times 5\,\mathrm{mm}^2$ size, so the uncertainty is assumed to be about 10 µm.

The LEFE experiment was then performed by measuring a Hahn echo with a superimposed electric field: $\pi/2$ pulse at $t = 0$, π pulse at $t = \tau = 7$ µs, echo at $t = 2\tau$, and

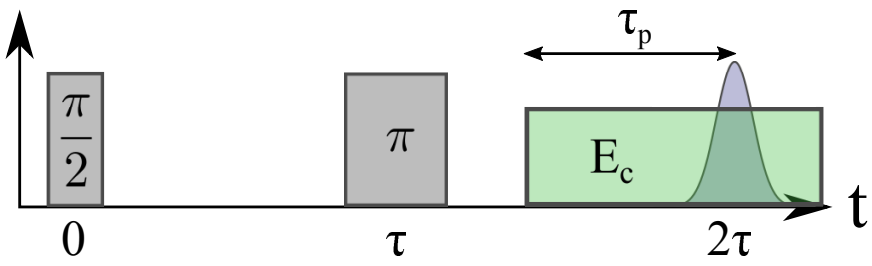

Figure 4.7: Schematic of LEFE experiment. A normal Hahn echo sequence is superimposed with an electric field pulse applied along the crystal c axis, changing the energy of the transition slightly. The time from the beginning of the electric pulse until the echo is observed is τ_p.

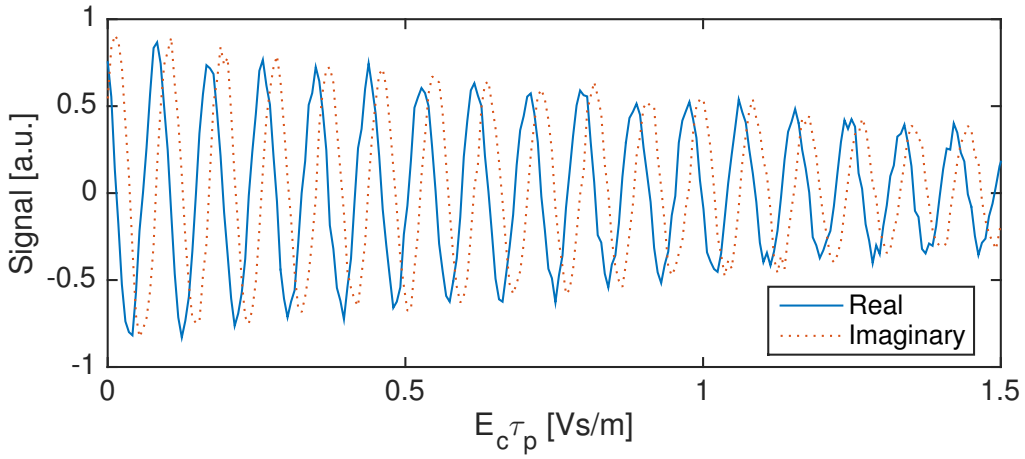

Figure 4.8: Real and imaginary intensities of Hahn echo as a function of applied electric field impulse between π pulse and echo. The pulse sequence τ is kept constant, as well as the electric field amplitude, but the electric field pulse starting time is varied.

triggering the electric field pulse at $t = 2\tau - \tau_p$, varying τ_p from 0 up to an upper limit of τ. The electric field impulse is then calculated as $J_E = E_c\tau_p$. The pulse scheme is visualised in Figure 4.7. Keeping τ fixed at 7 µs makes the results easier to interpret as there is no decay induced by varying τ.

The integral of the real (I) and imaginary part (Q) of the echo are recorded for each measurement, resulting in a plot such as the one in Fig. 4.8. The phase of the echo can be calculated at each point by $\phi = \tan^{-1}\frac{Q}{I}$. Unwrapping and plotting the phase as a function of the impulse J_E shows a linear dependence, seen in Fig. 4.9. The circles

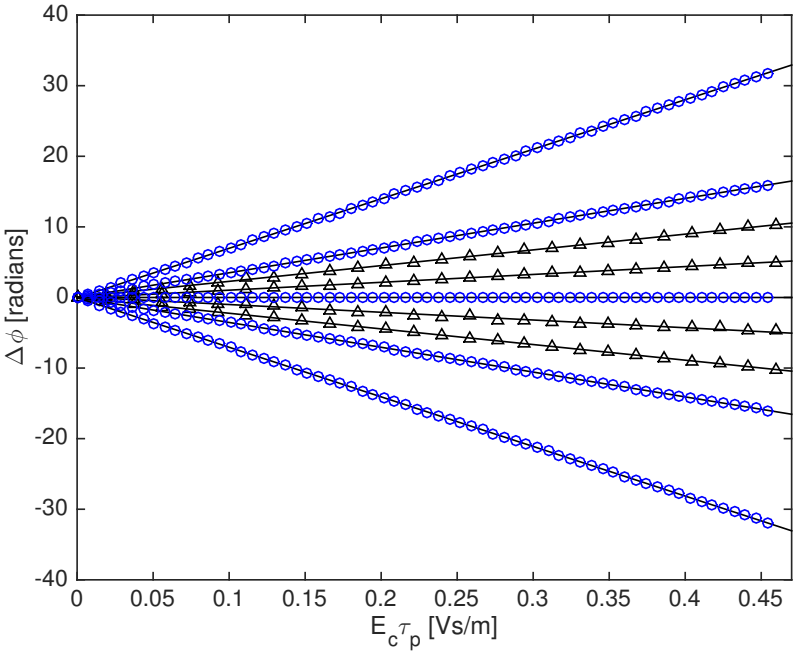

Figure 4.9: The LEFE measurement for different resonances seen in the ZnO sample. Circles correspond to Fe^{3+} and triangles correspond to Mn^{2+}.

are the Fe^{3+} resonances, and the triangles are the Mn^{2+} resonances. The parameters that we extract from the plot are

$$\kappa_{\mathrm{Fe}} = 17.6 \pm 0.3\,(\mathrm{rad/s})/(\mathrm{V/m}) \tag{4.1}$$

$$\kappa_{\mathrm{Mn}} = 5.6 \pm 0.1\,(\mathrm{rad/s})/(\mathrm{V/m}). \tag{4.2}$$

It is unclear why the κ_{Mn} measured here is so different from the one measured in the previous work [38], $\kappa = 20.8 \pm 0.2\,(\mathrm{rad/s})/(\mathrm{V/m})$. A possible explanation is that the applied voltage was not well calibrated in the original paper. In the current work, standard equipment was used, and the voltage of the triggered pulse measured on an oscilloscope to confirm.

We can use Equation (2.82) to calculate the spin-lattice coupling coefficient G_{33}:

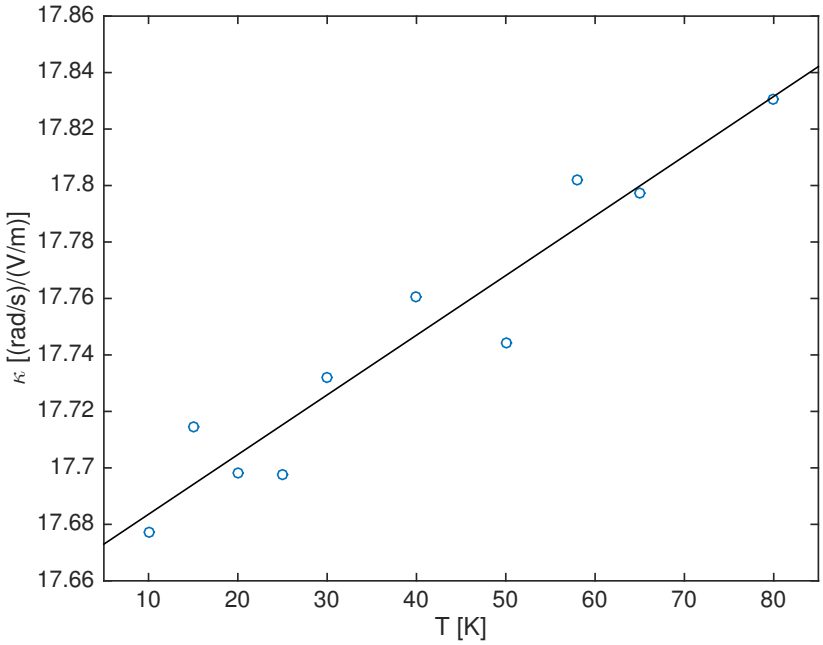

Figure 4.10: Temperature dependence of κ for Fe^{3+}:ZnO.

$$G_{33,\mathrm{Fe}} = 280 \pm 5\,\mathrm{GHz/strain} \tag{4.3}$$

$$G_{33,\mathrm{Mn}} = 89 \pm 2\,\mathrm{GHz/strain.} \tag{4.4}$$

These values compare favourably to the ones reported for NV^- centres in diamond. They have been measured with three different methods [74, 75, 76] ($G_{33} = 13.4 \pm 0.8$ GHz/strain and $G_{11} = 21.5 \pm 1.2$ GHz/strain, $G_{33} = 5.46 \pm 0.31$ GHz/strain and $G_{11} = 19.63 \pm 0.40$ GHz/strain, and $G_{33} = 17.5$ GHz/strain, respectively). The value for $G_{33,\mathrm{Fe}}$ that we extracted is about 16 times larger than the largest reported value of $G_{33,NV}$.

4.1.3.1 Temperature dependence of κ

The LEFE parameter κ was measured for different temperatures, as shown in Figure 4.10. The solid line shows a least-squares fit through the data points, showing an increase in κ with increasing temperature. Fitting a line $\kappa(T) = \kappa_0 + \kappa' T$ to the data allows us to extract the value $\kappa'/\kappa_0 = 1.20 \pm 0.23 \times 10^{-4}$. We compare this to the relative change in the Hamiltonian parameter D with temperature ($D = D_0 + D'T$), $D'/D_0 = 1.18 \pm 0.13 \times 10^{-4}$. The error is given by the 95% confidence interval for the slope of the fit. The close agreement supports the theory that the LEFE is best described by the equation

$$D = D_0(1 + \kappa E) \tag{4.5}$$

i.e., the applied electric field modifies the static zero-field splitting multiplicatively rather than additively. This is plausible if we assume the crystal field parameters to depend linearly on crystal length scales, crystal strain to depend linearly on applied electric field, and that the piezoelectric coefficient does not depend much on temperature.

4.2 Fe doped lithium niobate

In our search for the ideal system to observe SAW-spin coupling, our attention was turned to iron doped lithium niobate ($LiNbO_3$). Lithium niobate (LN) is a frequently used substrate in SAW devices [53], and iron doped LN (Fe:LN) was in fact used in a paper to investigate absorption of SAWs by electron spins [47]. It is also helpful that Fe:LN is readily available commercially due to its use in various photonics applica-

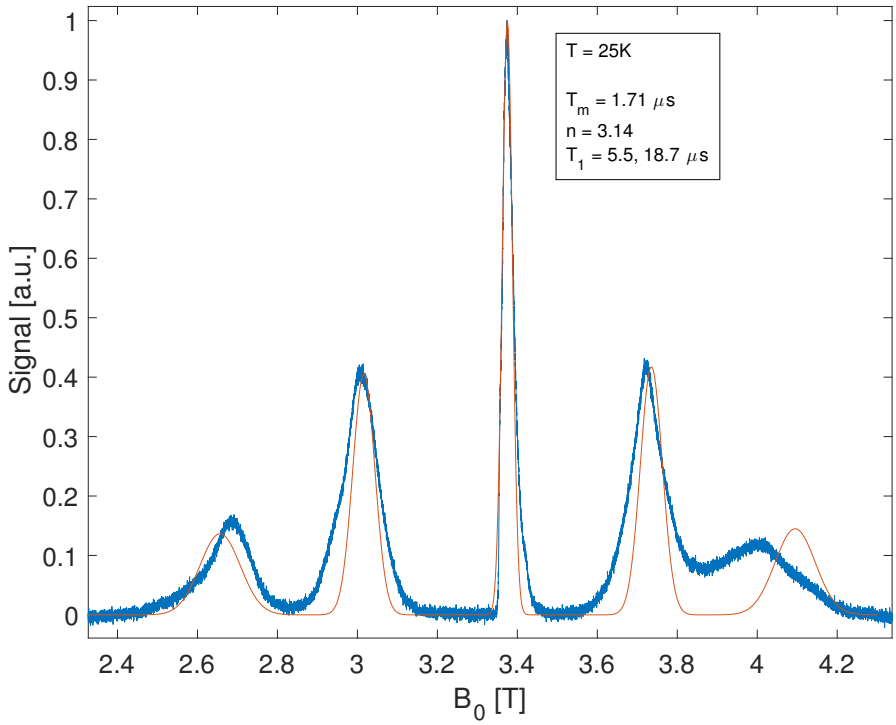

Figure 4.11: Echo detected spectrum of Fe:LN measured at W-band. The red line is a simulation with parameters $S = 5/2$, $g = 1.987$, $D = 5\,\mathrm{GHz}$ (800 MHz D strain), linewidth 30 mT and $T = 300\,\mathrm{K}$. The parameters in the text box are the fitted decay parameters for the central resonance at $B_0 \simeq 3.4\,\mathrm{T}$.

tions. We purchased a piece of LN from Del Mar Photonics, doped with 0.05% Fe_2O_3 in the melt by weight, and diced it into 5×5 mm^2 wafers and a shard of the right size for W-band ESR. The echo-detected spectrum at W-band is shown in Figure 4.11. It shows the characteristic spectrum of a $S = 5/2$ spin, with a zero-field splitting of $D \approx 5$ GHz. The red line is a simulation of a $S = 5/2$ spin with $D = 5$ GHz at $T = 300$ K. Simulating with $T = 25$ K gives a large skew in peak intensities which is not observed in the data. This along with the discrepancy in peak location leads to the conclusion that the crystal was not perfectly aligned, and the spin temperature might for some reason not be 25 K as indicated by the thermometry. The spectrum corresponds well to previously measured ESR data of Fe^{3+}:LN [46, 77].

The presence of Fe^{2+} can be difficult to measure with ESR techniques as the zero-field splitting is very large [47]. This same property makes it interesting for spin-lattice coupling experiments however. We thus proceeded to reduce the majority of Fe^{3+} to Fe^{2+} in two Fe:LN wafers by annealing them at 600°C for 30 hours, packed in lithium carbonate [45]. The wafers took on a dark grey colour instead of the previous transparent appearance. To confirm that most of the Fe had been reduced, X-band ESR spectra were recorded for both reduced and untreated wafers, with the c axis parallel to the magnetic field. As Figure 4.12 shows, the resonances seen in the untreated LN:Fe are no longer present in the spectrum of the annealed wafer.

4.2.1 Diffusion doping

The very broad linewidth seen in the Fe^{3+}:LN spectra above is believed to be due to non-stoichiometry of the LN crystal. To see if diffusion doping Fe into stoichiometric

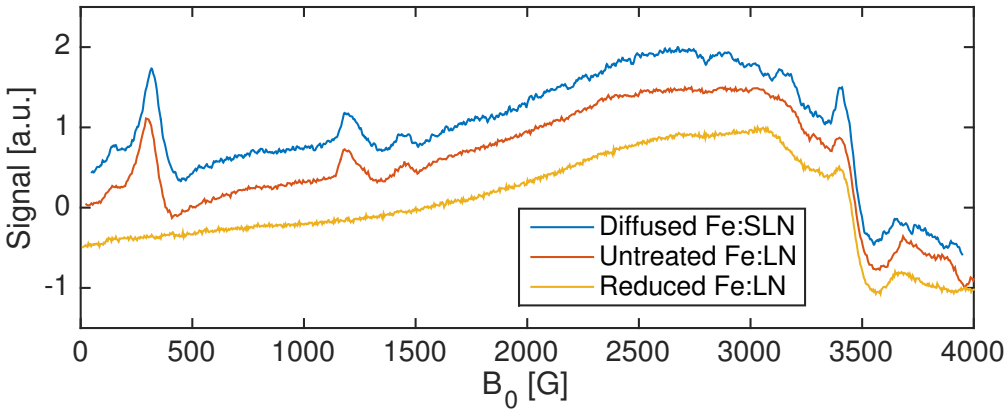

Figure 4.12: X-band ESR spectra of untreated Fe:LN, reduced Fe:LN, and SLN doped with Fe by diffusion, measured at room temperature with the c axis parallel to the magnetic field.

lithium niobate (SLN) results in narrower linewidths, we deposited 50 nm of iron on top of SLN wafers purchased from MTI Corporation. We then diffused the Fe into the SLN by annealing the wafers at 1050°C for 24 hours [50]. The reported diffusion constant at these parameters was about 500 nm^2/s.

The density of evaporated iron thin films is approximately the same as that of bulk iron, about 8 g/cm^3 [78]. That translates to about 8.7×10^{22} $atoms/cm^3$, or a fluence of $8.7 \times 10^{15}/cm^2$ per nm thickness of the layer. The fluence of our 50 nm layer is thus approximately $4.4 \times 10^{17}/cm^2$. Annealing for approximately 24 hours yields a surface density of about $5 \times 10^{20}/cm^2$ and a diffusion depth of about 10 µm.

To assess the success of the diffusion process, the sample was measured with CW-ESR at X band to compare to the commercial Fe:LN. As Figure 4.12 shows, the spectrum is very similar to the untreated Fe:LN, but was achieved at considerably higher power and modulation. We were hoping for a narrower linewidth, but it is still very broad. The surface of the diffused SLN looks quite rough under a microscope, although this is

something that would need to be verified with a surface profiling. Although the spin linewidth does not seem to be improved, diffusion-doped Fe:LN can still be considered for SAW spin resonance experiments due to the high impurity densities achievable, if the surface quality is determined to be acceptable.

Chapter 5

Surface acoustic wave devices

A major aim of this project has been to couple surface acoustic waves (SAWs) to spin impurities. Due to the promising electric field effect observed in background work on the electric field effect of Mn^{2+} impurities in ZnO crystals [38], the first experiments focused on making SAW devices on bulk ZnO. The results from the SAW device fabrication and characterisation at low temperature were published and are presented in the following section.

Inspired by work that did not receive much attention so far [47], we started considering iron-doped lithium niobate as a strong candidate to observe SAW-spin coupling. We present measurements of SAW resonators on Fe:LN.

5.1 SAW devices on ZnO

The first SAW device we made on bulk ZnO was a set of delay lines with two different pitches. This allowed us to observe temperature dependence up to relatively high temperatures of 20 K. We then proceeded to make one-port resonators that are much more sensitive to dissipation effects.

5.1.1 Delay line

The delay line device was designed with two input transducers in parallel, on either side of the centre conductor of a coplanar waveguide input line. The device is pictured in Figure 5.1(a), and a schematic view of the IDT design is shown in Figure 5.1(b). One side operates at a SAW wavelength of $\lambda = 4\,\mu\text{m}$ and the other at $\lambda = 6\,\mu\text{m}$. Each IDT has 20 finger pairs, and at 2 mm separation, there is an identical mirrored transducer for output. This parallel IDT design was used simply for convenience of gathering more data with a single device.

Figure 5.2 shows the transmission of the delay line, S_{21}, as a function of frequency at 50 mK. The attenuation of the cables in the cryostat has been subtracted. Both the $\lambda = 6\,\mu\text{m}$ and $\lambda = 4\,\mu\text{m}$ transducers are active. We observe multiple transmission peaks, with the fundamentals at $f_1 = 446.4\,\text{MHz}$ (arising from the $\lambda_1 = 6$ µm transducers) and $f_2 = 669.5\,\text{MHz}$ ($\lambda_2 = 4$ µm transducers), implying a SAW velocity of $v \simeq 2678\,\text{m/s}$ under the IDTs. We find higher harmonics in the transmission spectrum at $3f_1$, $3f_2$, $5f_1$, $5f_2$, $7f_1$ and $9f_1$, demonstrating that filters can be operated at frequencies multiple times higher than $f = v_s/(2p)$.

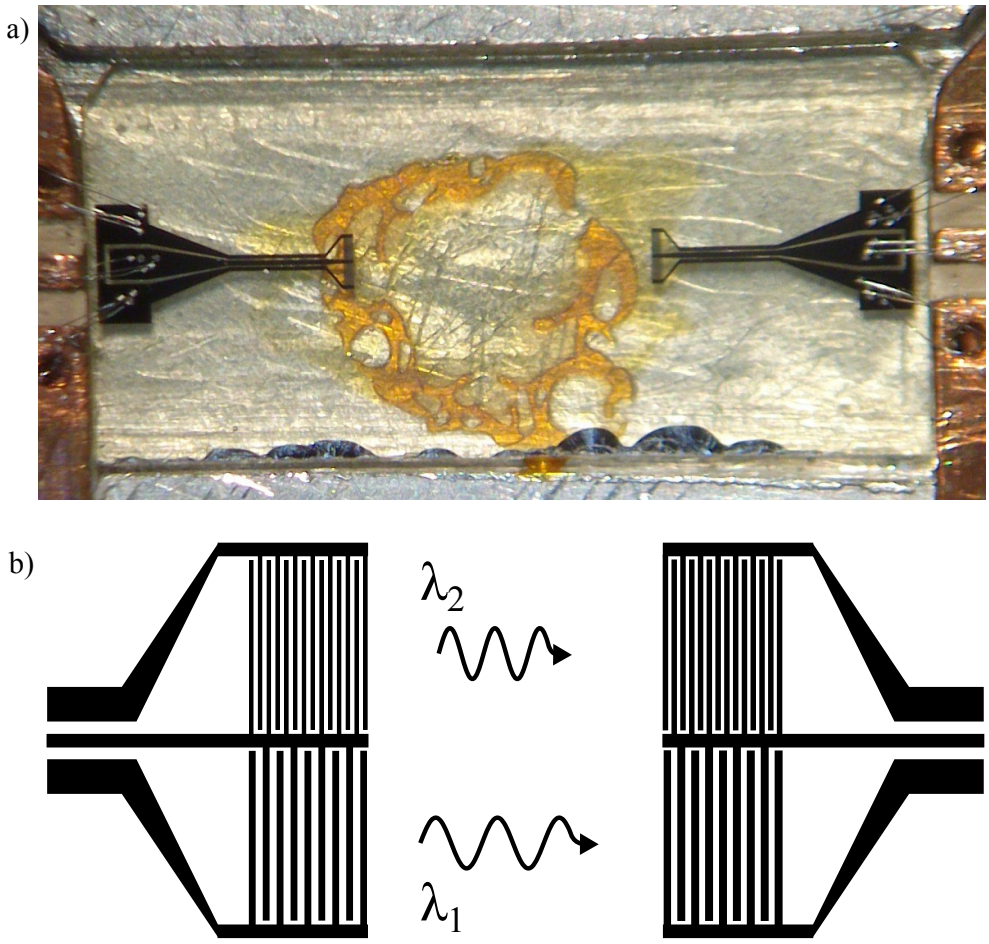

Figure 5.1: (a) Photograph of the SAW delay line on ZnO (transparent), mounted in the sample holder. The wafer is 10×5 mm^2. The blob seen in the background is GE varnish used to glue the chip down. (b) Schematic of the double IDT design.

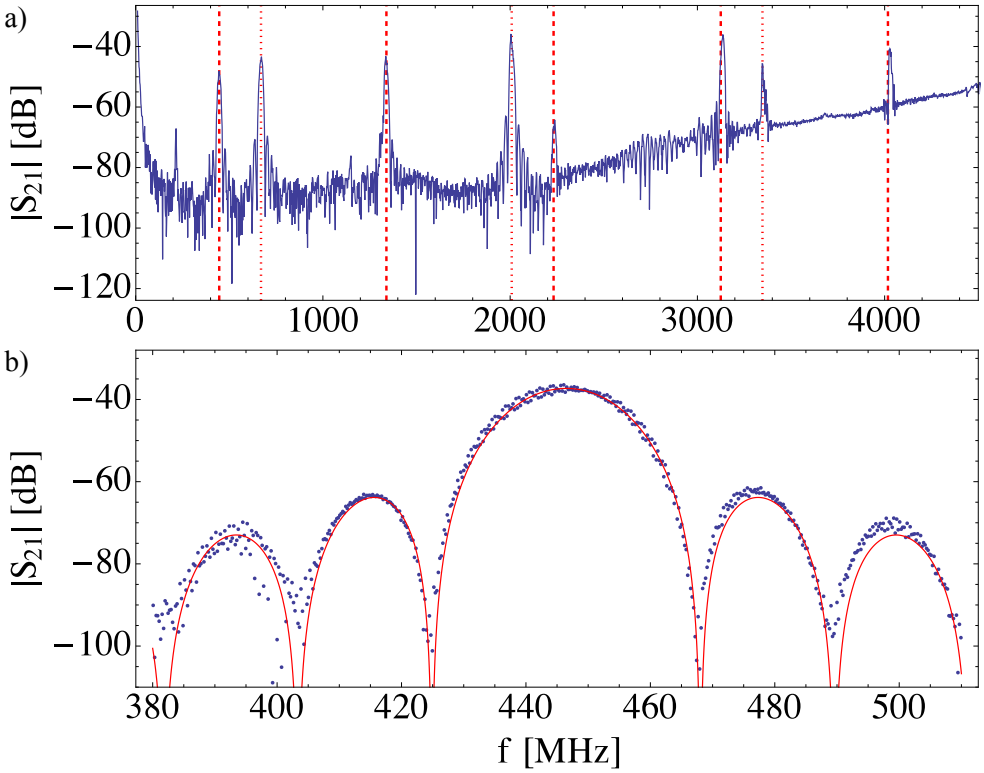

Figure 5.2: (a) Transmission spectrum of a delay line with 4 µm and 6 µm transducers. Multiple odd harmonics are seen. The 6 µm fundamental mode at $f = 446\,\mathrm{MHz}$ and its third, fifth, seventh and ninth harmonics are marked with vertical dashed lines, and the 6 µm modes up to fifth harmonic are marked with dotted lines. (b) Zoom of transmission spectrum at the fundamental mode ($f = 446\,\mathrm{MHz}$) of the delay line at 50 mK. The solid line is a fit of Equation (5.1) to the data.

Simple interdigital transducers of the kind we use here are expected to give rise to a transmission spectrum close to the fundamental frequency that depends on frequency as shown in Equation (2.100), or more simplified,

$$|S_{21}| = A\,\mathrm{sinc}^4\left(\pi N \Delta f / f_0\right) \tag{5.1}$$

where N is the number of IDT fingers, and Δf is the detuning from the center frequency f_0 [53]. Figure 5.2(b) shows a measurement of the transmission spectrum close to f_1 and a fit to Equation (5.1), demonstrating that the behaviour of our device is close to ideal.

Figure 5.3(a) shows the transmission of the delay line measured at f_1 as a function of temperature. The temperature dependent attenuation of the cryostat cables has been calibrated out. The delay line transmission is only weakly temperature dependent below 50 K, but drops slowly at higher temperatures up to about 200 K, above which it drops very sharply. This decrease in transmission is accompanied by a shift in f_1; fitting the transmission to Eq. 5.1 to obtain f_1 at each temperature allows us to derive the change in the SAW velocity with temperature, as shown in Fig. 5.3(b).

At low temperatures, the ZnO substrate is not electrically conductive. However, at elevated temperatures thermal excitation of impurities leads to n-type doping and a non-zero conductivity [79]. Fig. 5.3(c) shows the measured resistivity of our ZnO substrate as a function of temperature. Below about 120 K, the resistance is too high to measure using our apparatus. At higher temperatures, there are several intervals in temperature where the resistivity drops, which may be due to different impurities becoming ionised. These changes in resistivity are correlated with drops in

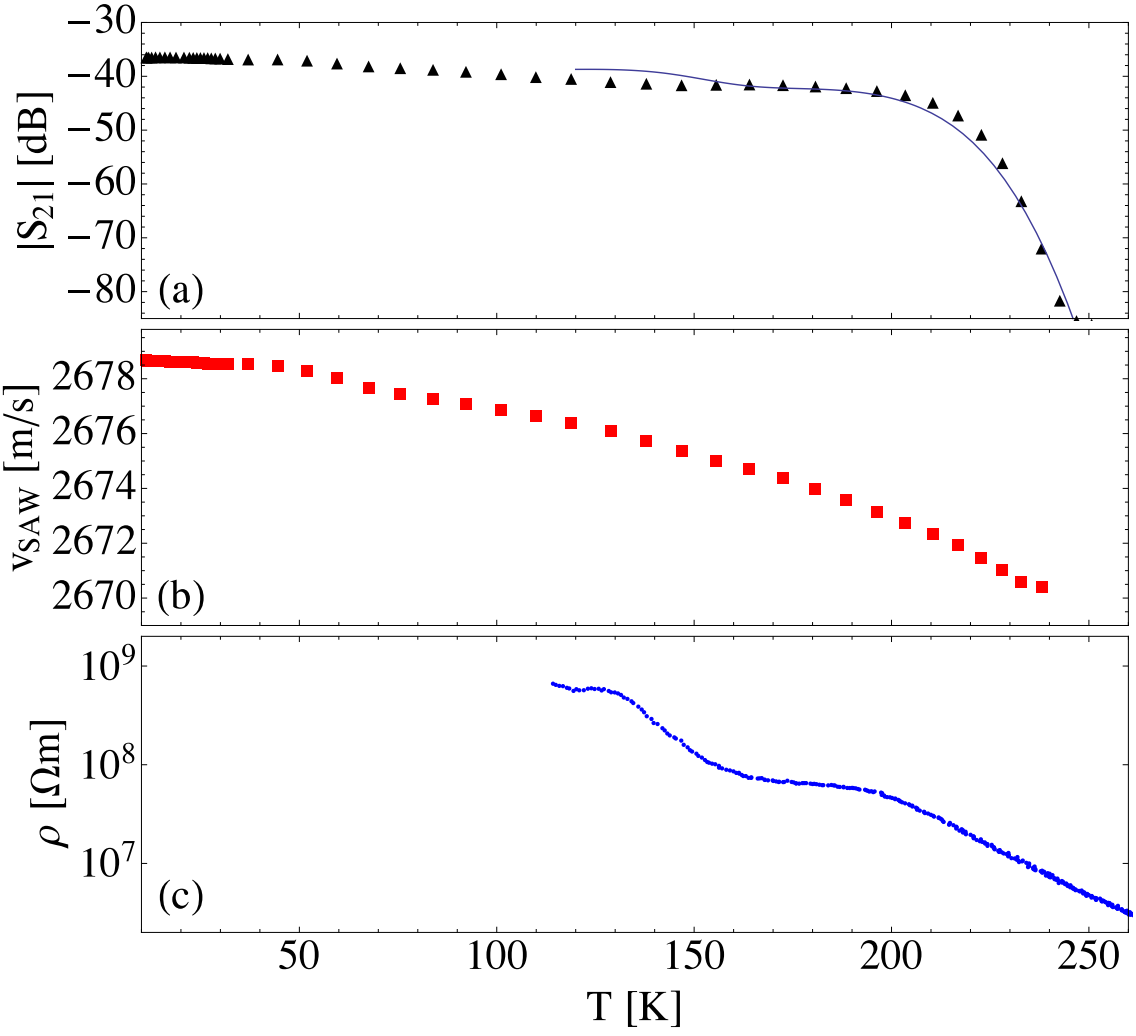

Figure 5.3: (a) Transmission amplitude S_{21} of the fundamental mode ($f = 446$ MHz) of the delay line as a function of temperature T. The solid line is a fit of transmission attenuating linearly with conductivity. (b) SAW velocity as a function of temperature, calculated by fitting the peak frequency and using $v_{SAW} = \lambda_0 / f_{SAW}$. (c) Resistivity of the ZnO substrate as a function of temperature.

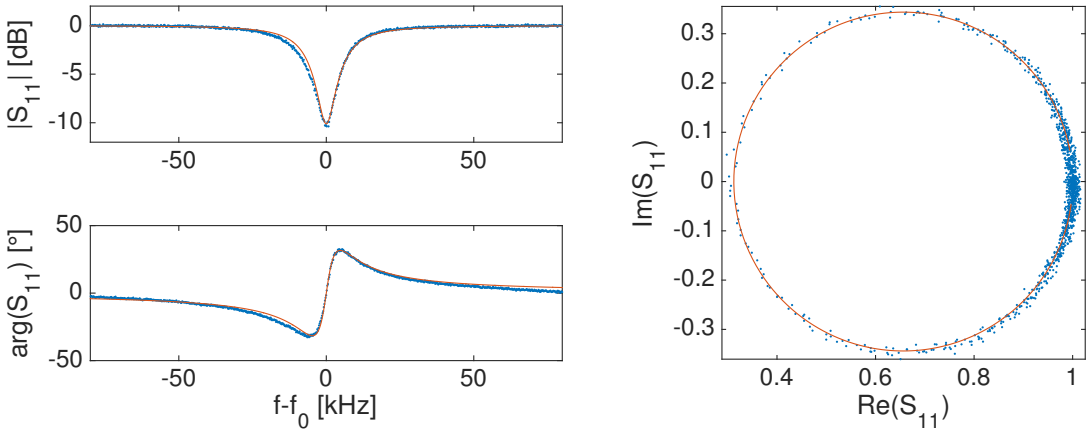

Figure 5.4: Reflection S_{11} of SAW resonator on ZnO, fitted with Equation (2.103). Fit parameters are $f_0 = 1.677781\,\text{GHz}$, $Q_e = 289 \times 10^3$ and $Q_i = 151 \times 10^3$. Measured at $T = 10\,\text{mK}$ at input power $-50\,\text{dBm}$.

$|S_{21}|$, because the electric field component of the SAW can drive dissipative currents, thereby damping the SAW. The solid line is a fit of the function $f(T) = A\,e^{-B/\rho(T)}$ to the data, where $A = -38.3$ dB and $B = 2.65 \times 10^8$ Ωm are fit parameters. This model assumes that SAW dissipation is linear in the DC conductivity of the ZnO. Deviations from this simple model may be due to the frequency dependent absorption of different defect centres in the crystal.

5.1.2 Resonator

We next fabricated a one-port SAW resonator on ZnO. The resonator has an IDT with 21 fingers ($\lambda = 1.6$ µm) and is measured in reflection. On either side of the transducer there are gratings with 1750 fingers, separated from the IDT by the width of a finger, meaning that there is no discontinuity between the IDT and grating.

Figure 5.4 shows the reflection S_{11} from the one-port resonator as a function of frequency around its resonant frequency of $f_0 \simeq 1.677781\,\text{GHz}$, measured at an input

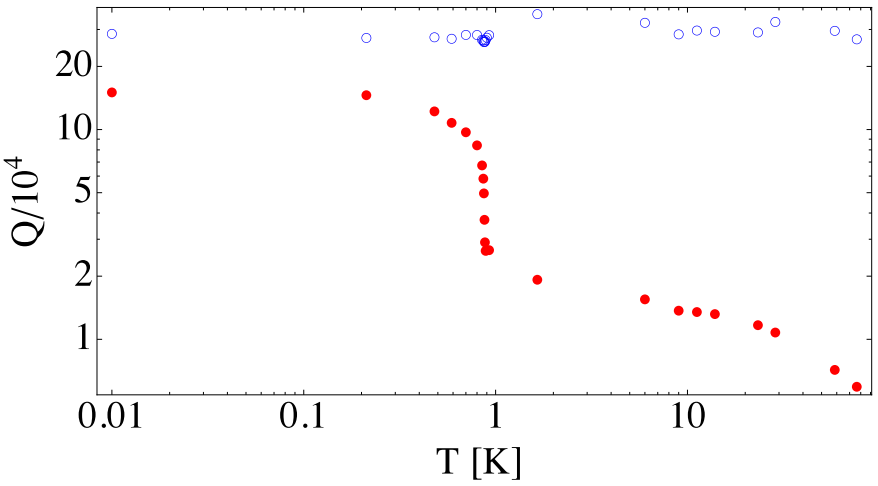

Figure 5.5: Dependence of resonator internal quality factor Q_i (filled circles) and external quality factor Q_e (empty circles) on temperature.

power of $-50\,\mathrm{dBm}$ and at $T = 10\,\mathrm{mK}$. The complex data is fitted to Equation (2.103) and yielding $f_0 = 1.677784$ GHz, $Q_e = 289 \times 10^3$ and $Q_i = 151 \times 10^3$.

Figure 5.5 shows the dependence of Q_i (filled circles) and Q_e (empty circles) on temperature. As the temperature increases from its base value, the quality factor Q_i decreases, and is particularly strongly temperature dependent as T approaches 1 K. This dependence is likely to be attributable to quasiparticle scattering in the Ti/Al bilayer, and its transition from the superconducting to normal state at $T \simeq 850\,\mathrm{mK}$. In contrast, Q_e is observed to be approximately temperature independent. As Equation (2.101) details, Q_e is dependent on several properties, which can be concluded not to have a strong temperature dependence.

At base temperature, the quality factor Q_i reaches values near 1.5×10^5, which at the time of measurement was close to the highest quality factors reported in SAW resonators fabricated on other materials [80]. It is interesting to note that in our device, superconducting electrodes increase Q_i by about a factor of 5.

Since the publication of our results, our group has produced SAW resonators on quartz with up to three times higher quality factor than we achieved on ZnO, by introducing a large gap between the IDT and the mirrors [54]. As shown in that paper, the quality factor decreases with frequency as $Q_i \propto f^{-2}$, which is important to bear in mind when considering SAWs for quantum information applications.

5.2 SAW resonator on lithium niobate

Having identified iron doped lithium niobate (LN) as a high potential system for SAW-spin coupling, resonators were fabricated on LN doped with 0.05% iron. Fabrication on LN can be tricky due to a few reasons. Firstly, it has a very large dielectric constant [43], calling for very different aspect ratios of coplanar waveguide structures than traditionally used substrates with an order of magnitude smaller dielectric constant. Secondly, LN is highly pyroelectric. This can cause trouble during procedures that call for baking the wafer, requiring modifications to the baking protocols. Temperature change causes a build-up of charge on the surfaces of the wafer, resulting in abrupt discharge if the surfaces are not shorted and the temperature changes too fast. This can potentially cause cross-linking of the resist, or even fracture the crystal. One way to avoid problems is to ensure that any temperature change happens slowly enough for the charge to dissipate.

With this in mind, resonators were fabricated using PMMA, ensuring a slow bake by putting the wafer on the bake plate before ramping the temperature. For the first design, four resonators were fabricated on the same chip, with identical design. The design consisted of a one-port resonator with $\lambda = 1600\,\mathrm{nm}$, with an IDT of 21 fingers and reflecting gratings of 1000 fingers, $d = 743.2$ µm apart. The fabrication was successful at this relatively coarse featured lithography. Literature parameters for SAWs on LN [81] are shown in Table 5.1, and compared to some measured values for our resonator at $T = 300\,\mathrm{K}$ and $10\,\mathrm{mK}$. We focused on the X propagation direction at low temperatures as this had a higher Q_i. There was only a factor of 2 improvement of

Table 5.1: SAW parameters on lithium niobate [81].

Propagation direction (Z cut)	X	Y
Literature values		
Free velocity, v_f [m/s]	3798	3903
Metallised velocity, v_m [m/s]	3788	3859
Electromechanical coupling, K^2 [%]	0.53	2.25
$f_f(\lambda = 1600$ nm) [GHz]	2.374	2.439
$f_m(\lambda = 1600$ nm) [GHz]	2.367	2.412
Measured values, $T = 300\,\mathbf{K}$		
f [GHz]	2.33	2.38
Q_i (from fit)	7000	2500
Q_e (from fit)	30000	12000
Measured values, $T = 10\,\mathbf{mK}$		
f [GHz]	2.35	-
Q_i (from fit)	13000	-
Q_e (from fit)	97000	-

Q_i at low temperature, but the resonator may have additional losses from accumulated dirt or scratches as it was re-bonded between the measurements.

The response of the resonators at room temperature is shown in Figure 5.6. As expected, the central frequency depends on the propagation direction, and we measure resonant frequencies $f_X \simeq 2.33$ GHz and $f_Y \simeq 2.38$ GHz. This is a bit lower than expected from the literature values for the SAW velocity. Fitting single resonances with Equation (2.103) gives internal and external quality factors as shown in Table 5.1. Multiple resonances are seen due to the long cavity length. The separation between the resonances (free spectral range) is 4.6 and 4.9 MHz for X and Y propagation, respectively. From this, we can derive an effective cavity length $L_c = v_s/\Delta f_{\mathrm{FSR}}$, and thus an effective penetration depth of the SAW into the gratings $l_{\mathrm{eff}} = (L_c - d)/2$. Using the literature values for the SAW velocities, we get $l_{\mathrm{eff,X}} = 41$ µm and $l_{\mathrm{eff,Y}} = 27$ µm. This can be assumed a good approximation, as the short penetration depth

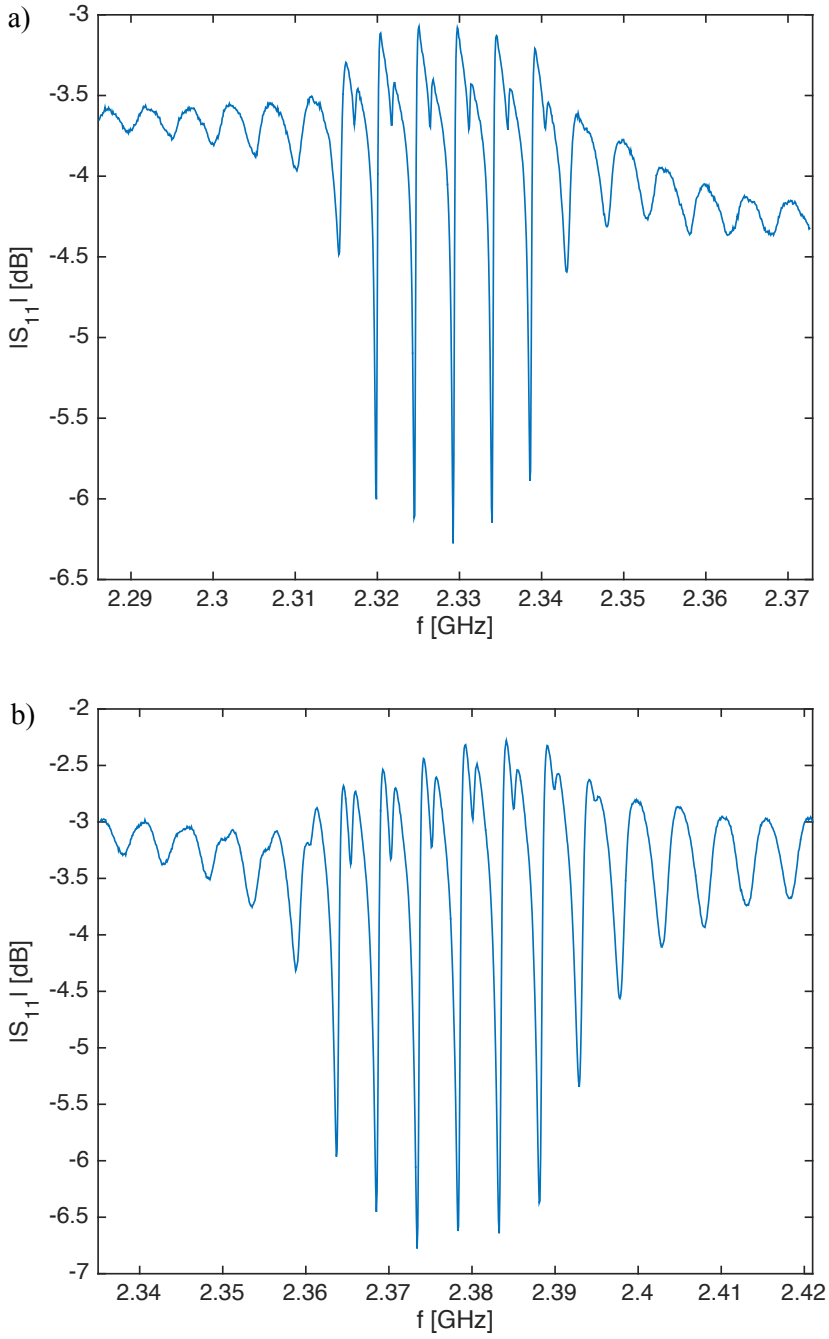

Figure 5.6: Response of one-port SAW resonators on Z-cut lithium niobate at room temperature. a) X propagation. b) Y propagation.

suggests that the wave exists mostly on the free surface without the grating or IDT. This also means that the gratings can be made much shorter without affecting the quality factor.

Chapter 6

Surface acoustic wave spin resonance

In this chapter we present the results from our ESR-type experiment using a SAW resonator rather than a traditional ESR resonator. We will refer to this experiment as surface acoustic wave spin resonance (SAWSR). As discussed earlier, there has been some research on acoustic excitation of spin resonance, called acoustic paramagnetic resonance (APR) [33]. However, only one attempt seems to have been made to measure spin resonance directly with surface acoustic waves [47]. In this work, a delay line was fabricated on lithium niobate doped with iron, and the attenuation of the SAW signal measured as a function of magnetic field. Although the theory in the paper seems valid, the results are not conclusive. It is worth repeating the experiment using a SAW resonator rather than a delay line, as this should increase the sensitivity significantly.

We fabricated SAW resonators on Z-plane iron doped lithium niobate doped with 0.05% of Fe_2O_3 in the melt. As described previously, the substrate was sourced from Del Mar Photonics. The resonators were fabricated with a wavelength of $\lambda =$

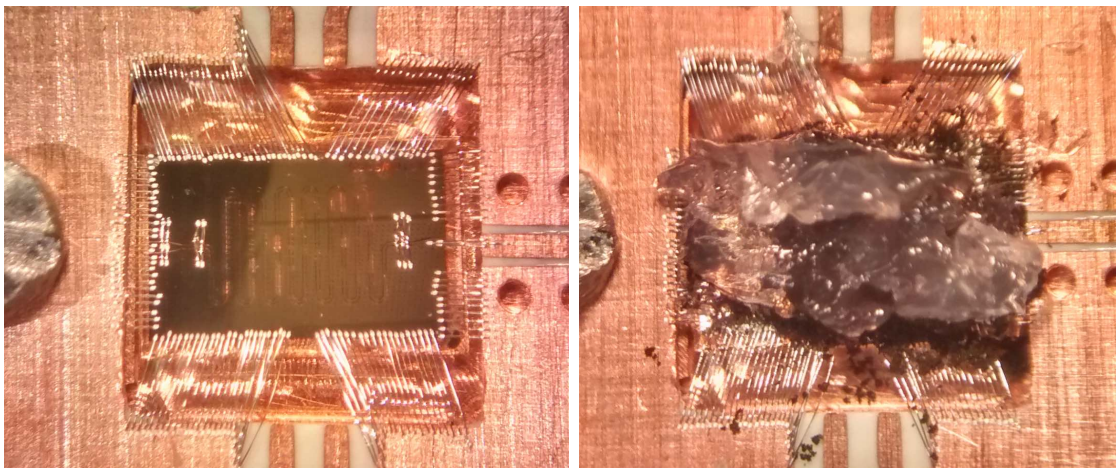

Figure 6.1: Superconducting niobium-titanium-nitride CPW resonator. *Right:* After DPPH has been deposited and secured with vacuum grease.

1600 nm, resulting in resonant frequencies of about 2.33 GHz and 2.38 GHz at room temperature, depending on propagation direction.

Our experiment is completely analogous to a CW ESR experiment, but with a SAW resonator instead of the ESR cavity. Figure 3.9 shows the sample holder used in the experiment. The bottom is made of copper, and the design has 4 ports. The lid is made from machinable plastic in order to allow the modulation magnetic field from the little coil on top to penetrate. The setup of the experiment is described in Section 3.7. The measurements are carried out in a helium cryostat, and the signal reflecting off the resonator is measured with a lock-in amplifier which drives the modulation field. What this experiment lacks compared to traditional CW-ESR is tuneable coupling, so unfortunately we are not able to critically couple the resonator. We measure the signal from the resonator at a single frequency, at the bottom of the resonance, and sweep the magnetic field.

6.1 Testing setup with CPW resonator

To ensure that the measurement setup actually outputs a good signal when measuring a spin-coupled system, we did a test experiment using a coplanar waveguide resonator with DPPH spins deposited on top. In this case we used a CPW resonator made from a high-temperature superconductor with large critical magnetic field, NbTiN. The substrate is quartz, the film thickness is 110 nm, and the pattern was produced using photolithography and reactive ion etching. The dimensions of the resonator are designed for a resonant frequency of about 4 GHz. The chip bonded in the sample holder is shown on the left in Figure 6.1. A fairly large amount of DPPH was placed directly on the resonator and then secured in place with a blob of vacuum grease. The field at which the microwave field of the 4 GHz resonator should be resonant with the DPPH spins is $B_0 = hf/g\mu_0 \simeq 144\,\mathrm{mT}$.

The setup described in Section 3.7 was then used to measure the absorption of DPPH at $T = 4\,\mathrm{K}$. As hoped for, we measured a magnetic resonance at about 140 mT, shown in Figure 6.2. The modulation voltage was varied to ensure that it was not broadening the linewidth at the maximum amplitude of 5 V. This convinces us that the setup works as expected, and we can move on to look for spin absorption using a SAW resonator.

6.2 SAW resonator on Fe^{2+}:LN

As explained in [47], the spin structure of Fe^{2+}:LN is $S = 2$ with $D \simeq 1.2\,\mathrm{THz}$, making it impossible to probe allowed transitions with microwave ESR techniques.

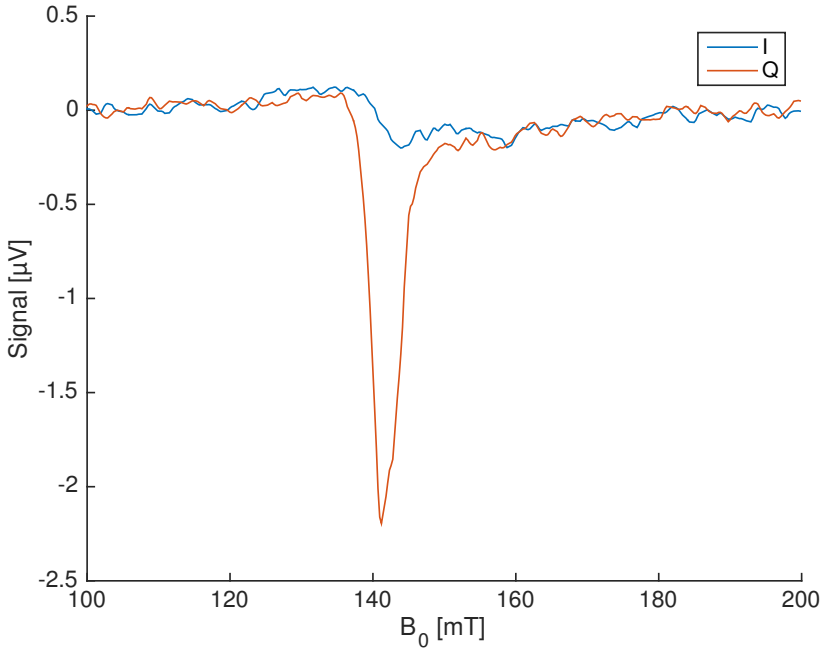

Figure 6.2: Spin resonance of DPPH on a superconducting CPW resonator with $f_0 = 4\,\mathrm{GHz}$.

We are, however, aiming to excite the "forbidden" $\Delta m = 2$ transition between the $|+1\rangle$ and $|-1\rangle$ states. The spin-lattice interaction Hamiltonian (Equation (2.73)) explicitly allows these transitions, depending on the values of matrix elements of G. The values calculated in [47] suggest a very strong coupling compared to what we measured in Fe^{3+}:ZnO. Figure 6.3 shows the energy diagram of our system with the magnetic field parallel to the anisotropy axis, with an expanded version on the right to visualise the forbidden transition using a 2.37 GHz resonator.

The SAW resonator used was one of 4 identical resonators on a single $5 \times 5\ \mathrm{mm}^2$ chip with $\lambda = 1.6\,\mu\mathrm{m}$, for a resonant frequency of about 2.37 GHz. Figure 6.4 shows a zoomed view of the resonance used in the SAWSR experiment. Although there are undesirable resonances near the main resonance, it is well fitted close to the main resonance by a S_{11} function with $Q_i \simeq 17500$ and $Q_e \simeq 105000$. The deviation of the

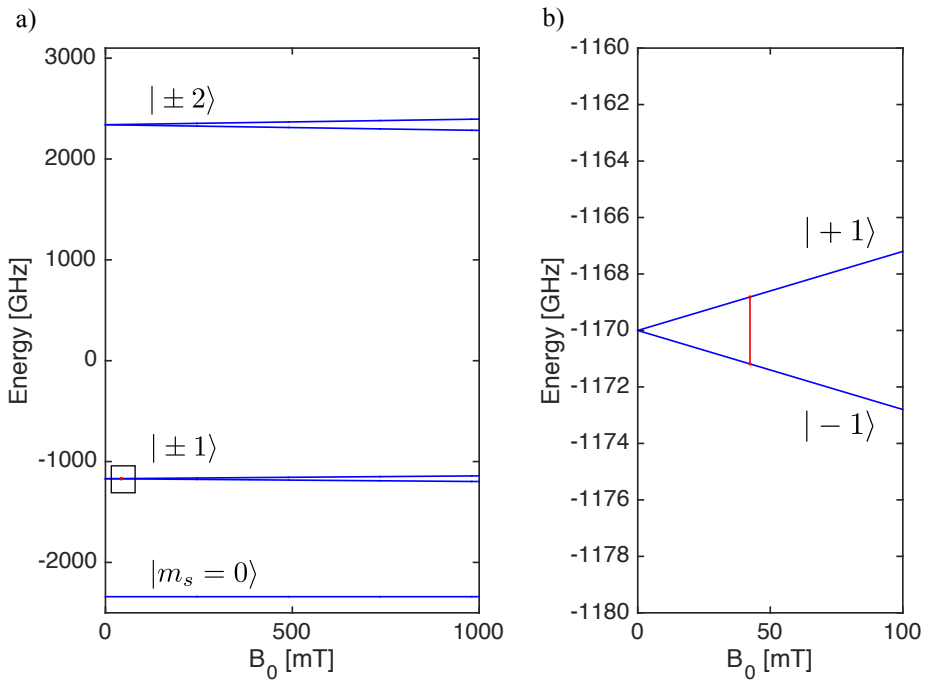

Figure 6.3: a) Energy levels of Fe^{2+}:LN with $\boldsymbol{B}_0 \parallel c$. The box indicates the approximate view shown in (b). b) Vertical bar indicates the $|-1\rangle \leftrightarrow |+1\rangle$ transition with a 2.37 GHz resonator.

fit from data away from the main resonance may be due lateral modes or imperfections in fabrication. The experiment was performed at $T = 25\,\mathrm{K}$. At this temperature, the occupation of the $|\pm 1\rangle$ states is still about 10% of the total number of spins, but drops off quickly as you decrease the temperature.

The output power of the RF source was set to its maximum of 16 dBm, and the attenuation was 40 dB, plus an additional 20 dB of attenuation in the cables. The power delivered to the sample can then be assumed to be about -37 dBm, or 200 nW. With this setup, a clear ESR signal was achieved. Figure 6.5 shows typical data as acquired from the lock-in amplifiers. As explained in Section 3.7.1, the data needs to be properly phased by post-processing to recover a meaningful signal. The raw signal (Figure 6.5(a)) is rotated in $X - Y$ and $I - Q$ space until there is nothing left in the

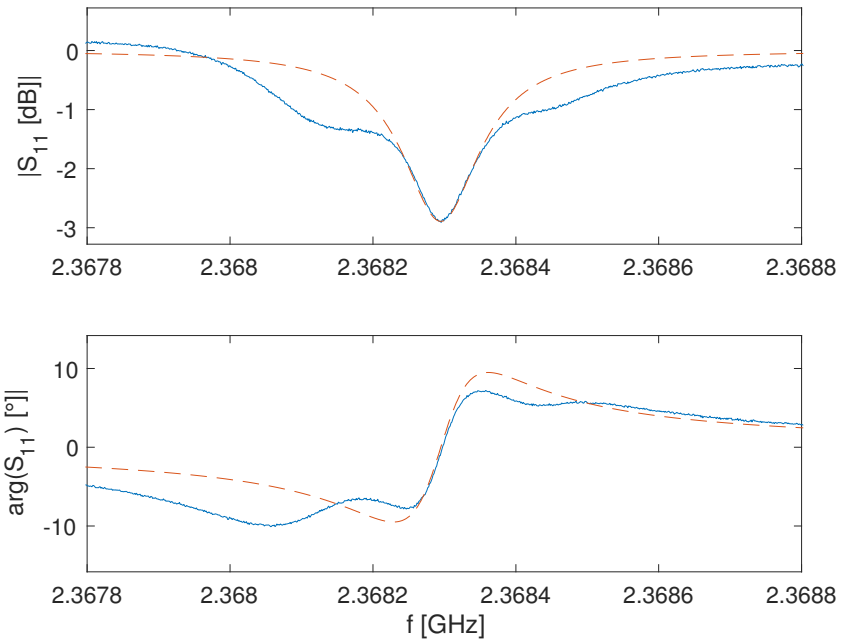

Figure 6.4: Resonance used for the SAWSR measurements. Dashed line corresponds to $Q_i \simeq 17500$ and $Q_e \simeq 105000$.

Y channel (Figure 6.5(b)). The optimal angles θ_{IQ} and θ_{XY} remain similar for all measurements, as θ_{XY} is essentially the phase delay caused by the induction of the modulation coil, and θ_{IQ} is determined by the effective path length of the signal from source to measurement.

Figure 6.6(a) shows the signal position acquired at different angles. The signal at $\theta \simeq 0°$ is centred at around 53 mT. For a spin system with $S = 2$ and a microwave frequency of $f = 2.37$ GHz, the transition $|+1\rangle \leftrightarrow |-1\rangle$ occurs at a field of $B_0 = hf/2g\mu_B \simeq 42.3$ mT for $g = 2$. The difference could be explained by an effective $g \simeq 1.6$, although previous work suggests that $g \simeq 2$ [47, 48]. The transition moves to higher field as θ is increased, as expected from simulation. The solid and dashed lines show the simulation results for $g = 2$ and $g = 1.6$, respectively. The data point at $\theta \simeq 55°$ seems to be an outlier, and our assumption is that this is an error in

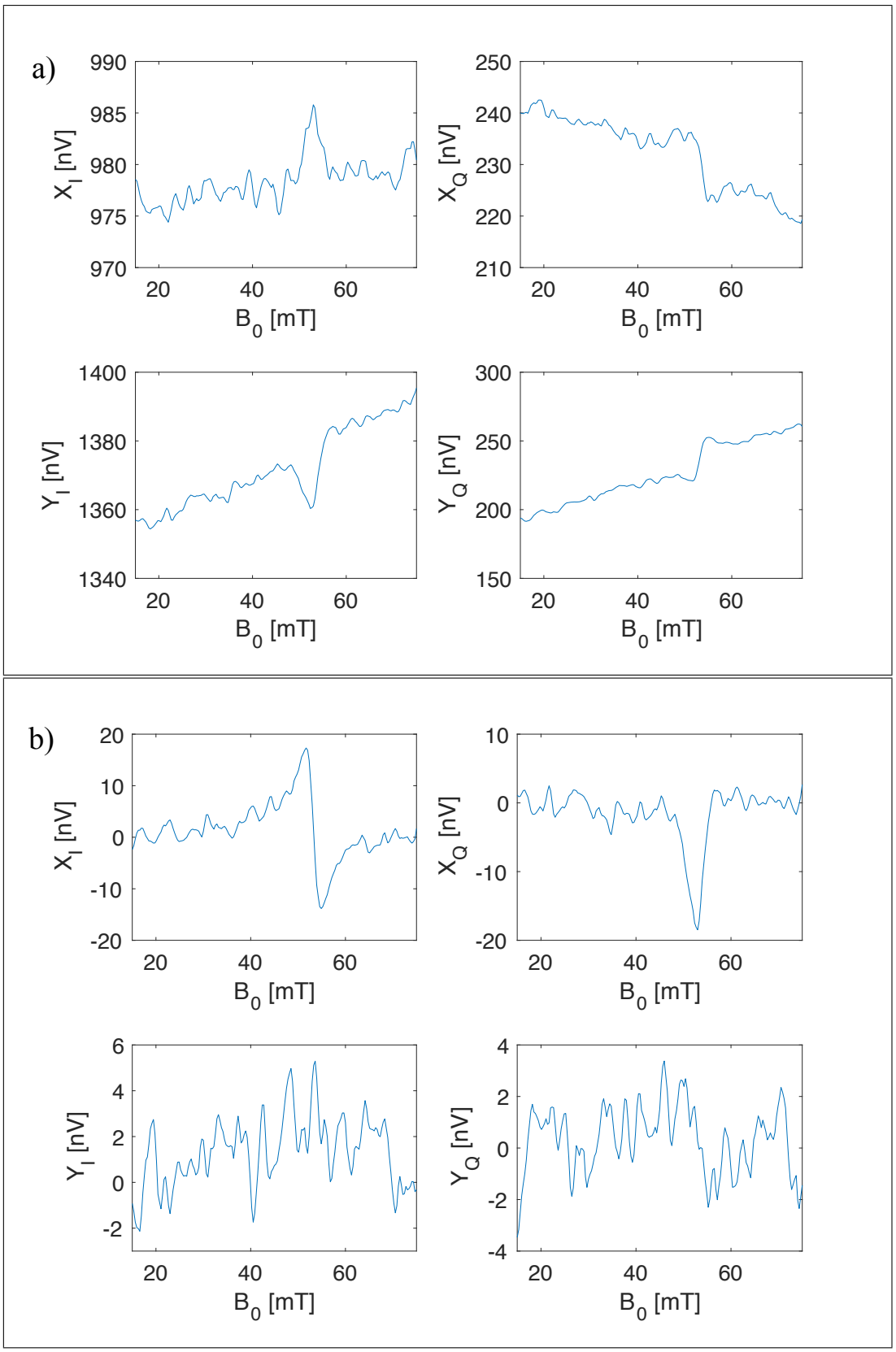

Figure 6.5: a) Raw data from a SAWSR measurement, $\theta \simeq 10°$. b) Data after proper phasing and background fitting.

the angle determination due to the low precision method used (angle estimated from mark on the side of the probe). This was subsequently improved by attaching a rod to the probe. There is quite large uncertainty in the angle due to the rudimentary angle adjustment used, and the magnetic field is known to occasionally have errors up to several percent at low fields, as the magnet is designed for fields up to 6 T.

A couple of the measurements appear to show a splitting of the resonance, as a signal of lower intensity is observed that remains close to 50 mT. This could be due to non-equivalent spin sites existing in the crystal, or possibly an unknown spin species. However, while the additional resonance had similar intensity as the main resonance, it did not appear consistently between measurement runs. It should be noted that when two resonances are visible, they require different phasing angles θ_{IQ} and also slightly different θ_{XY} to maximise the signals.

Figure 6.6(b) shows the intensity of the resonances. Since the signal-to-noise ratio is rather low, we define the intensity as the product of the peak-to-peak line width in mT and the peak-to-peak amplitude in V. An important feature is that the intensity of the main resonance does not tend to zero near $\theta = 0°$, as would be expected if it were a magnetically excited forbidden transition. This would also be expected if it was due to a strain modulation of the parameter D, in which case the coupling strength to the $|+1\rangle \leftrightarrow |-1\rangle$ transition should go to zero at zero angle. The behaviour observed suggests that the coupling is due to a modulation of the zero-field splitting parameter E, or in other words the spin-lattice coupling parameter G_{11} or G_{22}.

To understand more about the nature of the two resonances observed, we varied the temperature to see how the relative intensity of the two would change. Figure 6.7

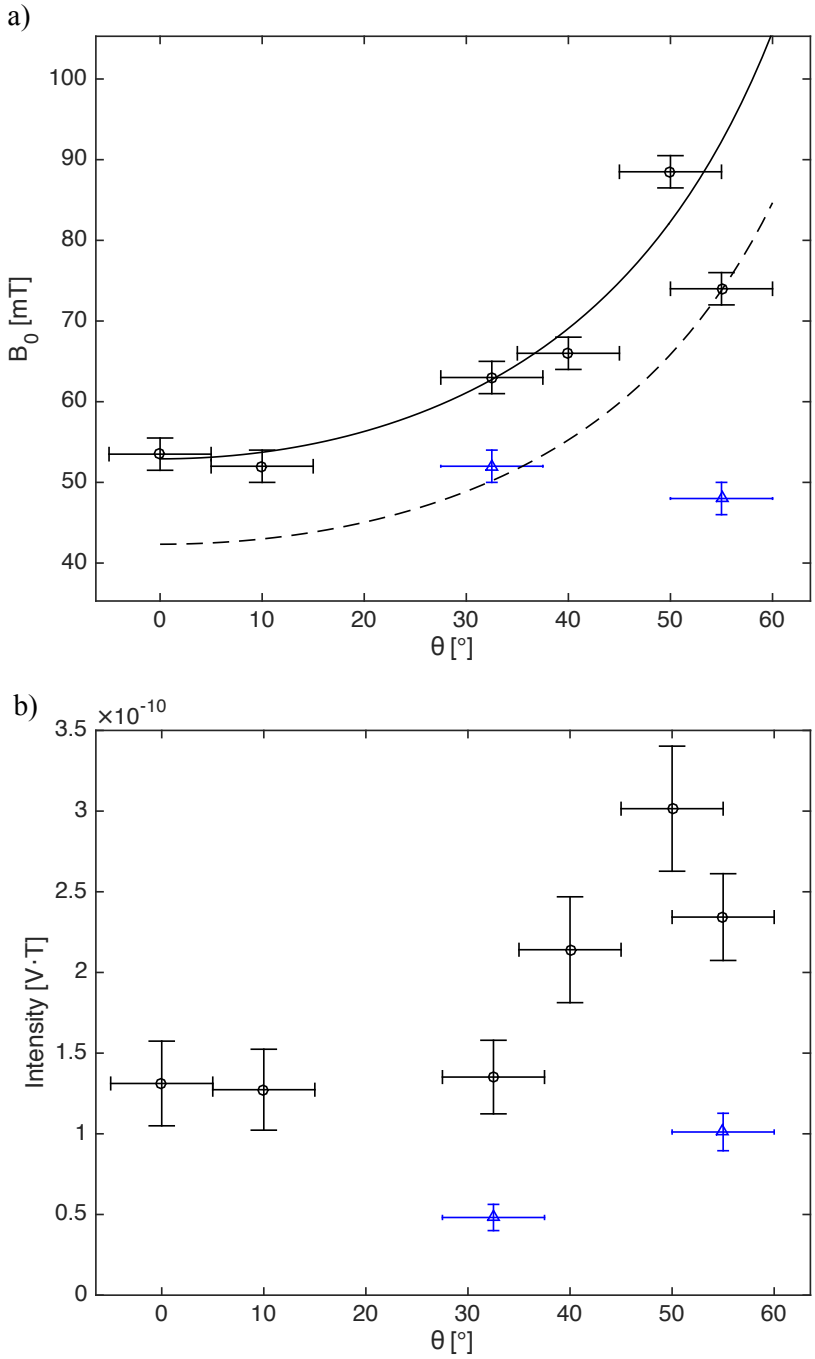

Figure 6.6: Angle dependence of SAWSR. a) Position of resonances as a function of angle θ between $\boldsymbol{B}_0$ and the c axis. Solid line is simulation for $g = 1.6$ and dotted line is for $g = 2$. b) Intensity of resonances as function of θ. Triangles are an additional resonance that appears in some of the measurements.

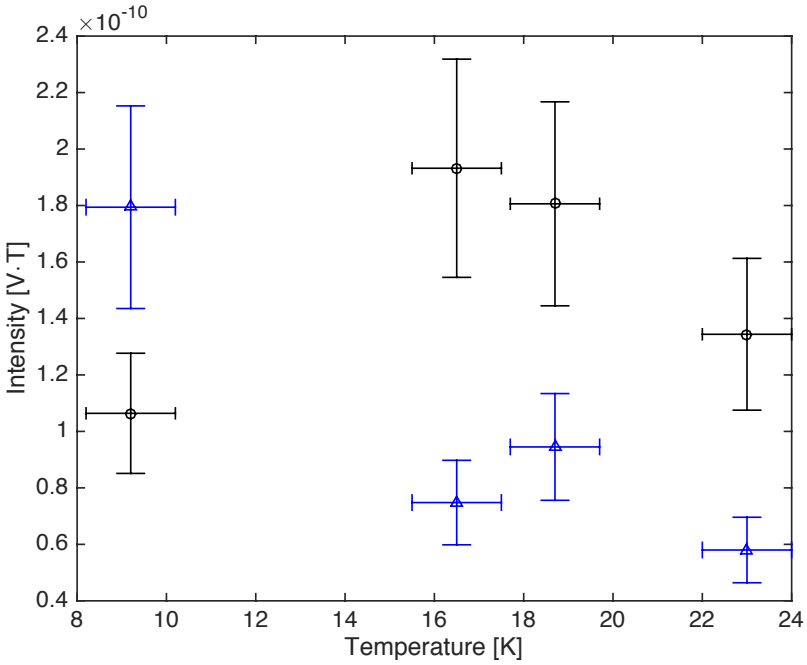

Figure 6.7: Temperature dependence of the SAWSR resonances seen at $\theta \simeq 55°$. Circles are the Fe^{2+} resonance at $B_0 \simeq 75\,\mathrm{mT}$, and the triangles are the lower-field resonance at $B_0 \simeq 50\,\mathrm{mT}$.

shows the result of this measurement. At the higher temperatures, the intensity of the higher-field resonance is higher than for the lower-field one, while at the lowest temperature measured that relationship gets inverted.

A power dependence measurement was done at $\theta \simeq 0°$. The results are plotted in Figure 6.8. It is apparent that saturation is setting in around 1 µW , as this is where the linewidth starts increasing and the intensity saturating. This result validates the choice of power at which all other measurements were done, $P \simeq 200\,\mathrm{nW} = -37\,\mathrm{dBm}$ ($\sqrt{P} \simeq 4.5 \times 10^{-4}\,\mathrm{W}^{1/2}$). We can also use the broadening of the linewidth to estimate the saturation parameter $s = 1 + (G\epsilon)^2 T_1 T_2 = 7.7/3.5 = 2.2 \pm 0.5$ at about 5 µW power. We estimate the strain at this power to be on the order of $\epsilon \sim 5 \times 10^{-5}$, giving an estimated order $G^2 T_1 T_2 \sim 5 \times 10^8$. To use this result to extract G would require

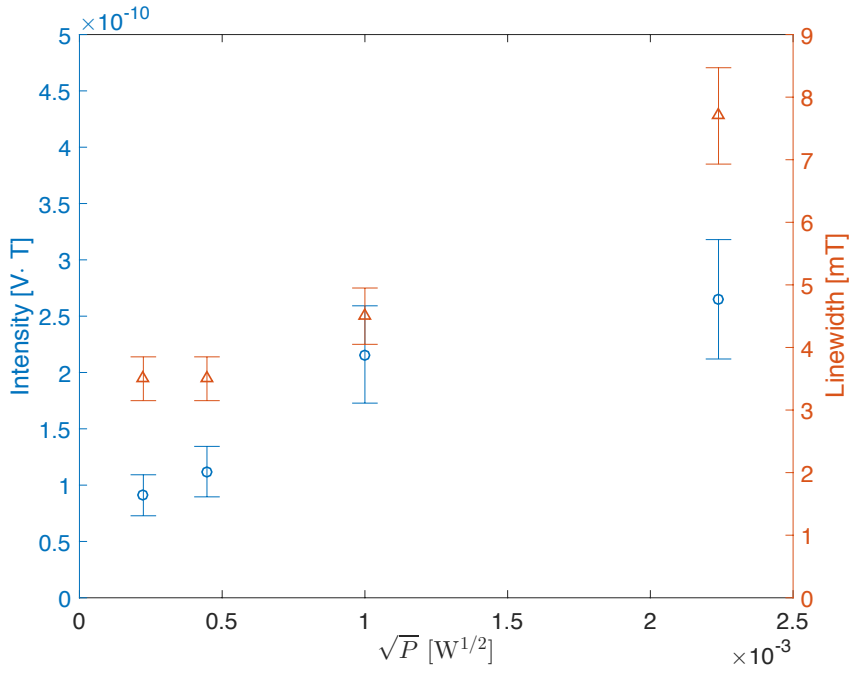

Figure 6.8: Power dependence of the SAWSR signal at $\theta \simeq 0$. Circles are intensity and triangles show the line width. Intensity increases approximately linearly with $\sqrt{P}$ for low power but saturates at high power, along with the linewidth broadening.

knowledge about T_1 and T_2, which we do not have at this time.

To further support the hypothesis that we are measuring acoustically excited spin resonance, and not simply exciting magnetically with the field around the IDT fingers, we also measured a SAW resonator on non-reduced lithium niobate containing mostly Fe^{3+}. As this species has $S = 5/2$, and much smaller D than Fe^{2+}, the $|m_s = -1/2\rangle \leftrightarrow |m_s = +1/2\rangle$ transition should be addressable, and located at about 85 mT. We measured in this range without finding any resonance, suggesting that there is not appreciable signal from magnetic excitation of the IDT.

Chapter 7

Conclusions

In conclusion, we have investigated various aspects of SAW devices and strain sensitive spin species in ZnO and $LiNbO_3$ for coupling surface acoustic waves to spin ensembles.

Firstly, we performed a series of ESR experiments exploring the potential of Fe^{3+} impurities in ZnO for spin-lattice coupling. This spin system has already been identified as a high potential quantum technology component due to its long coherence time. We have showed that the system also has good properties for spin-lattice coupling experiments, with a strain-coupling parameter $G_{33} = 280 \pm 5\,\mathrm{GHz/strain}$, which is about 16 times larger than the largest reported for NV centres in diamond. We found that the LEFE effect as well as the spin Hamiltonian parameter D have a linear temperature dependence. As the relative change in each coincide, this strongly supports the notion that the modification of D by an electric field is a multiplicative effect rather than an additive one, $D = D_0(1 + \kappa E)$. We also repeated LEFE measurements for Mn^{2+}:ZnO to compare to results in [38], and found that our measurement yielded a LEFE coefficient several times smaller, for reasons currently unknown. The LEFE coefficient

we measured was several times larger for Fe^{3+}:ZnO than for Mn^{2+}:ZnO.

Secondly, we have fabricated and characterised SAW devices on bulk ZnO crystals and Fe doped lithium niobate. We found that the nominally pure ZnO was conductive at room temperature due to n-type intrinsic doping, and electrical losses inhibited any transmission through a SAW delay line above $T = 200\,\mathrm{K}$. The one-port resonator measured down to milli-Kelvin temperatures showed excellent quality factors of up to $Q \simeq 1.5 \times 10^5$ in its superconducting state.

Thirdly, we designed and fabricated a superconducting split-coil magnet for use in a dilution refrigerator for magnetic field dependent measurements at milli-Kelvin temperatures. We characterised it by measuring the spectrum of a YIG sphere, and performed a proof of concept experiment using a coplanar waveguide resonator made from aluminium on sapphire. It showed that our setup with a fixed axis magnet and a rotating sample stage is a viable way to perform magnetic field and angle dependent microwave experiments at low temperature.

Finally, we performed a surface acoustic wave spin resonance (SAWSR) experiment using a one-port SAW resonator fabricated on Fe^{2+}:LN. We observed a clear signal at $T \simeq 25\,\mathrm{K}$, at a field near the expected one for a $\Delta m_s = 2$ transition between the $|-1\rangle$ and $|+1\rangle$ states. We concluded it to be a transition induced by acoustic coupling since the signal intensity did not tend to zero when the magnetic field was parallel to the crystal anisotropy axis. Furthermore, this tells us that the coupling is due to a modulation of the E zero-field splitting parameter rather than D. We investigated the dependence on microwave power and found the saturation limit. We performed

a measurement of Fe^{3+}:LN as well to reassure ourselves that the resonance is not magnetically excited by the field around the IDT.

7.1 Further experiments

To understand more about the potential of Fe^{3+}:ZnO for spin-lattice coupling experiments, G_{11} should also be found, by repeating the experiment with a different crystal axis orientation. Knowing this as well as G_{33} will allow for a better estimation of the coupling strength at all arbitrary magnetic field orientation. Growing intentionally Fe doped ZnO would be ideal, as we would not have to rely on unintentional impurities in our samples, which can vary widely. Alternatively, further developing the diffusion doping method could yield very high spin concentrations. With a high density, high crystal quality Fe^{3+}:ZnO sample, the SAWSR experiment could be repeated and expected to show positive results, as the linewidth can be expected to be much narrower than in Fe^{2+}:LN.

Learning from recent advances around us in the spin-lattice coupling community, it seems the ideal experiment should be designed such that the effect of the spin-lattice coupling is not measured with the acoustic mode itself, but with a more sensitive and well understood method. An approach more similar to that of MacQuarrie *et al.* [29], where NV centres in diamond are initialised and read out optically, $\Delta m_s = 1$ transitions driven with a microwave antenna, and $\Delta m_s = 2$ transitions driven with a bulk acoustic resonator, would be an interesting direction for SAW-spin coupling experiments. In fact, the same experiment could be repeated with a SAW resonator instead of a bulk acoustic resonator.

Taking a more general view of coupling SAW's to quantum states of impurities in crystals, it is clear that very large coupling parameters are achievable when looking at transitions to high energy excited electronic states, as in the case of the transition between the triplet ground state and the $|E_y\rangle$ excited state of the NV centres in diamond where the coupling is 610 THz/strain, compared to about 5 THz/strain for the $\Delta m_s = 2$ transition in Fe^{2+}:LN, and about 1 THz/strain for the $|\pm 3/2\rangle \leftrightarrow |\pm 5/2\rangle$ transition in Fe^{3+}:ZnO. It is not unlikely that SAWs will ultimately find more use in optomechanical applications than in traditional spin resonance.

Appendix A

Fabrication procedures

Here follows a list of the main fabrication procedures used in this thesis.

Cleaning wafers

- Leave in 80°C DMSO for up to 30 minutes
- Place beaker in ultrasonic bath at high power for 5 minutes
- Clean wafers in two beakers of hot water to remove DMSO
- Blow dry with N_2
- Repeat if necessary until surface is clean

UV-PL procedure

- Bake cleaned wafer to remove water at 110°C for 10 minutes
- Spin-coat TI PRIME immediately, 0-10sec 500RPM, 10-35 sec 3000RPM
- Bake at 120°C for 120 seconds
- Spin-coat AZ5214E photoresist, 0-10sec 500RPM 10-55sec 5000RPM

- Bake at 110°C for 50 seconds
- Expose the pattern using the photomask
  - Settings: Hard+Vacuum contact, Dose: 10 mJ/cm^2 for sapphire, 20 mJ/cm^2
- Bake at 120°C for 120 seconds
- Flood expose whole wafer, 200 mJ/cm^2
- Develop in developer for 2-3 minutes
- Blow dry with N_2

EBL procedure

- Spin-coat clean wafer with 950K PMMA A3 at 4000RPM for 45 seconds
- Bake on hot-plate at 180°C for 5 minutes
- Spin Electra 92 charge dissipation layer on wafer at 3000RPM for 30 seconds
- Expose in EBL machine with a dose of 450 $\mu C/cm^2$

EBL development

- To remove Electra layer, clean in DI water for 1 min
- Blow dry with N_2
- Develop first in MIBK:IPA (1:3) for 50 seconds and immediately in IPA 20 for seconds
- Blow dry with N_2

Lift-off

- Evaporate 5 nm of titanium and 45 nm of aluminium on wafer
- Leave in 60°C DMSO for up to 30 minutes
- Place beaker in ultrasonic bath at lowest power for 5 minutes
- Place wafer in water and check in microscope whether finished, repeat above if necessary
- Clean in hot DI water
- Blow dry with N_2

Bibliography

[1] Lauren Peters. *Rotatable Superconducting Coplanar Waveguide Resonators in Magnetic Fields*. M.phil. thesis, University of Oxford, 2015.

[2] Stephen Wiesner. Conjugate coding, 1983.

[3] C.H. Bennett and G. Brassard. Quantum cryptography: Public key distribution and coin tossing. *Proceedings of IEEE International Conference on Computers, Systems and Signal Processing*, 175:8, 1984.

[4] Paul Benioff. The computer as a physical system: A microscopic quantum mechanical Hamiltonian model of computers as represented by Turing machines. *Journal of Statistical Physics*, 22(5):563–591, May 1980.

[5] Richard P. Feynman. Simulating physics with computers. *International Journal of Theoretical Physics*, 21(6-7):467–488, 1982.

[6] Peter W. Shor. Polynomial-Time Algorithms for Prime Factorization and Discrete Logarithms on a Quantum Computer *. *SIAM Journal on Computing*, 26(5):1484–1509, 1997.

[7] I. M. Georgescu, S. Ashhab, and Franco Nori. Quantum simulation. *Reviews of Modern Physics*, 86(1), 2014.

[8] Romana Schirhagl, Kevin Chang, Michael Loretz, and Christian L Degen. Nitrogen-vacancy centers in diamond: nanoscale sensors for physics and biology. *Annual review of physical chemistry*, 65:83–105, 2014.

[9] M H Devoret and R J Schoelkopf. Superconducting circuits for quantum information: an outlook. *Science (New York, N.Y.)*, 339(6124):1169–74, 2013.

[10] John J L Morton, Alexei M Tyryshkin, Richard M Brown, Shyam Shankar, Brendon W Lovett, Arzhang Ardavan, Thomas Schenkel, Eugene E Haller, Joel W Ager, and S A Lyon. Solid-state quantum memory using the ^{31}P nuclear spin. *Nature*, 455(7216):1085–1088, 2008.

[11] M Wallquist, K Hammerer, P Rabl, M Lukin, and P Zoller. Hybrid quantum devices and quantum engineering. *Physica Scripta*, T137(T137):014001, December 2009.

[12] Ze-Liang Xiang, Sahel Ashhab, J. Q. You, and Franco Nori. Hybrid quantum circuits: Superconducting circuits interacting with other quantum systems. *Reviews of Modern Physics*, 85(2):623–653, April 2013.

[13] Gershon Kurizki, Patrice Bertet, Yuimaru Kubo, Klaus Mø lmer, David Petrosyan, Peter Rabl, and Jörg Schmiedmayer. Quantum technologies with hybrid systems. *Proceedings of the National Academy of Sciences of the United States of America*, 112(13):3866–3873, March 2015.

[14] a D O'Connell, M Hofheinz, M Ansmann, Radoslaw C Bialczak, M Lenander, Erik Lucero, M Neeley, D Sank, H Wang, M Weides, J Wenner, John M Mar-

tinis, and a N Cleland. Quantum ground state and single-phonon control of a mechanical resonator. *Nature*, 464(7289):697–703, 2010.

[15] Y. Kubo, F. R. Ong, P. Bertet, D. Vion, V. Jacques, D. Zheng, A. Dréau, J.-F. Roch, A. Auffeves, F. Jelezko, J. Wrachtrup, M. F. Barthe, P. Bergonzo, and D. Esteve. Strong Coupling of a Spin Ensemble to a Superconducting Resonator. *Physical Review Letters*, 105(14):140502, September 2010.

[16] Martin J A Schuetz, Eric M Kessler, Geza Giedke, Lieven M K Vandersypen, Mikhail D Lukin, and J Ignacio Cirac. Universal Quantum Transducers based on Surface Acoustic Waves. *Physical Review X*, 5(3), 2015.

[17] E. B. Magnusson, B. H. Williams, R. Manenti, M.-S. Nam, A. Nersisyan, M. J. Peterer, A. Ardavan, and P. J. Leek. Surface acoustic wave devices on bulk ZnO crystals at low temperature. *Applied Physics Letters*, 106(6):063509, February 2015.

[18] Anthony Mark Fox. *Quantum Optics: An Introduction*. OUP Oxford, 2006.

[19] Christopher Gerry and Peter Knight. *Introductory Quantum Optics*. Cambridge University Press, Cambridge, 2004.

[20] D.F. Walls and Gerard J. Milburn. *Quantum Optics*. Springer-Verlag Berlin Heidelberg, Berlin, 2008.

[21] D. Leibfried, R. Blatt, C. Monroe, and D. Wineland. Quantum dynamics of single trapped ions. *Reviews of Modern Physics*, 75(1):281–324, March 2003.

[22] T P Harty, D T C Allcock, C J Ballance, L Guidoni, H A Janacek, N M Linke,

D N Stacey, and D M Lucas. High-Fidelity Preparation, Gates, Memory, and Readout of a Trapped-Ion Quantum Bit. *Physical review letters*, 113(22):220501, November 2014.

[23] D. I. Schuster, A. P. Sears, E. Ginossar, L. DiCarlo, L. Frunzio, J. J. L. Morton, H. Wu, G. A. D. Briggs, B. B. Buckley, D. D. Awschalom, and R. J. Schoelkopf. High-Cooperativity Coupling of Electron-Spin Ensembles to Superconducting Cavities. *Physical Review Letters*, 105(14):140501, September 2010.

[24] Alexandre Blais, Ren-Shou Huang, Andreas Wallraff, S. M. Girvin, and R. J. Schoelkopf. Cavity quantum electrodynamics for superconducting electrical circuits: An architecture for quantum computation. *Physical Review A*, 69(6):062320, June 2004.

[25] A Wallraff, D I Schuster, A Blais, L Frunzio, R-S Huang, J Majer, S Kumar, S M Girvin, and R J Schoelkopf. Strong coupling of a single photon to a superconducting qubit using circuit quantum electrodynamics. *Nature*, 431(7005):162–7, September 2004.

[26] Xiaobo Zhu, Shiro Saito, Alexander Kemp, Kosuke Kakuyanagi, Shin-ichi Karimoto, Hayato Nakano, William J Munro, Yasuhiro Tokura, Mark S Everitt, Kae Nemoto, Makoto Kasu, Norikazu Mizuochi, and Kouichi Semba. Coherent coupling of a superconducting flux qubit to an electron spin ensemble in diamond. *Nature*, 478(7368):221–4, October 2011.

[27] Y. Kubo, C. Grezes, A. Dewes, T. Umeda, J. Isoya, H. Sumiya, N. Morishita, H. Abe, S. Onoda, T. Ohshima, V. Jacques, A. Dréau, J.-F. Roch, I. Diniz,

A. Auffeves, D. Vion, D. Esteve, and P. Bertet. Hybrid Quantum Circuit with a Superconducting Qubit Coupled to a Spin Ensemble. *Physical Review Letters*, 107(22):220501, November 2011.

[28] Menno Poot and Herre S.J. van der Zant. Mechanical systems in the quantum regime. *Physics Reports*, 511(5):273–335, February 2012.

[29] E. R. MacQuarrie, T. A. Gosavi, A. M. Moehle, N. R. Jungwirth, S. A. Bhave, and G. D. Fuchs. Coherent control of a nitrogen-vacancy center spin ensemble with a diamond mechanical resonator. *Optica*, 2(3):233, March 2015.

[30] D. Andrew Golter, Thein Oo, Mayra Amezcua, Kevin A. Stewart, and Hailin Wang. Optomechanical Quantum Control of a Nitrogen-Vacancy Center in Diamond. *Physical Review Letters*, 116(14):143602, April 2016.

[31] A. Abragam and B. Bleaney. *Electron Paramagnetic Resonance of Transition Ions*. OUP Oxford, 2012.

[32] Arthur Schweiger and Gunnar Jeschke. *Principles of Pulse Electron Paramagnetic Resonance*. Oxford University Press, 2001.

[33] John W. Tucker and V. W. Rampton. *Microwave ultrasonics in solid state physics*. North-Holland Pub. Co., 1973.

[34] K W H Stevens. Matrix Elements and Operator Equivalents Connected with the Magnetic Properties of Rare Earth Ions. *Proceedings of the Physical Society. Section A*, 65(3):209–215, March 1952.

[35] W. B. Mims. *The Linear Electric Field Effect In Paramagnetic Resonance*. Oxford University Press, 1976.

[36] R.T. Eaton, G.R.; Eaton, S.S.; Barr, D.P.; Weber. *Quantitative EPR*. Springer, 2010.

[37] W. B. Mims. Phase Memory in Electron Spin Echoes, Lattice Relaxation Effects in $CaWO_4$: Er, Ce, Mn. *Physical Review*, 168(2):370–389, April 1968.

[38] Richard E. George, James P. Edwards, and Arzhang Ardavan. Coherent Spin Control by Electrical Manipulation of the Magnetic Anisotropy. *Physical Review Letters*, 110(2):027601, January 2013.

[39] A. Igelmund and A. Hausmann. Forbidden ESR transitions $\Delta S = \pm 2$ of Fe^{3+} and Mn^{2+} in zinc oxide. *Zeitschrift für Physik B Condensed Matter and Quanta*, 21(1):65–67, March 1975.

[40] W. M. Walsh and L. W. Rupp. Paramagnetic Resonance of Trivalent ^{57}Fe in Zinc Oxide. *Physical Review*, 126(3):952–955, May 1962.

[41] J. Tribollet, J. Behrends, and K. Lips. Ultra long spin coherence time for Fe^{3+} in ZnO: A new spin qubit. *EPL (Europhysics Letters)*, 84(2):20009, October 2008.

[42] M Goryca, M Koperski, P Wojnar, T Smoleski, T Kazimierczuk, A Golnik, and P Kossacki. Coherent Precession of an Individual 5/2 Spin. *Physical review letters*, 113(22):227202, November 2014.

[43] Tatyana Volk and Manfred Wöhlecke. *Lithium Niobate: Defects, Photorefraction*

and Ferroelectric Switching, volume 115 of *Springer Series in Materials Science*. Springer Berlin Heidelberg, Berlin, Heidelberg, 2008.

[44] M. Goulkov and Th. Woike. Photoelectric response in $LiNbO_3$:Fe versus Fe^{2+}/Fe^{3+}ratio studied by PILS method. *JOURNAL OF THE OPTICAL SOCIETY OF AMERICA B*, 31:1071–1077, 2014.

[45] W. Phillips and D. L. Staebler. Control of the Fe^{2+} concentration in iron-doped lithium niobate. *Journal of Electronic Materials*, 3(2):601–617, May 1974.

[46] J.B. Herrington, B. Dischler, and J. Schneider. An EPR investigation of Fe^{3+} and Mn^{2+} in $LiNbO_3$. *Solid State Communications*, 10(6):509–511, March 1972.

[47] Yasuo Cho, Hideyoshi Horie, and Kazuhiko Yamanouchi. Surface Acoustic Wave Paramagnetic Resonance in Iron Doped-$LiNbO_3$. *Japanese Journal of Applied Physics*, 29(S1):19, January 1990.

[48] S. Juppe and O. F. Schirmer. Thermally detected electron spin resonance of Fe^{2+} in LiNbO3. *Solid State Communications*, 76(3):299–302, 1990.

[49] G. I. Malovichko, V. G. Grachev, E. P. Kokanyan, O. F. Schirmer, K. Betzler, B. Gather, F. Jermann, S. Klauer, U. Schlarb, and M. Whlecke. Characterization of stoichiometric $LiNbO_3$ grown from melts containing K_2O. *Applied Physics A Solids and Surfaces*, 56(2):103–108, February 1993.

[50] Maria Vittoria Ciampolillo. *Diffusion of Iron in Lithium Niobate for Applications in Integrated Optical Devices*. Ph.d. thesis, University of Padova, Italy, 2010.

[51] Maxim Goryachev, Nikita Kostylev, and Michael E. Tobar. Single-photon level

study of microwave properties of lithium niobate at millikelvin temperatures. *Physical Review B*, 92(6):060406, August 2015.

[52] Lord Rayleigh. On Waves Propagated along the Plane Surface of an Elastic Solid. *Proceedings of the London Mathematical Society*, s1-17(1):4–11, November 1885.

[53] David Morgan. *Surface Acoustic Wave Filters, Second Edition: With Applications to Electronic Communications and Signal Processing (Studies in Electrical and Electronic Engineering)*. Academic Press, 2007.

[54] R. Manenti, M. J. Peterer, A. Nersisyan, E. B. Magnusson, A. Patterson, and P. J. Leek. Surface acoustic wave resonators in the quantum regime. *Physical Review B*, 93(4):041411, January 2016.

[55] A. Megrant, C. Neill, R. Barends, B. Chiaro, Yu Chen, L. Feigl, J. Kelly, Erik Lucero, Matteo Mariantoni, P. J. J. OMalley, D. Sank, A. Vainsencher, J. Wenner, T. C. White, Y. Yin, J. Zhao, C. J. Palmstrom, John M. Martinis, and A. N. Cleland. Planar superconducting resonators with internal quality factors above one million. *Applied Physics Letters*, 100(11):113510, March 2012.

[56] Martin V. Gustafsson, Paulo V. Santos, Göran Johansson, and Per Delsing. Local probing of propagating acoustic waves in a gigahertz echo chamber. *Nature Physics*, 8(4):338–343, February 2012.

[57] Martin V Gustafsson, Thomas Aref, Anton Frisk Kockum, Maria K Ekström, Göran Johansson, and Per Delsing. Propagating phonons coupled to an artificial atom. *Science (New York, N.Y.)*, 346(6206):207–11, October 2014.

[58] W. A. Phillips. Two-level states in glasses. *Rep. Prog. Phys.*, 50:1657–1708, 1987.

[59] L. P. Kouwenhoven. Electron transport in quantum dots. In Lydia L. Sohn, Leo P. Kouwenhoven, and Gerd Schön, editors, *Mesoscopic Electron Transport*. Springer, 1997.

[60] V. Talyanskii, J. Shilton, M. Pepper, C. Smith, C. Ford, E. Linfield, D. Ritchie, and G. Jones. Single-electron transport in a one-dimensional channel by high-frequency surface acoustic waves. *Physical Review B*, 56(23):15180–15184, 1997.

[61] P. J. Leek, M. R. Buitelaar, V. I. Talyanskii, C. G. Smith, D. Anderson, G. A C Jones, J. Wei, and D. H. Cobden. Charge pumping in carbon nanotubes. *Physical Review Letters*, 95(25), 2005.

[62] M Weiler, L Dreher, C Heeg, H Huebl, R Gross, M S Brandt, and S T B Goennenwein. Elastically driven ferromagnetic resonance in nickel thin films. *Physical review letters*, 106(11):117601, March 2011.

[63] M Weiler, H Huebl, F S Goerg, F D Czeschka, R Gross, and S T B Goennenwein. Spin pumping with coherent elastic waves. *Physical review letters*, 108(17):176601, April 2012.

[64] Chennupati Jagadish and Stephen Pearton, editors. *Zinc Oxide Bulk, Thin Films and Nanostructures*. Elsevier, Oxford, first edition, 2006.

[65] A.H. Weber, G. Weiss, and S. Hunklinger. Comparison of Rayleigh and Sezawa

wave modes in ZnO-SiO_2-Si structures. In *IEEE 1991 Ultrasonics Symposium*, pages 363–366. IEEE, 1991.

[66] Vitaliy Avrutin, Gene Cantwell, J J Song, Donald J Silversmith, and Hadis Morkoç. Bulk ZnO: Current Status, Challenges, and Prospects. *Proceedings of the IEEE*, 98(7):1339–1350, July 2010.

[67] M. V. Ciampolillo, A. Zaltron, M. Bazzan, N. Argiolas, C. Sada, and M. Bianconi. Lithium niobate crystals doped with iron by thermal diffusion: Relation between lattice deformation and reduction degree. *Journal of Applied Physics*, 107(8):084108, April 2010.

[68] G. J. Dolan. Offset masks for lift-off photoprocessing. *Applied Physics Letters*, 31(5):337–339, 1977.

[69] A. I. Harris, M. Sieth, J. M. Lau, S. E. Church, L. A. Samoska, and K. Cleary. Note: Cryogenic microstripline-on-Kapton microwave interconnects, 2012.

[70] M. Tinkham. Effect of Fluxoid Quantization on Transitions of Superconducting Films. *Physical Review*, 129(6):2413–2422, March 1963.

[71] J. E. Healey, T. Lindstrom, M. S. Colclough, C. M. Muirhead, and A. Ya. Tzalenchuk. Magnetic field tuning of coplanar waveguide resonators. *Applied Physics Letters*, 93(4):043513, July 2008.

[72] C. Song, T. W. Heitmann, M. P. Defeo, K. Yu, R. McDermott, M. Neeley, John M. Martinis, and B. L T Plourde. Microwave response of vortices in super-

conducting thin films of Re and Al. *Physical Review B - Condensed Matter and Materials Physics*, 79(17), 2009.

[73] David M. Pozar. *Microwave Engineering*. Wiley, 1990.

[74] Preeti Ovartchaiyapong, Kenneth W Lee, Bryan A Myers, and Ania C Bleszynski Jayich. Dynamic strain-mediated coupling of a single diamond spin to a mechanical resonator. *Nature communications*, 5:4429, January 2014.

[75] J. Teissier, A. Barfuss, P. Appel, E. Neu, and P. Maletinsky. Strain coupling of a nitrogen-vacancy center spin to a diamond mechanical oscillator. *Physical Review Letters*, 113(2), 2014.

[76] Marcus W. Doherty, Viktor V. Struzhkin, David A. Simpson, Liam P. McGuinness, Yufei Meng, Alastair Stacey, Timothy J. Karle, Russell J. Hemley, Neil B. Manson, Lloyd C L Hollenberg, and Steven Prawer. Electronic properties and metrology applications of the diamond NV - Center under pressure. *Physical Review Letters*, 112(4), 2014.

[77] G I Malovichko, V G Grachev, O F Schirmer, and B Faust. New axial Fe^{3+} centres in stoichiometric lithium niobate crystals. *Journal of Physics: Condensed Matter*, 5(23):3971–3976, June 1993.

[78] O.S. Heavens, M.M. Brown, and V. Hinton. The structure and density of iron films formed by thermal evaporation. *Vacuum*, 9(1):17–20, March 1959.

[79] U. Ozgur, Ya. I. Alivov, C. Liu, A. Teke, M. A. Reshchikov, S. Dogan, V. Avrutin,

S.-J. Cho, and H. Morkoc. A comprehensive review of ZnO materials and devices. *Journal of Applied Physics*, 98(4):041301, August 2005.

[80] A. El Habti. High-frequency surface acoustic wave devices at very low temperature: Application to loss mechanisms evaluation. *The Journal of the Acoustical Society of America*, 100(1):272, July 1996.

[81] C. Galassi, M. Dinescu, K. Uchino, and M. Sayer, editors. *Piezoelectric Materials: Advances in Science, Technology and Applications*. Springer, 2000.